UNIVERSITY OF CALIFORNIA SAN DIEGO

Nanostructured Materials for Energy Storage Devices

A dissertation submitted in partial satisfaction of the requirements
for the degree Doctor of Philosophy

in

Nanoengineering

by

Xiujun Yue

Committee in charge:

Professor Ping Liu, Chair
Professor Prabhakar Rao Bandaru
Professor Renkun Chen
Professor Zheng Chen
Professor David Fenning

2019

The Dissertation of Xiujun Yue is approved, and it is acceptable in quality and form for publication on microfilm and electronically:

_____

_____

_____

_____

_____

Chair

University of California San Diego

2019

DEDICATION

To my family and my loved ones.

TABLE OF CONTENTS

LIST OF FIGURES

LIST OF TABLES

ACKNOWLEDGEMENTS

First of all, I would like to express my sincere appreciation and thanks to my advisor and mentor, Prof. Ping Liu. Without the great support and guidance from him, this dissertation could not have been completed. His advices are invaluable on my research as well as career and life. I would also like to thank my committee members, Prof. Prabhakar Rao Bandaru, Prof. Renkun Chen, Prof. Zheng Chen and Prof. David Fenning for their valuable time and comments. In addition, I would like to thank Prof. Liangfang Zhang who encouraged me at my hardship.

Secondly, I would like to thank all the present past lab members who have helped and inspired me. Special thanks to Dr. Haodong Liu for the tremendous help and inspiring discussions with him. My sincere thanks to Dr. Hee-dae Lim, Hongyao Zhou, Xing Xing, Zhaohui Wu, and Matthew Gonzalez, for their invaluable help on researches.

I would also like to express my thanks to Dana Jimenez, who helped on administrative issues.

In the end, special thanks to my family. Great help and encouraging from my parents and my wife Yang Shi have supported me to overcome all the challenges and hardship.

Chapter 2, in full, is a reprint of materials published in the following paper: Xiujun Yue, Qian He, Hee-dae Lim and Ping Liu*, “Hierarchical structural designs of ion exchange membranes for flow batteries" *J. Mater. Chem. A.*, **2019**, 7, 5794-5802. The

dissertation author was the primary researcher for the data presented and was the primary author of this publication. The permissions to reproduce this material were granted by the Royal Society of Chemistry, copyright 2019.

Chapter 3, in full, is a reprint of materials published in the following paper: Haodong Liu, Xiujun Yue, Xing Xing, Qizhang Yan, Jason Huang, Victoria Petrova, Hongyao Zhou and Ping Liu*, "A scalable 3D lithium metal anode" *Energy Storage Materials*, **2019**, 16, 505-511. The dissertation author was one of the primary researchers for the data presented and was one of the primary authors of this publication. The permissions to reproduce this material were granted by the Elsevier B.V., copyright 2018.

Chapter 4, in full, is a reprint of materials published in the following paper: Xiujun Yue, Haodong Liu and Ping Liu*, "Polymer grafted on carbon nanotubes as a flexible cathode for aqueous zinc ion batteries" *Chem. Commun.*, **2019**, 55, 1647-1650. The dissertation author was the primary researcher for the data presented and was the primary author of this publication. The permissions to reproduce this material were granted by the Royal Society of Chemistry, copyright 2019.

VITA

Education

2019 Doctor of Philosophy, Nanoengineering, University of California San Diego, La Jolla, California

2014 Master of Science, Nanoengineering, University of California San Diego, La Jolla, California

2013 Bachelor of Science, Applied Chemistry and Engineering, Tianjin University, Tianjin, China

Publications

1. "Bio-inspired Structural Colors Produced via Self-Assembly of Synthetic Melanin Nanoparticles", Ming Xiao, Yiwen Li, Michael Allen, Dimitri Deheyn, **Xiujun Yue**, Juizhou Zhao, Nathan Gianneschi, Matthew Shawkey, and Ali Dhinojwala, *ACS Nano*, 2015, 9, 5454

2. "Mimicking melanosomes: Polydopamine nanoparticles as artificial microparasols", Yuran Huang, Yiwen Li, Ziying Hu, **Xiujun Yue**, Maria T Proetto, Ying Jones and Nathan C Gianneschi, *ACS Central Science*, 2017, 3, 564.

3. "Designing solution chemistries for the low-temperature synthesis of sulfide-based solid electrolytes", Hee-Dae Lim, **Xiujun Yue**, Xing Xing, Victoria Petrova, Matthew Gonzalez, Haodong Liu and Ping Liu, *Journal of Materials Chemistry A*, 2018, 6, 7370.

4. "Resolving the Compositional and Structural Defects of Degraded $LiNi_xCo_yMn_zO_2$ Particles to Directly Regenerate High-Performance Lithium-Ion Battery Cathodes", Yang Shi, Gen Chen, Fang Liu, **Xiujun Yue** and Zheng Chen, *ACS Energy Letters*, 2018, 3, 1683.

5. "Dendrite Suppression Membranes for Rechargeable Zinc Batteries", Byoung-Sun Lee, Shuang Cui, Xing Xing, Haodong Liu, **Xiujun Yue**, Victoria Petrova, Hee-Dae Lim, Renkun Chen and Ping Liu, *ACS Applied Materials & Interfaces*, 2018, 10, 38928.

6. “A scalable 3D lithium metal anode”, Haodong Liu, **Xiujun Yue**, Xing Xing, Qizhang Yan, Jason Huang, Victoria Petrova, Hongyao Zhou and Ping Liu, *Energy Storage Materials*, 2019, 16, 505.

7. “Polymer grafted on carbon nanotubes as a flexible cathode for aqueous zinc ion batteries”, **Xiujun Yue**, Haodong Liu and Ping Liu, *Chemical Communications*, 2019, 55, 1647.

8. “Hierarchical structural designs of ion exchange membranes for flow batteries”, **Xiujun Yue**, Qian He, Hee-dae Lim and Ping Liu, *Journal of Materials Chemistry A*, 2019, 7, 5794-5802.

9. “In situ chemical synthesis of fluorine-free solid electrolyte interface for lithium metal batteries”, Hongyao Zhou, Haodong Liu, Yejing Li, **Xiujun Yue**, Xuefeng Wang, Matthew Gonzalez, Ying Shirley Meng and Ping Liu, *Journal of Materials Chemistry A*, submitted.

ABSTRACT OF THE DISSERTATION

Nanostructured Materials for Energy Storage Devices

by

Xiujun Yue

Doctor of Philosophy in Nanoengineering

University of California San Diego, 2019

Professor Ping Liu, Chair

Driven by the flourishing of renewable energy sources and increasing demands of portable electronics and electric vehicles, high-performance energy storage devices are required for applications at different scales. Benefiting from the small size, high surface area and hierarchical structures, nanostructured materials have been playing critical roles in the development of advanced energy storage devices.

This dissertation will discuss the applications of nanostructured materials to address performance challenges for different types of energy storage devices. Chapter 2 provides a new strategy to fabricate a cation exchange membrane that features a dense, crack-free tungsten oxide coating layer on Nafion that also penetrates into the Nafion's hydrophilic, ionic cluster regions. The hierarchical structural designs overcome the inherent tradeoff between conductivity and permeability of ion exchange membranes for redox flow batteries. In Chapter 3, a facile and scalable method is demonstrated to fabricate a 3D lithium metal anode with lithium nitrate, polyvinylidene difluoride, and nano-sized carbon black. The multi-functional 3D electrodes enable dendrite-free lithium metal cycling with high coulombic efficiency. In Chapter 4, a non-toxic, free-standing and flexible cathode is developed by grafting polydopamine on carbon nanotubes for aqueous zinc-ion battery. Cross-linked highly uniform active materials and the efficient conducting network overcome the long term cycling stability issue of aqueous zinc-ion batteries.

Chapter 1: Introduction

1.1 The need for energy storage devices

Since the invention of Voltaic Pile, the first battery invented in 1800, energy storage devices have been intensively studied, especially during the past decades driven by the explosive demanding from different fields.[1-4] From biomedical and personal electronic devices to electric vehicles (EVs) and even the grids, energy storage devices play critical roles.[5-6]

Due to the air pollution and many other issues of internal combustion engine vehicles (ICEVs), the market of EVs is developing rapidly.[7] Plans to promote EVs or even ban the sale of ICEVs have been announced by several countries.[8-9] However, even with much improved EV performances and encouraging policies by governments, many consumers still cannot fully accept EVs due to the worries on driving range and charging time.[9-11] Correspondingly, high energy density and rate capability are required for the energy storage devices for EVs. In addition, the public's awareness on the safety issue also has been aroused by reports about EVs' accidents.[12]

The electric grid has an intrinsic unbalancing issue as a result of varying demands over different periods of time in a day.[1] The intermittent nature of renewable resources, including wind, solar, tides etc., aggravates such problems even more.[13-15] Energy storage devices can serve as power banks to store extra energy during off-peak hours and make up the demand during peak hours. Energy storage will be a must for the grid when the

portions form renewable resources are larger than about 10%.[1] Energy storage devices for grids are expected to be large-scale low-cost systems with high capacity.

To meet the different requirements of various application scenarios, different types of energy storage devices have been developed: rechargeable batteries, redox flow batteries, fuel cells, supercapacitors etc.. All these energy storage devices have their own unique advantages and challenges. Our research is mainly focusing on redox flow batteries, lithium-ion batteries and zinc-ion batteries.

1.2 Redox flow batteries and nanostructured materials

Redox flow battery (RFB) is an electrochemical device which stores energy by two pairs of redox couples in two electrolytes. Catholyte and anolyte stored in two external tanks are pumped through porous electrodes. Two electrolytes are separated by a separator, which typically is a selective ion exchange membrane (IEM). With such a unique set up, the capacity of a RFB is decided by the size of external tanks rather than the battery itself.[16] With low cost, long life, rapid response, high mobility and flexibility, RFBs can serve as suitable large-scale energy storage devices for the grids.[17-19]

IEM is one of the key components of the RFB, which allows the diffusion of charge-carrying ions while preventing the mixing of catholyte and anolyte. An ideal IEM is supposed to have high conductivity to decrease the Ohmic loss and low crossover rate to prevent the self-discharging. Nafion, a tetrafluoroethylene based copolymer with

sulfuric acid functional groups, is one of the most widely used IEMs for RFB for its outstanding conductivity and stability.[20-21] The conductivity of Nafion membranes is relied on nano-sized hydrophilic ionic clusters formed by phase segregation. But such structure also causes the crossover of active species which lead to self-discharging or irreversible contamination. Some other non-fluorinated polymers such as sulfonated poly(tetramethydiphenyl ether ether ketone) (SPEEK) also have been utilized as IEMs for redox flow batteries for lower cost.[22] However, most of the polymeric IEMs suffer from serious crossover problem.[13, 23]

Various nanostructured materials have been developed to overcome the trade-off relationship between conductivity and selectivity of polymeric IEMs. Teng et al fabricated a Nafion/SiO_2 hybrid membrane with silicate nanoparticles in the ionic clusters of Nafion via *in situ* sol-gel reactions of tetraethoxysilane (TEOS) and diethoxydimethylsilane (DEDMS).[24] The vanadium RFB with such composite membrane achieved an energy efficiency of 87.4% at 20 mA cm^{-2}, while the one for Nafion is only 73.8%. A series of low-cost SPEEK/nano oxides composite membranes with Al_2O_3, SiO_2, and TiO_2 were demonstrated to have improved flow battery performances than Nafion 117 as a result of lower crossover rate.[22] Beside nano fillers, Qiao et al developed a poly(ether sulfone) (PES)/SPEEK porous membrane with a slit-like layer which is consist of nano-sized channels.[25] Compared with Nafion, the RFB performances were much enhanced by the highly selective skin layer. In another work by Yan et al, four orders of

magnitude lower VO^{2+} ion permeability than that of Nafion was achieved by a supported silica thin film with highly ordered, vertically aligned, and subnanosized channels.[26]

1.3 Lithium-ion batteries and nanostructured materials

Lithium-ion battery is regarded as the foundation of the mobile world.[27] From the first commercial versions by Sony in 1991, modern lithium-ion batteries bring powerful devices to everyone's life.[1, 28] Closing to the theoretical limit, researchers are pursuing next-generation high-energy batteries in many approaches.[4, 28-30] Nanostructured materials have had and will continue to have a profound impact on the development of lithium-ion batteries which play versatile roles according to different demands. Small sizes of nanostructured materials contribute to short diffusion distances. Large surface area enables more effective contact with electrolyte. Hierarchical structures of nanomaterials may provide electronic conduction network, encapsulate active materials, and mitigate volume change or mechanical stress.

For most cases, intercalation type cathode materials for lithium-ion battery take the advantages of high surface area and short transport length of the nanostructure. Longoni et al obtained a capacity retention of 77.7% at 20 C by *in situ* $LiFePO_4$ nano-particles grown on few-layer graphene flakes.[31] Zhang et al developed a V_2O_5 nanosheet/SWCNT hybrid electrodes with high capacities (370 mA h g^{-1} at 0.05 C),

excellent energy (555 W h kg^{-1}), and power densities (2175 W kg^{-1}) due to the synergistic effects from the high surface area nanosheets and the SWCNT conductive matrix.[32]

Silicon has a high capacity of 4200 mAh g^{-1} as an anode material for lithium-ion battery, but suffers from rapid capacity decay as a result of huge volume change (~320%).[33] Nanostructured materials can effectively buffer the volume change.[34] Tian et al developed a composite anode of nano-porous silicon with carbon coating which maintains 86.8% of initial capacity after 300 cycles at 500 mA g^{-1}.[35] Chen et al achieved a high capacity retention of 2925 mAh g^{-1} after 100 cycles at 0.5 A g^{-1} with silver treated hollow silicon nanospheres.[36]

Lithium-sulfur battery is attracting more and more interest for its high theoretical energy density and low cost.[37] The commercialization of lithium-sulfur battery is hindered by the insulating nature, large volume variation, and dissolution problem.[38] Utilizing conductive and porous nano structure serving as volume mediator and sulfur trap is one of the most popular solutions.[39-40] Chen et al developed a sulfur cathodes enabled by 3D hierarchically porous TiO_2/graphene composite which delivered a high rate performance of 832 mAh g^{-1} at 2 C and excellent cycling stability for 300 cycles at 0.2 C.[41] Combining both physical confinement and chemical interaction, Liang et al realized an ultra-low fading rate of 0.039% per cycle over 1700 cycles by the nano-sized sulfur/MnO_2 coreshell structure in Li-S cells.[42]

Lithium metal anode has been considered as a key component to achieving next-generation high-energy batteries for the high theoretical capacity and low electrochemical potential.[29] To realize the successful commercialization of lithium metal battery, safety and cyclability are two major challenges which mainly origin from the dendrite growth, solid electrolyte interphase (SEI) formation, and volume change.[28] Tremendous efforts have been made to solve those problems with nanostructured materials from different aspects. Kozen et al demonstrated a 14 nm thick ALD Al_2O_3 layer can serve as a stable artificial SEI for lithium metal anode to deliver much improved capacity retention for 100 cycles.[43] Yan et al designed a carbon nanocapsule, with gold nanoparticles decorated on the inner shell surface, which can guide lithium deposition solely inside the nanocapsules with well-defined morphology.[44] Combining with stabilization effect of the nanocapsules, a high coulombic efficiency (98%) was achieved even in alkyl carbonate electrolyte. Shen et al developed a CNT sponge based 3D host for lithium metal which manipulated the volume expansion and suppressed the dendrite growth as a result of confined lithium deposition.[45]

1.4 Zinc-ion batteries and nanostructured materials

Lithium-ion battery has been dominating the market, however, alternative batteries are also in demand due to concerns on the cost, safety, environmental friendliness, and long-term risk of shortage.[46] Among monovalent (K^+, Na^+) or

multi-valent (Mg^{2+}, Ca^{2+}, Zn^{2+}, Al^{3+}) metal ions, Zn^{2+} is an attractive candidate since zinc-ion battery has unique advantages in all the mentioned aspects.[47] A zinc-ion battery basically consists of a cathode as the host for zinc ions, zinc metal foil as anode, filter paper or glass fiber as separator and aqueous electrolyte in majority.[48] Unlike lithium-ion battery, studies on zinc-ion battery are immature and mainly focusing the cathode. It is still challenging to develop advanced cathode materials for zinc-ion battery with high capacity, cyclability, and rate capability.

Nano-scale structures are widely adopted by cathode active materials for zinc-ion batteries due to the high surface area which can enhance the electrode performance from several aspects: (1) Increase the electrode/electrolyte contacting area. (2) Decrease the particle size to reduce the diffusion distance. (3) Reduce electrical transportation distance to compromise the inherent low conductivity of many cathode materials. Li et al developed a flexible zinc-ion battery with MoS_2 nanosheets which delivers a specific capacity of 202.6 mA h g^{-1} at 0.1 A g^{-1}, as well as good cycle stability (98.6% capacity retention over 600 cycles).[49] Sambandam et al demotrated $Zn_2V_2O_7$ nanowire cathode has stable cyclability over 200 cycles at 300 mA g^{-1} while the cathode fabricated with the bulk material exhibited large capacity decay after only 35 cycles.[50]

Nanostructured supporting matrix also has been combined with cathode materials to construct superior conductive network which is usually beneficial to the performances of batteries at high rate. $H_2V_3O_8$ nanowire/graphene composite exhibited an excellent

high-rate capability of 270 mA h g^{-1} at 20 C as well as stable cycling for more than 2000 cycles.[51] Dai et al demonstrated VO_2/rGO (reduced graphene oxide) composite structure can effectively enhance the high-rate capability: the capacity retention of the composite at 16 A g^{-1} was increased by more than five times compared with pure VO_2 powder.[52]

1.5 References

1. Whittingham, M. S. History, Evolution, and Future Status of Energy Storage. *Proc. IEEE*, **2012,** *100*, 1518-1534.

2. Goodenough, J. B., Battery Components, Active Materials for. In *Batteries for Sustainability: Selected Entries from the Encyclopedia of Sustainability Science and Technology*, Brodd, R. J., Ed. Springer New York: New York, NY, 2013; 51-92.

3. Park, J. K., *Principles and Applications of Lithium Secondary Batteries*. Wiley-VCH: Germany, 2012.

4. Winter, M.; Barnett, B.; Xu, K. Before Li Ion Batteries. *Chem. Rev.*, **2018,** *118*, 11433-11456.

5. Chen, H.; Ling, M.; Hencz, L.; Ling, H. Y.; Li, G.; Lin, Z.; Liu, G.; Zhang, S. Exploring Chemical, Mechanical, and Electrical Functionalities of Binders for Advanced Energy-Storage Devices. *Chem. Rev.*, **2018,** *118*, 8936-8982.

6. Liu, J.; Wang, J.; Xu, C.; Jiang, H.; Li, C.; Zhang, L.; Lin, J.; Shen, Z. X. Advanced Energy Storage Devices: Basic Principles, Analytical Methods, and Rational Materials Design. *Adv. Sci.*, **2018,** *5*, 1700322.

7. Cano, Z. P.; Banham, D.; Ye, S.; Hintennach, A.; Lu, J.; Fowler, M.; Chen, Z. Batteries and fuel cells for emerging electric vehicle markets. *Nat. Energy*, **2018,** *3*, 279-289.

8. Wang, N.; Tang, L.; Pan, H. A global comparison and assessment of incentive policy on electric vehicle promotion. *Sustain. Cities Soc.*, **2019,** *44*, 597-603.

9. Zhang, X.; Xie, J.; Rao, R.; Liang, Y. Policy Incentives for the Adoption of Electric Vehicles across Countries. *Sustainability*, **2014,** *6*, 8056.

10. Sierzchula, W.; Bakker, S.; Maat, K.; van Wee, B. The influence of financial incentives and other socio-economic factors on electric vehicle adoption. *Energy Policy*, **2014,** *68*, 183-194.

11. Li, W.; Long, R.; Chen, H.; Geng, J. A review of factors influencing consumer intentions to adopt battery electric vehicles. *Renew. Sust. Energ. Rev.,* **2017,** *78*, 318-328.

12. Rezvani, Z.; Jansson, J.; Bodin, J. Advances in consumer electric vehicle adoption research: A review and research agenda. *Transp. Res. D,* **2015,** *34*, 122-136.

13. Liu, J.; Zhang, J.-G.; Yang, Z.; Lemmon, J. P.; Imhoff, C.; Graff, G. L.; Li, L.; Hu, J.; Wang, C.; Xiao, J.; Xia, G.; Viswanathan, V. V.; Baskaran, S.; Sprenkle, V.; Li, X.; Shao, Y.; Schwenzer, B. Materials Science and Materials Chemistry for Large Scale Electrochemical Energy Storage: From Transportation to Electrical Grid. *Adv. Funct. Mater.,* **2013,** *23*, 929-946.

14. Pasta, M.; Wessells, C. D.; Huggins, R. A.; Cui, Y. A high-rate and long cycle life aqueous electrolyte battery for grid-scale energy storage. *Nat. Commun.,* **2012,** *3*, 1149.

15. Yang, Z.; Zhang, J.; Kintner-Meyer, M. C. W.; Lu, X.; Choi, D.; Lemmon, J. P.; Liu, J. Electrochemical Energy Storage for Green Grid. *Chem. Rev.,* **2011,** *111*, 3577-3613.

16. Dunn, B.; Kamath, H.; Tarascon, J.-M. Electrical Energy Storage for the Grid: A Battery of Choices. *Science,* **2011,** *334*, 928-935.

17. Ponce de León, C.; Frías-Ferrer, A.; González-García, J.; Szánto, D. A.; Walsh, F. C. Redox flow cells for energy conversion. *J. Power Sources,* **2006,** *160*, 716-732.

18. Skyllas-Kazacos, M.; Chakrabarti, M. H.; Hajimolana, S. A.; Mjalli, F. S.; Saleem, M. Progress in Flow Battery Research and Development. *J. Electrochem. Soc.,* **2011,** *158*, R55-R79.

19. Weber, A. Z.; Mench, M. M.; Meyers, J. P.; Ross, P. N.; Gostick, J. T.; Liu, Q. Redox flow batteries: a review. *J. Appl. Electrochem.,* **2011,** *41*, 1137.

20. Li, X.; Zhang, H.; Mai, Z.; Zhang, H.; Vankelecom, I. Ion exchange membranes for vanadium redox flow battery (VRB) applications. *Energy Environ. Sci.,* **2011,** *4*, 1147-1160.

21. Prifti, H.; Parasuraman, A.; Winardi, S.; Lim, T. M.; Skyllas-Kazacos, M. Membranes for Redox Flow Battery Applications. *Membranes,* **2012,** *2*, 275.

22. Yin, B.; Yu, L.; Jiang, B.; Wang, L.; Xi, J. Nano oxides incorporated sulfonated poly(ether ether ketone) membranes with improved selectivity and stability for vanadium redox flow battery. *J. Solid State Electrochem.,* **2016,** *20*, 1271-1283.

23. Cheng, F.; Liang, J.; Tao, Z.; Chen, J. Functional Materials for Rechargeable Batteries. *Adv. Mater.,* **2011,** *23*, 1695-1715.

24. Teng, X.; Zhao, Y.; Xi, J.; Wu, Z.; Qiu, X.; Chen, L. Nafion/organically modified

silicate hybrids membrane for vanadium redox flow battery. *J. Power Sources,* **2009,** *189*, 1240-1246.

25. Qiao, L.; Zhang, H.; Lu, W.; Xiao, C.; Fu, Q.; Li, X.; Vankelecom, I. F. J. Advanced porous membranes with slit-like selective layer for flow battery. *Nano Energy,* **2018,** *54*, 73-81.

26. Yan, X. H.; Zhou, X. L.; Zhao, T. S.; Jiang, H. R.; Zeng, L. A highly selective proton exchange membrane with highly ordered, vertically aligned, and subnanosized 1D channels for redox flow batteries. *J. Power Sources,* **2018,** *406*, 35-41.

27. Noorden, R. V. The rechargeable revolution: A better battery. *Nature,* **2014,** *507*, 26-28.

28. Lin, D.; Liu, Y.; Cui, Y. Reviving the lithium metal anode for high-energy batteries. *Nat. Nanotechnol.,* **2017,** *12*, 194.

29. Liu, J.; Bao, Z.; Cui, Y.; Dufek, E. J.; Goodenough, J. B.; Khalifah, P.; Li, Q.; Liaw, B. Y.; Liu, P.; Manthiram, A.; Meng, Y. S.; Subramanian, V. R.; Toney, M. F.; Viswanathan, V. V.; Whittingham, M. S.; Xiao, J.; Xu, W.; Yang, J.; Yang, X.-Q.; Zhang, J.-G. Pathways for practical high-energy long-cycling lithium metal batteries. *Nat. Energy,* **2019**.

30. Li, M.; Lu, J.; Chen, Z.; Amine, K. 30 Years of Lithium-Ion Batteries. *Adv. Mater.,* **2018,** *30*, 1800561.

31. Longoni, G.; Panda, J. K.; Gagliani, L.; Brescia, R.; Manna, L.; Bonaccorso, F.; Pellegrini, V. In situ $LiFePO_4$ nano-particles grown on few-layer graphene flakes as high-power cathode nanohybrids for lithium-ion batteries. *Nano Energy,* **2018,** *51*, 656-667.

32. Zhang, C.; Park, S.-H.; O'Brien, S. E.; Seral-Ascaso, A.; Liang, M.; Hanlon, D.; Krishnan, D.; Crossley, A.; McEvoy, N.; Coleman, J. N.; Nicolosi, V. Liquid exfoliation of interlayer spacing-tunable 2D vanadium oxide nanosheets: High capacity and rate handling Li-ion battery cathodes. *Nano Energy,* **2017,** *39*, 151-161.

33. Kim, H.; Lee, E.-J.; Sun, Y.-K. Recent advances in the Si-based nanocomposite materials as high capacity anode materials for lithium ion batteries. *Mater. Today,* **2014,** *17*, 285-297.

34. Casimir, A.; Zhang, H.; Ogoke, O.; Amine, J. C.; Lu, J.; Wu, G. Silicon-based anodes for lithium-ion batteries: Effectiveness of materials synthesis and electrode preparation. *Nano Energy,* **2016,** *27*, 359-376.

35. Tian, H.; Tan, X.; Xin, F.; Wang, C.; Han, W. Micro-sized nano-porous Si/C anodes for lithium ion batteries. *Nano Energy,* **2015,** *11*, 490-499.

36. Chen, D.; Mei, X.; Ji, G.; Lu, M.; Xie, J.; Lu, J.; Lee, J. Y. Reversible Lithium-Ion Storage in Silver-Treated Nanoscale Hollow Porous Silicon Particles. *Angew. Chem. Int. Ed.,* **2012,** *51*, 2409-2413.

37. Manthiram, A.; Fu, Y.; Chung, S.-H.; Zu, C.; Su, Y.-S. Rechargeable Lithium–Sulfur Batteries. *Chem. Rev.,* **2014,** *114*, 11751-11787.

38. Yin, Y.-X.; Xin, S.; Guo, Y.-G.; Wan, L.-J. Lithium–Sulfur Batteries: Electrochemistry, Materials, and Prospects. *Angew. Chem. Int. Ed.,* **2013,** *52*, 13186-13200.

39. Yang, Y.; Zheng, G.; Cui, Y. Nanostructured sulfur cathodes. *Chem. Soc. Rev.,* **2013,** *42*, 3018-3032.

40. Ma, L.; Hendrickson, K. E.; Wei, S.; Archer, L. A. Nanomaterials: Science and applications in the lithium–sulfur battery. *Nano Today,* **2015,** *10*, 315-338.

41. Chen, Y.; Choi, S.; Su, D.; Gao, X.; Wang, G. Self-standing sulfur cathodes enabled by 3D hierarchically porous titanium monoxide-graphene composite film for high-performance lithium-sulfur batteries. *Nano Energy,* **2018,** *47*, 331-339.

42. Liang, X.; Nazar, L. F. In Situ Reactive Assembly of Scalable Core–Shell Sulfur–MnO_2 Composite Cathodes. *ACS Nano,* **2016,** *10*, 4192-4198.

43. Kozen, A. C.; Lin, C.-F.; Pearse, A. J.; Schroeder, M. A.; Han, X.; Hu, L.; Lee, S.-B.; Rubloff, G. W.; Noked, M. Next-Generation Lithium Metal Anode Engineering via Atomic Layer Deposition. *ACS Nano,* **2015,** *9*, 5884-5892.

44. Yan, K.; Lu, Z.; Lee, H.-W.; Xiong, F.; Hsu, P.-C.; Li, Y.; Zhao, J.; Chu, S.; Cui, Y. Selective deposition and stable encapsulation of lithium through heterogeneous seeded growth. *Nat. Energy,* **2016,** *1*, 16010.

45. Shen, F.; Zhang, F.; Zheng, Y.; Fan, Z.; Li, Z.; Sun, Z.; Xuan, Y.; Zhao, B.; Lin, Z.; Gui, X.; Han, X.; Cheng, Y.; Niu, C. Direct growth of 3D host on Cu foil for stable lithium metal anode. *Energy Storage Mater.,* **2018,** *13*, 323-328.

46. Konarov, A.; Voronina, N.; Jo, J. H.; Bakenov, Z.; Sun, Y.-K.; Myung, S.-T. Present and Future Perspective on Electrode Materials for Rechargeable Zinc-Ion Batteries. *ACS Energy Lett.,* **2018,** *3*, 2620-2640.

47. Song, M.; Tan, H.; Chao, D.; Fan, H. J. Recent Advances in Zn-Ion Batteries. *Adv. Funct. Mater.,* **2018,** *28*, 1802564.

48. Ming, J.; Guo, J.; Xia, C.; Wang, W.; Alshareef, H. N. Zinc-ion batteries: Materials, mechanisms, and applications. *Mater. Sci. Eng. R,* **2019,** *135*, 58-84.

49. Li, H.; Yang, Q.; Mo, F.; Liang, G.; Liu, Z.; Tang, Z.; Ma, L.; Liu, J.; Shi, Z.; Zhi, C.

MoS_2 nanosheets with expanded interlayer spacing for rechargeable aqueous Zn-ion batteries. *Energy Storage Mater.,* **2018**.

50. Sambandam, B.; Soundharrajan, V.; Kim, S.; Alfaruqi, M. H.; Jo, J.; Kim, S.; Mathew, V.; Sun, Y.-k.; Kim, J. Aqueous rechargeable Zn-ion batteries: an imperishable and high-energy Zn2V2O7 nanowire cathode through intercalation regulation. *J. Mater. Chem. A,* **2018,** *6*, 3850-3856.

51. Pang, Q.; Sun, C.; Yu, Y.; Zhao, K.; Zhang, Z.; Voyles, P. M.; Chen, G.; Wei, Y.; Wang, X. $H_2V_3O_8$ Nanowire/Graphene Electrodes for Aqueous Rechargeable Zinc Ion Batteries with High Rate Capability and Large Capacity. *Adv. Energy Mater.,* **2018,** *8*, 1800144.

52. Dai, X.; Wan, F.; Zhang, L.; Cao, H.; Niu, Z. Freestanding graphene/VO_2 composite films for highly stable aqueous Zn-ion batteries with superior rate performance. *Energy Storage Mater.,* **2019,** *17*, 143-150.

Chapter 2: Hierarchical structural designs of ion exchange membranes for flow batteries

2.1 Introduction

The utilization of renewable resources, such as wind, solar, and tides, has been growing rapidly. This growth is driven by the increasing energy demand and concerns regarding carbon emissions;[1-4] however, large-scale energy storage solutions are required due to the intermittent nature of renewable resources.[5-6] Redox flow batteries (RFBs) are one of the promising candidates due to their low cost, long life, rapid response, high mobility and flexibility.[5-13] RFBs store energy in two solutions with different redox couples. The positive and negative electrodes are separated by a selective ion exchange membrane (IEM), which prevents the mixing of active species. Most of the leading flow batteries with chemistries such as all-vanadium, all-iron, and iron–chromium utilize cation exchange membranes (CEMs).[2, 5, 9-15] Anion exchange membranes (AEMs) have also been used, especially for lowering crossover when cations serve as the active species.[3, 9-10, 14-15]

Perfluorinated polysulfonic acid (PFSA) membranes, such as Nafion, are the most widely used CEMs in RFBs due to their high conductivity and good chemical and thermal stabilities.[10, 14-16] However, Nafion membranes suffer from the crossover of active species, leading to severe self-discharge and decreased energy efficiency.[2, 7, 17-19] Various strategies have been proposed to fabricate new composite membranes with reduced crossover.[20] Physical blending with inorganic particles,[21-24] nanotubes,[25-26] graphene,[27-29] metal–organic frameworks (MOFs), and polymers has been extensively studied.[30-33] The

crossover rate can be reduced by these added materials via reducing mobile water transport and the corresponding leakage of hydrated redox-active ions.[14] Besides the simple mixing method, fillers such as SiO_2 and TiO_2 can also be synthesized during the membrane formation process via the sol-gel method to achieve uniform distribution.[34-37] In the "infiltration method", fillers are formed *in situ* by infiltrating precursors into an existing polymer membrane, resulting in well-dispersed and extremely small particles inside the hydrophilic ionic cluster regions of phase-segregated polymer membranes.[20, 38-40] Reduced crossover rates can be achieved by the decreased size of the ionic cluster regions. Surface modification, mostly with organic coatings serving as highly selective layers, has been used to reduce the crossover of active species as well.[41-44]

Inorganic ion conductors are ideal candidates to serve as ion exchange membranes. While perfect selectivity is theoretically possible, most of these conductors tend to be brittle and are difficult to handle and use. This difficulty can be circumvented by supporting thin films of ion conductors on porous polymer substrates. Unfortunately, a bilayer inorganic-polymer structure has not been widely adopted due to difficulties in integrating materials with significant differences in mechanical properties. Upon exposure to liquids, the polymer tends to swell, while the inorganic layer does not swell. This mismatch results in cracking, delamination, and failure of the membrane.

Here, we developed a composite cation exchange membrane with a hierarchical structure; it consisted of a polymer membrane with tungsten oxide filling the ionic cluster

region and a dense tungsten oxide coating layer on the polymer surface (Figure 2-1). This hierarchical structure simultaneously enabled both high selectivity and conductivity during use in a flow battery. Tungsten oxide hydrates ($H_xWO_3 \cdot yH_2O$) have been reported to show high proton conductivity (~0.1 S cm^{-1}, 25 ℃) and are formed *in situ* in the ionic clusters of polymer membranes.[45-47] By replacing water in the ionic clusters with oxides, we achieve several advantages. (1) Decrease in the permeability of active species: crossover of active species, such as Fe, Cr, and V ions, primarily relies on hydrated ionic clusters, which cannot permeate through the oxide structure. (2) Enhanced mechanical stability of the membrane: interactions between the filled oxide and polymer chains result in denser polymer packing and structural reinforcement. (3) Suppressed swelling of the polymer membrane via the interaction between oxide and polymer chain and decreased water uptake: a low swelling ratio is essential for the polymer membrane to be integrated with a rigid oxide coating layer without suffering from delamination and cracking. The dense oxide layer was coated via the sol-gel method on the polymer/oxide composite membrane. Tungsten oxide hydrates have been reported to have a layered structure with water molecules bonded between the layers, which can enable efficient proton conduction through the hydrogen bond network.[46] Proton insertion/extraction reactions, such as $WO_3 + xH^+ + xe^- \leftrightarrow H_xWO_3$, convert tungsten oxide into tungsten bronze (H_xWO_3, $0 < x < 1$). Protons are conducted through the movement of proton vacancies.[48] Potassium ions are conducted through a similar solid-state ion conduction mechanism. However, multivalent

ions, such as Fe, Cr, and V, with high charge densities have strong interactions with water molecules, which make them too bulky to be inserted into the lattice structure of tungsten oxide hydrates. Nafion was used as a test case for the hierarchical structure, and future experiments can allow for further applications of this strategy to other polymer membranes at lower costs. Combining the oxide-in-polymer and oxide-on-polymer structures has promising potential for enhancing the performance of a variety of membranes.

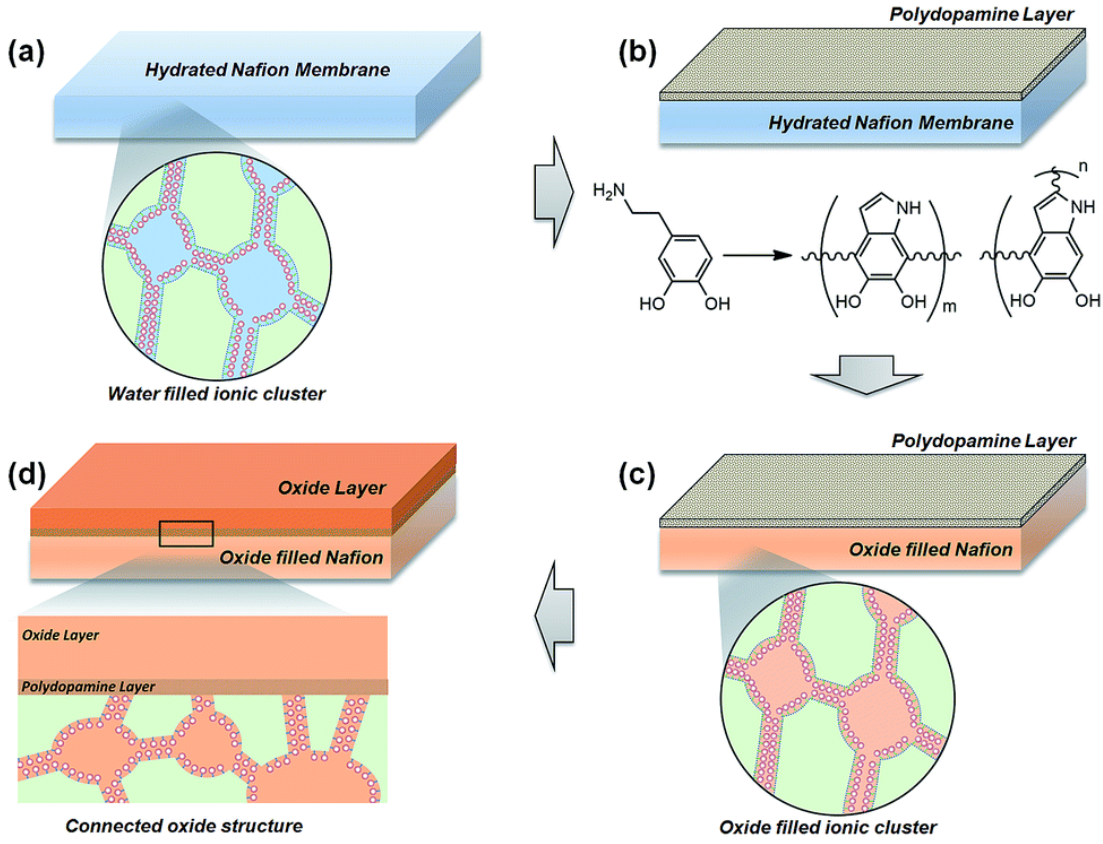

Figure 2-1 Fabrication of tungsten oxide/Nafion hierarchical composite membrane (h-DNf/oxide): (a) blank hydrated Nafion membrane; (b) polydopamine coating (DNf); (c) *in situ* formation of tungsten oxide in hydrophilic ionic cluster regions of Nafion membrane (c-DNf/oxide); (d) tungsten oxide coating on the surface (h-DNf/oxide). Green: fluorocarbon backbones of Nafion; red spheres: sulfonic acid groups of Nafion.

2.2 Fabrication of hierarchical composite membrane

Figure 2-1 shows the fabrication steps for the hierarchical membrane structure. A hydrated Nafion membrane is coated with a thin polydopamine layer (DNf) to improve the hydrophilicity of the surface. DNf is then filled with tungsten oxide in its hydrophilic ionic cluster regions, resulting in a composite structure (c-DNf/oxide). A dense tungsten oxide film is then coated onto c-DNf/oxide to form the final membrane (h-DNf/oxide).

In order to realize the hierarchical structure, strong adhesion at the interface between the oxide coating and Nafion is essential. However, Nafion has a hydrophobic surface due to the perfluoroalkane backbone structure. To enable tungstic acid aqueous solution to wet the Nafion surface, surface modification is required to render it hydrophilic. Inspiration was drawn from biological systems such as mussels that adhere to rocks through the use of dopamine.[49-50] Dopamine monomers are readily oxidized in air under basic pH conditions at room temperature to self-polymerize.[42, 51] The polydopamine layer adheres strongly to almost any material, including PTFE and other anti-fouling materials.[49] Here, we utilized polydopamine as the adhesive layer to enhance the interaction between the Nafion membrane and tungsten oxide coating layer and its hydrophilicity to facilitate the coating process. The polydopamine layer formed on Nafion was presumably very thin (~10 nm based on the literature)[52] and could not be observed in the cross-sectional SEM images (Figure 2-11). A successful coating process was visually confirmed as the clear, transparent Nafion membrane became brown and

semi-transparent (Figure 2-10); it was also confirmed by a change in the surface wetting properties. The contact angle of the Nafion membrane decreased from 89 ° to 61 ° after polydopamine coating (Figure 2-12).

Tungstic acid, which becomes tungsten oxide at an elevated temperature or at a low pH, is the precursor to both c- and h-DNf/oxide structures. The acid was synthesized at around 25 ℃ through the reaction of tungsten powder with hydrogen peroxide. Nano-sized particles were formed as the aging progressed and then served as nucleation sites during the transformation from tungstic acid to tungsten oxide, thus enhancing the formation of the coating layer.

A c-DNf/oxide structure was achieved by filling the ionic channels and clusters with the oxide precursor. Due to the small sizes of the ionic clusters (~5 nm) in Nafion,[53] directly soaking the dry membrane was ineffective; therefore, an infiltration method was used. The membrane was first soaked in methanol, causing it to swell; then, methanol was exchanged after soaking in the precursor solution. While there was no noticeable change in the color of the membrane after the exchange with the tungstic acid solution, the membrane became opaque and dark brown after a curing process, during which the precursor tungstic acid transformed into solid tungsten oxide. This indicated the successful filling of tungsten oxide into the polymer membrane matrix (Figure 2-10). Repeated solvent exchanges and curing further increased the oxide loading amount in Nafion with infiltrated tungsten oxide (c-DNf/oxide).

h-DNf/oxide was prepared by a simple dip-coating method followed by a curing process. As a result of the enhanced hydrophilicity due to the polydopamine coating, the surface of DNf was readily wetted when dipped in a tungstic acid solution. The solution formed a uniform thin liquid layer covering the entire surface when the membrane was pulled out of the solution. During the curing process, an elevated temperature promoted the solidification of the precursor solution layer, while humidity kept the membrane hydrated to avoid shrinkage and possible cracking or delamination of the surface oxide layer due to mismatch in the size changes between Nafion and oxide. Smooth and uniform dark-brown layers were coated on the membrane after repeated coating and curing processes (Figure 2-15 (b)). The quality of the coating was confirmed by SEM; the film is uniform and crack-free (Figure 2-2 (a and b)). At a very high magnification, the coating layer is found to be formed by the aggregation of small particles of 5-15 nm size (Figure 2-11 (b)). Additionally, a membrane with a tungsten oxide layer only on the surface but not in the bulk (l-DNf/oxide) was prepared by directly coating DNf to confirm the contribution of the oxide-in-polymer structure to the stability of the oxide-on-polymer structure (Figure 2-15).

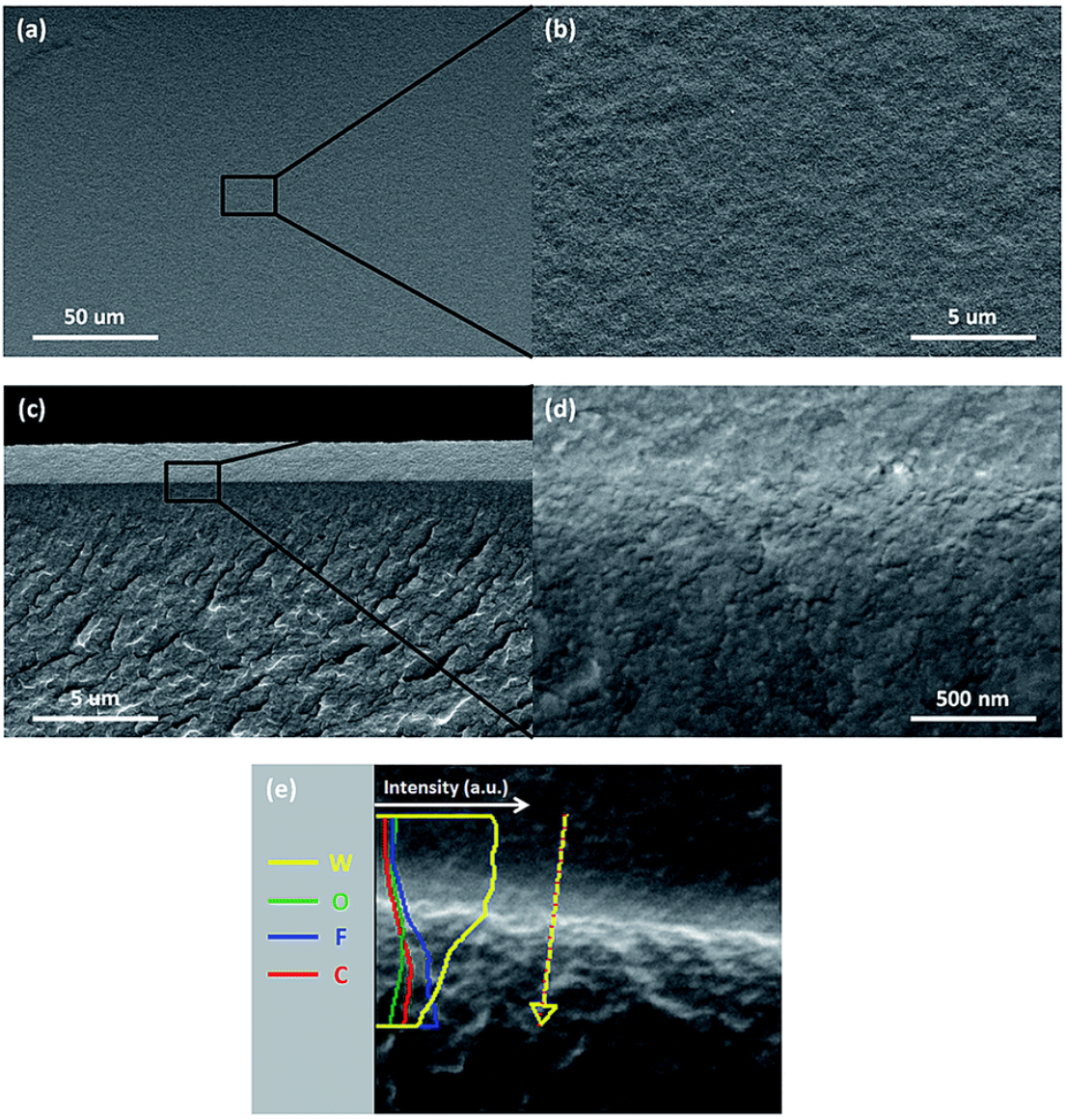

Figure 2-2 SEM images of h-DNf/oxide: (a, b) surface; (c, d) cross-sectional; (e) line-scan EDX at the interface of tungsten oxide coating layer and Nafion membrane.

2.3 Characterization of hierarchical composite membrane

EDX mapping was conducted on the surface of h-DNf/oxide (Figure 2-13). Tungsten and oxygen are distributed homogenously in the coating layer. Cross-sectional SEM images also clearly show the dense and uniform coating layer when EDX mapping is conducted on the surface of h-DNf/oxide (Figure 2-13). Tungsten and oxygen are distributed homogenously in the coating layer. Cross-sectional SEM images also clearly show the dense and uniform coating layer with thickness of 1.6 μm, confirming that the structure is not porous even though it is formed from aggregation of particles (Figure 2-2 (c and d)). The interface between the supporting Nafion membrane and coating layer is of exceptional quality with no visible voids, and the boundary at the interface is not visible, as observed in the high-magnification SEM image (Figure 2-2 (d)). Line-scan EDX shows a gradual compositional gradient across the interface, most noticeably for W (Figure 2-2 (e)). This observation confirmed that our original design has been realized: the tungsten oxide phase is a continuous film on the surface but extends deeply into the Nafion structure. Such a structure is expected to contribute to a robust composite membrane. Such excellent connection and adhesion can mitigate possible delamination at the interface, which is a critical problem for multilayered composite materials. EDX was also conducted on the cross-section of h-DNf/oxide (Figure 2-14). Low-magnification EDX mapping shows that the bulk polymer is mainly composed of carbon, oxygen, fluorine, and sulfur. The surface coating layer contains concentrated tungsten and oxygen,

while tungsten is also uniformly distributed in the bulk polymer matrix, further confirming the bilayer oxide-in-polymer and oxide-on-polymer structures.

XRD was performed to investigate the structure of the membranes (Figure 2-3). The shifts in the Nafion peaks for h-DNf/oxide from 16.83 ° and 39.11 ° to 18.11 ° and 39.98 °, respectively, indicate denser packing of the polymer chains due to the interaction with tungsten oxide. The peak at 23.83 ° matches with several different types of tungsten oxide crystalline structures. As a result, the specific structure of filled tungsten oxide in Nafion cannot be determined based on XRD data. Further characterizations were performed to confirm the structure.

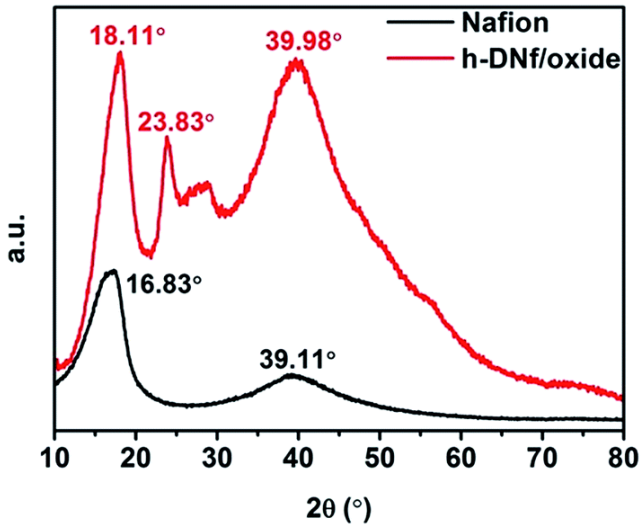

Figure 2-3 XRD of Nafion and h-DNf/oxide.

FTIR spectra were used to examine the chemical structures of Nafion and h-DNf/oxide (Figure 2-4). The peaks at 1200, 1144, and 512 cm^{-1} are related to the C-F bonds on the Nafion polymer backbone. C-O-C and C-S bonds on the side chain lead to

twin peaks at 980 and 968 cm^{-1} and a weak peak at 880 cm^{-1} respectively. The shoulders at 1300 and 1144 cm^{-1} are assigned to the SO_3^- group. For h-DNf/oxide, the peaks in the range of 500-900 cm^{-1} are assigned to the W-O bond. Due to covering by a dense tungsten oxide coating layer, all peaks from Nafion decrease significantly. Raman spectroscopy was also performed on h-DNf/oxide (Figure 2-4 (b)). The C-C bond from the Nafion polymer backbone exhibits a broad peak at 1370 cm^{-1}. The peaks observed at 1000, 690, 254, and 130 cm^{-1} correspond to W=O, O-W-O, W-O-W, and W-W bonds. The peak at 800 cm^{-1}, also corresponding to the O-W-O bond, is associated with the monoclinic structure of tungsten oxide. It is thus concluded that tungsten oxide is successfully formed in the ionic clusters and its structure is probably monoclinic.

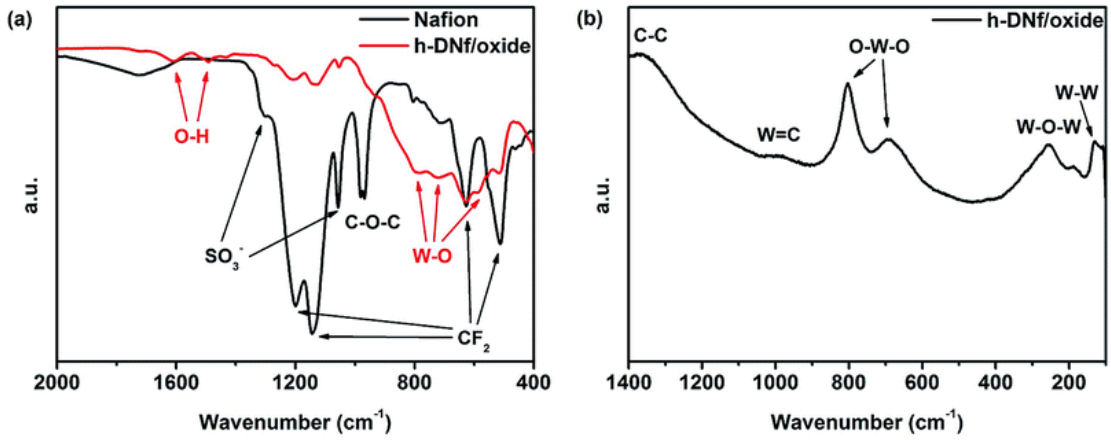

Figure 2-4 Spectra of Nafion and h-DNf/oxide: (a) FT-IR; (b) Raman.

The thermal properties and compositions of the membranes were investigated by TGA (Figure 2-5). Both blank Nafion and h-DNf/oxide exhibited three-step thermal degradation: loss of water during the first step before 270 ℃; desulfonation of Nafion

during the step around 350 ℃; and decomposition of the Nafion polymer backbone during the last step above 400 ℃. For both membranes, the first step can be ignored as a result of pre-drying. After incorporating tungsten oxide into Nafion, the peaks of the second and third steps in the derivative thermal gravimetric curves shift from 363.9 ℃ and 448.9 ℃ to 377.0 ℃ and 469.5 ℃, respectively (Figure 2-5 (b)). The enhanced thermal stability of h-DNf/oxide provides evidence for the interaction between the oxide and polymer. The residual weight indicates that the tungsten oxide loading is 6.6%.

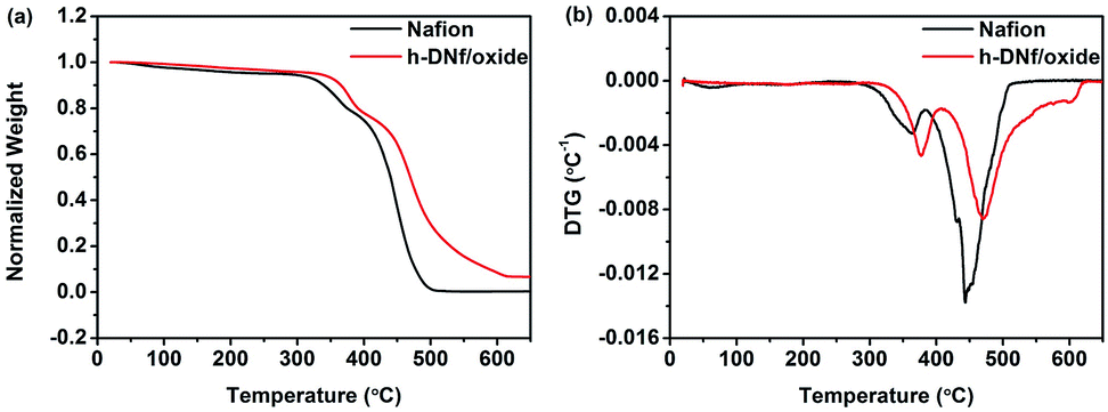

Figure 2-5 Thermogravimetric analysis of Nafion and h-DNf/oxide: (a) TG; (b) DTG.

High mechanical stability of PEM is necessary for long-term practical operation of flow batteries. The Nafion membrane in its dry state showed a Young's modulus of 142.5 MPa, yield stress of 7.67 MPa with 8.5% strain, and failure stress of 25.9 MPa with 223.3% strain (Figure 2-6, Table 2-2). The Nafion membrane became much weaker when hydrated; it exhibited Young's modulus of 35.5 MPa, yield stress of 4.95 MPa, and failure stress of 20.4 MPa. The yield strain increased by 2.6 times to 22%; however, the ultimate

strain remained almost the same. A decrease in the Young's modulus and change in the yield point after hydration were due to the high water uptake and swelling ratios of the Nafion membrane. High water content enables faster proton transport but also increases polymer chain mobility, leading to poor mechanical stability. h-DNf/oxide was significantly reinforced, achieving Young's modulus of 148.7 MPa and yield stress of 9.29% at elongation of 9.1%; these performances were superior even when compared with those of dry Nafion membranes. The ultimate strain significantly decreased to only 47.3% without a large drop in the ultimate stress. The coated tungsten oxide layer on the polymer contributed negligibly to the mechanical properties of bulk membrane due to its limited thickness. Tungsten oxide in the polymer probably changed the mechanical properties of the membrane in three aspects: (1) interactions between tungsten oxide and polymer chains suppress chain mobility and increase chain packing density; (2) tungsten oxide filled in ionic clusters forms a continuous rigid oxide network across the polymer matrix, serving as reinforced concrete to achieve outstanding mechanical stability; (3) tungsten oxide replaces water in the hydrated polymer, which can also reduce chain mobility. The mechanical stability of h-DNf/oxide is not only beneficial toward cell operation but also helps prevent the failure of the coating layer caused by mechanical deformation or dimensional variations due to humidity changes.

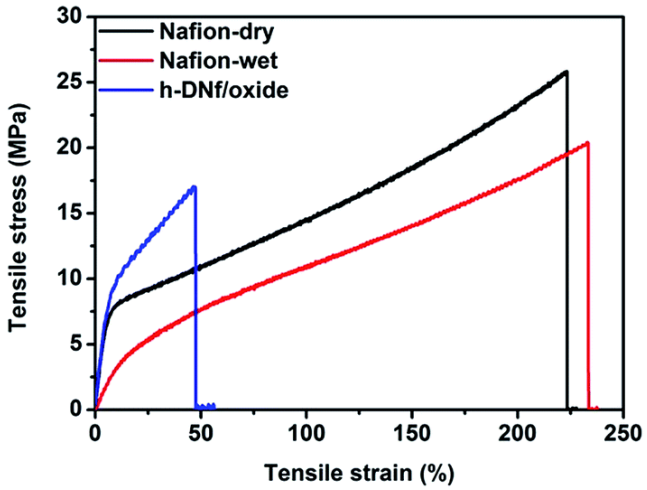

Figure 2-6 Stress-strain curves of Nafion and h-DNf/oxide.

Water uptake (WU) and swelling (SW) are important parameters for composite ion exchange membranes (Table 2-1). While high water uptake usually facilitates ion transport, correspondingly high swelling might compromise the mechanical integrity of the composite structure, particularly for the oxide-on-polymer configuration. The DNf membrane exhibited water uptake of 38.2% and swelling of 44.1%, which were similar to those for baseline Nafion. Due to its very low thickness, the polydopamine coating layer has negligible influence on the water uptake and swelling of the bulk membrane.

Table 2-1 Water uptake, swelling ratio and ion conductivity of Nafion and composite membranes.

	WU [%]	SW [%]	σ_{H^+} [a] [mS/cm]	σ_{H^+}/WU	σ_{K^+} [a] [mS/cm]	σ_{K^+}/WU
Nafion	38.9	46.6	54.1	1.39	8.0	0.21
DNf	38.2	44.1	4.6	0.12	-	-
h-DNf/oxide	12.1	16.9	22.8	1.88	4.6	0.38

All data measured at room temperature. [a] through plane, at 100% RH

Consequently, the significant reduction in the swelling ratio was due to the incorporation of tungsten oxide. Most failures of composite membranes with layered structures, especially those formed by coating rigid inorganic materials on soft polymer supports, are caused by delamination or cracks due to different swelling ratios of the layers. Controlling the water uptake and swelling can effectively enhance the stability as well as mechanical properties of the composite membrane. The tungsten oxide coating layer of l-DNf/oxide exhibited dramatic delamination after soaking in DI water for 24 hours, while h-DNf/oxide maintained its original structure after one week, confirming the contribution of infiltrated tungsten oxide for membrane stability (Figure 2-15).

Ionic conductivities (σ) were measured by a through-plane two-probe method at the hydrated state (Table 2-1). The proton conductivity (σH^+) of DNf membranes was 4.6 mS cm^{-1}, which was only 8.5% of the conductivity of Nafion (54.1 mS cm^{-1}). The dramatic conductivity drop caused by the additional layer with negligible thickness suggested that the conductivity of polydopamine is very low. Interestingly, after

introducing tungsten oxide, the conductivity of h-DNf/oxide increased to 22.8 mS cm^{-1}, which represented manageable reduction from that of Nafion. Filling polydopamine with proton-conductive tungsten oxide and rebuilding the proton transport pathway probably contributed toward the recovery of conductivity. The ratio of conductivity over water uptake (σ/WU) is a metric that measures the effectiveness of water in promoting ion conduction. The σ_{H+}/WU ratio of h-DNf/oxide was 1.88 when compared with 1.39 for baseline Nafion. Hence, tungsten oxide filling in the ion channels appeared to help enhance water-facilitated proton conduction.

We also measured the potassium ion conductivity (σ_{K^+}) of Nafion and the composite membranes (Table 2-1). For flow batteries such as Fe/Fe and Cr/Fe, KCl is often used as the supporting electrolyte and K^+ transports through the cell membrane. During ion exchange, we expected hydrated tungsten oxide to change into its potassium form. In this regard, hydrated potassium tungsten bronze is well-known. However, their K^+ conductivities have not been well studied. Our measurement indicated conductivity of 8.0 mS cm^{-1} for K^+-exchanged Nafion or 14.8% of the proton conductivity. h-DNf/oxide showed K^+ conductivity of 4.6 mS cm^{-1} or 20.2% of the proton conductivity. The σ_{K^+}/WU value for h-DNf/oxide reached 0.38; in comparison, the value for Nafion was 0.21. The smaller difference in σ/WU for K^+ vs. H^+ when compared with that of Nafion indicated that h-DNf/oxide does not rely much on water to transport ions.

The permeability of active species is another key parameter of CEM for flow batteries. The permeabilities for Fe(II) and Cr(III) ions were measured simultaneously by filling two sides of an H-cell with solutions containing different ions. This represents the discharged state of an Fe/Cr flow battery. The crossover of Cr(III) ions could be visibly observed based on their dark-green color, while the crossover of Fe(II) ions could not be observed since their light-green color is similar to that of Cr(III) ions. h-DNf/oxide showed much smaller crossover for both Fe(II) and Cr(III) ions when compared with baseline Nafion. Figure 2-7 (a) and (b) show the test results for both ions while using three different membranes: baseline Nafion, h-DNf/oxide, and c-DNf/oxide. The Fe(II) ion crossover rate of Nafion is the highest; after 50 hours, it starts to decrease as the solution reaches concentration equilibrium. As shown in Figure 2-8 (a), for both Fe(II) and Cr(III) ions, h-DNf/oxide still maintains a constant low crossover rate after 210 hours, suggesting that the stability of the coating layer is not compromised over extended testing. For h-DNf/oxide, the permeabilities of Fe(II) and Cr(III) ions decrease by an order of magnitude (from 2.66×10^{-7} cm^2 s^{-1} and 8.84×10^{-8} cm^2 s^{-1} to 2.31×10^{-8} cm^2 s^{-1} and 8.34×10^{-9} cm^2 s^{-1}, respectively). Cr(III) ions exhibit lower permeability for both baseline and h-DNf/oxide due to their higher valence state. c-DNf/oxide also exhibited some capability to decrease metal ion crossover; the values were measured to be 8.14×10^{-8} cm^2 s^{-1} and 3.85×10^{-8} cm^2 s^{-1} for Fe(II) and Cr(III) ions, respectively. The permeability difference between the membranes of h-DNf/oxide and c-DNf/oxide can be attributed to

the dense surface of the tungsten oxide layer. Considering the thicknesses of the Nafion membrane and coating layer, the dense tungsten oxide coating layer showed extraordinarily low permeability: 4.88×10^{-10} cm^2 s^{-1} for Fe(II) ions, which is 0.18% of that of baseline Nafion and 1.94% of that of c-DNf/oxide; 1.48×10^{-10} cm^2 s^{-1} for Cr(III) ions, which is 0.17% of that of bare Nafion and 1.77% of that of c-DNf/oxide. An empirical figure of merit (β) is defined as the ratio of conductivity to permeability to demonstrate the ratio between the diffusivities of the desired ions and undesired ions in the membrane. In Figure 2-8 (b), h-DNf/oxide shows increased β of H^+ and K^+ over that of Fe^{2+} and Cr^{3+}. The H^+/Cr^{3+} β value of h-DNf/oxide reaches 2.74×10^9 mS s cm^{-3}. Therefore, hierarchical composite structures considerably enhance the selectivity of membranes.

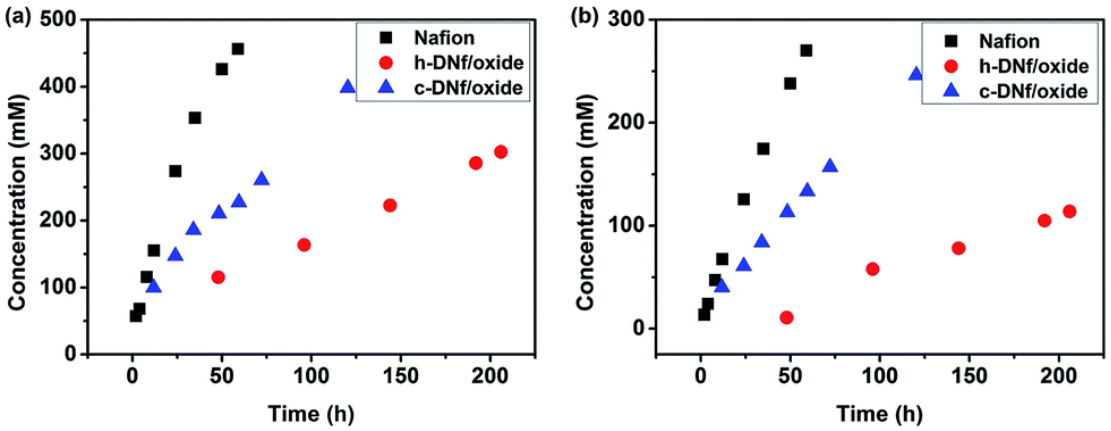

Figure 2-7 Ion-crossover tests of Nafion, c-DNf/oxide, and h-DNf/oxide: (a) Fe(II); (b) Cr(III).

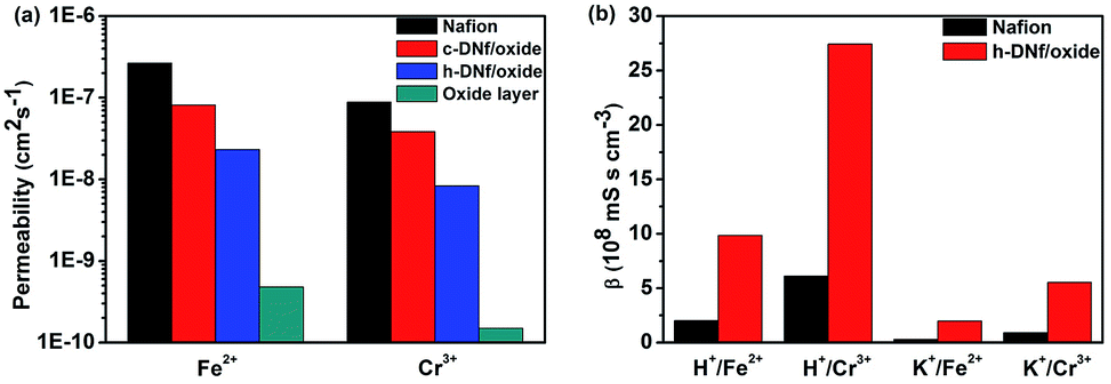

Figure 2-8 Comparisons of (a) ion permeabilities and (b) β values for Nafion and composite membranes. β is defined as the ratio of conductivity to permeability.

2.4 Flow battery performances of hierarchical composite membrane

The flow battery performances of membranes were evaluated in a lab-scale single-cell iron-chromium flow battery (Figure 2-17) as a proof of concept. For the galvanostatic charge and discharge experiments, relatively high capacity to the active membrane area was utilized to emphasize the effect of crossover by prolonging the time of each cycle (Figure 2-9). Although only a limited number of cycles were performed, the

total duration of tests was actually similar to those commonly reported in the literature.[54-56] At a current density of 20 mA cm^{-2}, the flow battery assembled with Nafion as the separator exhibited quick and dramatic discharge capacity decay, retaining only 29.5 mA h after 42.2 hours from the first-cycle capacity of 106.6 mA h. The dark color of the catholyte after cycling indicated the high rate of irreversible crossover, which led to rapidly decreasing capacity (Figure 2-18). Benefiting from the much decreased crossover rate due to the hierarchical composite structure, the capacity decay was mitigated by the dense oxide layer of h-DNf/oxide (Figure 2-20). The flow battery with h-DNf/oxide delivered capacity of 87.9 mA h after 47.9 hours, which was about 3 times that of the battery with Nafion. The color change of the catholyte was also very small. Compared with Nafion, even without the dense surface oxide layer, c-DNf/oxide still showed significant improvement and maintained a discharge capacity of 55.4 mA h. As shown in Figure 2-9 (b), due to severe crossover, the flow battery with Nafion exhibits much larger overpotential than those with either h-DNf/oxide or c-DNf/oxide. Coulombic efficiency is a commonly used performance metric; we should note that for all the three batteries, the coulombic efficiencies were very similar (at about 85%) despite the large difference in capacity retentions. This indicated that the crossover in this case reduced the reversible capacity of batteries, while the coulombic efficiency was determined by other processes such as hydrogen evolution.4 In summary, the overall trend of flow battery performance is consistent with the permeability and selectivity results from static H-cell tests. With no

significant influence from the slight decrease in conductivity, the hierarchical composite structure can considerably mitigate the crossover of active species, which represents an important progress in addressing the well-known trade-off between conductivity and selectivity for flow battery membranes.

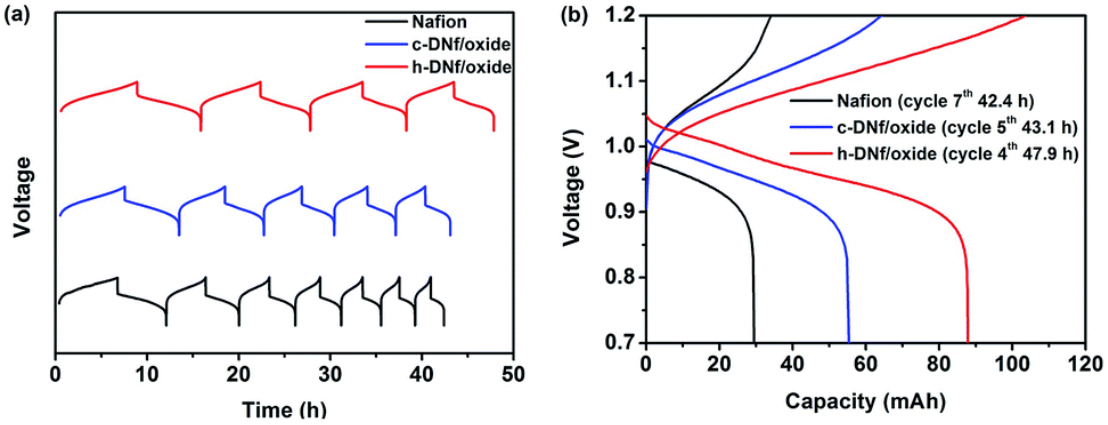

Figure 2-9 Charge–discharge profiles of Nafion and composite membranes at 20 mA cm^{-2}: (a) cycling; (b) comparison after similar cycling times.

2.5 Conclusion

A hierarchical composite ion exchange membrane was developed by integrating Nafion and tungsten oxide. Proton-conducting tungsten oxide infiltrated into ionic clusters of Nafion membranes to reduce water uptake and swelling ratios and enhance stability while maintaining reasonable conductivity. A dense, crack-free tungsten oxide layer was coated onto the surface to reduce the permeability of active species. A stable oxide-on-polymer structure was obtained due to the dimensionally stable oxide-in-polymer composite structure. An order-of-magnitude decrease in the permeabilities of Fe(II) and Cr(III) ions was observed for the hierarchical composite

membrane while maintaining comparable conductivities. The dense oxide coating layer showed three orders of magnitude lower permeability than Nafion. Such a composite membrane with a hierarchical structure provides a strategy to solve the trade-off between conductivity and permeability of ion exchange membranes. The positive effect of the reduced crossover was confirmed in a small lab-scale iron-chromium flow battery with improved capacity retention with cycling and time. Further work is needed to scale up the flow battery and optimize its design to fully realize the benefit of the composite membrane. Nevertheless, our method of fabricating a stable bilayer inorganic-polymer structure has the potential to be applied to many different ion conductors beneficial for energy conversion and storage devices.

2.6 Experimental

Materials: Nafion 117 membrane was purchased from Fuel Cell Store. Tungsten powder (12 μm, 99.9% trace metals basis) and bismuth oxide (Bi_2O_3, 10 μm, 99.9% trace metals basis) were purchased from Sigma-Aldrich. 3-Hydroxytyramine hydrochloride (dopamine, 99%) was purchased from ACROS Organics. Tris(hydroxymethyl)aminomethane (Tris, 99.8%), hydrogen peroxide solution (H_2O_2, 30%), sulfuric acid (H_2SO_4, 95-98%), hydrochloric acid (HCl, 36.5-38%), potassium chloride (KCl, 99%), ferrous chloride tetrahydrate ($FeCl_2 \cdot 4H_2O$, 99%), and chromium chloride hexahydrate ($CrCl_3 \cdot 6H_2O$, 98%) were purchased from Fisher Scientific.

Membrane preparation: Polydopamine was coated onto a Nafion 117 membrane according to a method provided in the literature.[52] A commercial Nafion 117 membrane was pre-treated by boiling in steps of deionized water, starting from pure to a mixture of 3% H_2O_2 and then 0.5 M H_2SO_4 solutions before being stored in deionized water at room temperature. The membrane was then immersed in 79 mL Tris–HCl buffer (pH 8.5), while 1 mL 160 mg mL^{-1} aqueous dopamine solution was added dropwise under mild stirring to induce spontaneous self-polymerization. The coated Nafion membrane (DNf) was taken out after 90 minutes and rinsed with deionized water.

A tungstic acid solution was prepared by slowly dissolving 2.5 g tungsten powder in 30 mL 30% hydrogen peroxide in a room-temperature water bath while being stirred. Excess hydrogen peroxide was removed by placing a small piece of platinum foil in the solution and putting the solution in an oven at 80 ℃ for 20 minutes. The clear solution turned bright yellow.

DNf was soaked in methanol for 24 hours under room temperature, followed by soaking in tungstic acid solution for another 24 hours. Then, the residues on the membrane were wiped off and it was cured for 1 hour under 100% RH and 80 ℃; this environment was created by placing a capped bottle with water in an oven. All the above processes were repeated 3 times to get c-DNf/oxide.

c-DNf/oxide was manually dip-coated in the tungstic acid solution, resulting in double-sided coatings. The coated Nafion was cured in the same way as the previous

method. The coating and curing steps were repeated three times to achieve h-DNf/oxide with the desired thickness of coating.

Membrane characterization: The morphology and thickness of h-DNf/oxide were characterized using scanning electron microscopy (FEI Quanta 250 SEM and Zeiss Sigma 500 SEM for obtaining an ultrahigh magnification image) with atomic composition and elemental mapping analyses performed by an integrated energy-dispersive X-ray (EDX) spectrometer. The chemical composition of the membrane was characterized by Fourier transform infrared spectroscopy (FTIR, Perkin Elmer Spectrum Two) and Raman spectroscopy (Renishaw inVia). The crystal structure of the membrane was investigated by X-ray diffraction (XRD, Bruker D2 Phaser). The thermal stability of the membrane was characterized by thermal gravimetric analysis (TGA, PerkinElmer Pyris 1 TGA) from 25 to 650 ℃ (heating rate: 5 ℃ min^{-1}).

Mechanical properties: The mechanical properties of the membranes were measured using tensile tests (Instron 5960) to generate stress–strain curves at a strain rate of 0.01 mm s^{-1} at room temperature and sampled at 10 Hz rate. Membrane samples were cut into dog-bone-shaped specimens; overall dimensions: 25 mm × 15 mm, gauge dimensions: 15 mm × 2 mm. Dry and wet membranes were pre-treated with the mentioned methods for water uptake measurements.

Water uptake and swelling: Water uptake (WU) and in-plane swelling ratio (SW) of the membranes were calculated based on the percent changes in the wet and dry

weights (WU) and areas (SW). All the measurements were carried out right after the treatment for obtaining accurate data. The dry membranes were dried at 80 ℃ under vacuum for 24 hours to remove residual water and then cooled to room temperature under vacuum. The wet membranes were immersed in deionized water at 60 ℃ for 24 hours to reach complete hydration.

Conductivity: The proton and potassium ion conductivities of the membrane were measured in a conductivity cell using AC impedance spectroscopy, and the membrane resistance was probed with a potentiostat (Bio-Logic, VSP-300) at an oscillating voltage of 20 mV over a frequency range of 7 MHz to 1 Hz. Prior to testing, the membrane sample was fully hydrated in water. The conductivity (σ) was calculated with the following equation:

$$\sigma[\mathrm{mS}\ cm^{-1}] = \frac{L}{RS}$$

L is the distance (cm) between the two electrodes, R is the impedance (Ω) of the membrane, and S is the surface area (cm^2) of the electrodes.

Permeability: An H-cell setup was used for the permeability measurement of Fe(II) and Cr(III) ions. The left reservoir was filled with 1 M Fe(II) ion solution ($FeCl_2$ $4H_2O$) in 2 M HCl, and the right reservoir was filled with 1 M Cr(III) ion solution ($CrCl_3$ $6H_2O$) in 2 M HCl. The geometrical area of the exposed membrane was 1.77 cm^2 and the volume of the solution for each reservoir was 25 mL. Crossover contamination

was measured by ultraviolet-visible spectrometry (UV-vis) on the samples of solutions, which were taken from each reservoir at different time intervals. The samples were analyzed for Fe(II) concentration in right reservoir of Cr(III) solution and for Cr(III) concentration in left reservoir of Fe(II) solution. The measured absorbance of the samples from the H-cell was converted into concentration based on standard absorbance–concentration curves. The permeability was calculated with the following equation:

$$V_B \frac{dc_B(t)}{dt} = A\frac{P}{L}(c_A - c_B(t))$$

here, c_A is the ion concentration in the original reservoir, and $c_B(t)$ is the time-dependent concentration of ions in the other reservoir, which went through the membrane; V_B is the volume of one reservoir, A and L are the area and thickness of the membrane, respectively, and P is the permeability of ions. P is assumed to be independent of the concentration. The permeability of the coating layer was calculated based on the data of h-DNf/oxide and c-DNf/oxide using the following equation:

$$\frac{L_A + L_B}{P_{A+B}} = \frac{L_A}{P_A} + \frac{L_B}{P_B}$$

A represents c-DNf/oxide, B is the dense top oxide layer, and A + B is h-DNf/oxide.

An empirical figure of merit (β) is defined in the form of $\beta = \sigma/P$ to demonstrate the ratio between the diffusivities of the desired and undesired ions in the membrane, i.e., the ratio of proton conductivity (σ) to Fe(II) permeability.

Flow battery test: A flow battery hardware was designed and fabricated in-house. A picture of the device is shown in Figure 2-17 Activated by 3:1 sulfuric acid and nitrate acid for 6 hours at 50 ℃, two pieces of 0.6 cm-thick graphite felt (AvCarb G200) were used as the electrodes. Viton® fluoroelastomer rubber gaskets were used to seal the hardware. The active area of the membrane was 1 × 1 cm^2. Densified and resin-filled impervious graphite plates (Graphtek FC-GR347B) served as the current collectors, which were sandwiched between the copper end plates. The catholyte was prepared by dissolving 1 M $FeCl_2$ in 2 M HCl solution, while the anolyte was prepared by mixing 1 M $CrCl_3$ in 2 M HCl solution with 0.01 M Bi^{3+}. Furthermore, we circulated 8.5 mL catholyte and anolyte at a flow rate of 5 mL min^{-1} by a two-channel peristaltic pump (EW-77921-75, Cole-Parmer). All the flow battery tests were performed at room temperature (25 ℃). The galvanostatic charge and discharge experiments were conducted at 20 mA cm^{-2} with cut-off voltages between 0.7 and 1.2 V. Bismuth, serving as a catalyst for the anodic reaction, was plated onto the anode at 20 mA cm^{-2} before the initial charging.[57]

2.7 Appendix

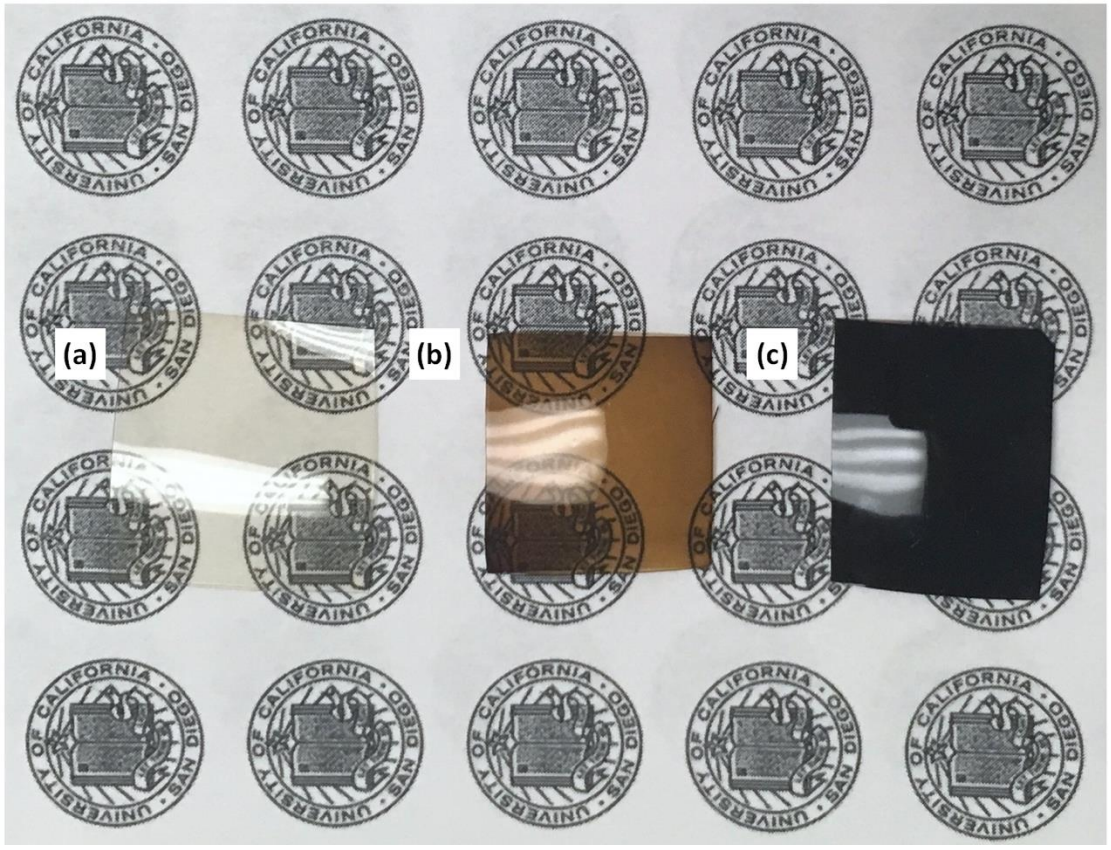

Figure 2-10 Photo of (a) Blank Nafion; (b) h-DNf/oxide; (c) c-DNf/oxide.

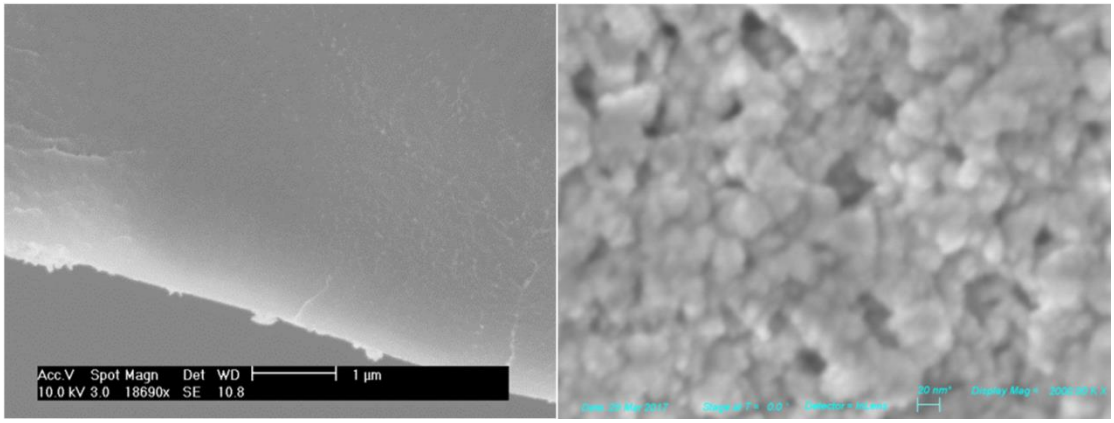

Figure 2-11 SEM images: (a) cross section of DNf; (b) ultra-high magnification surface of h-DNf/oxide.

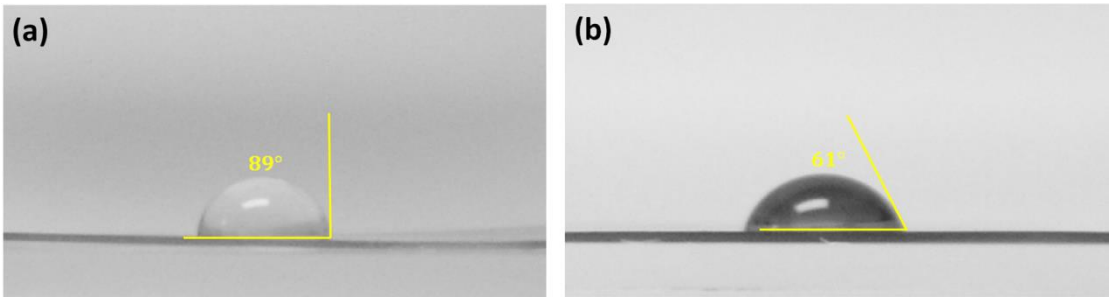

Figure 2-12 Contact angles of (a) Blank Nafion; (b) DNf.

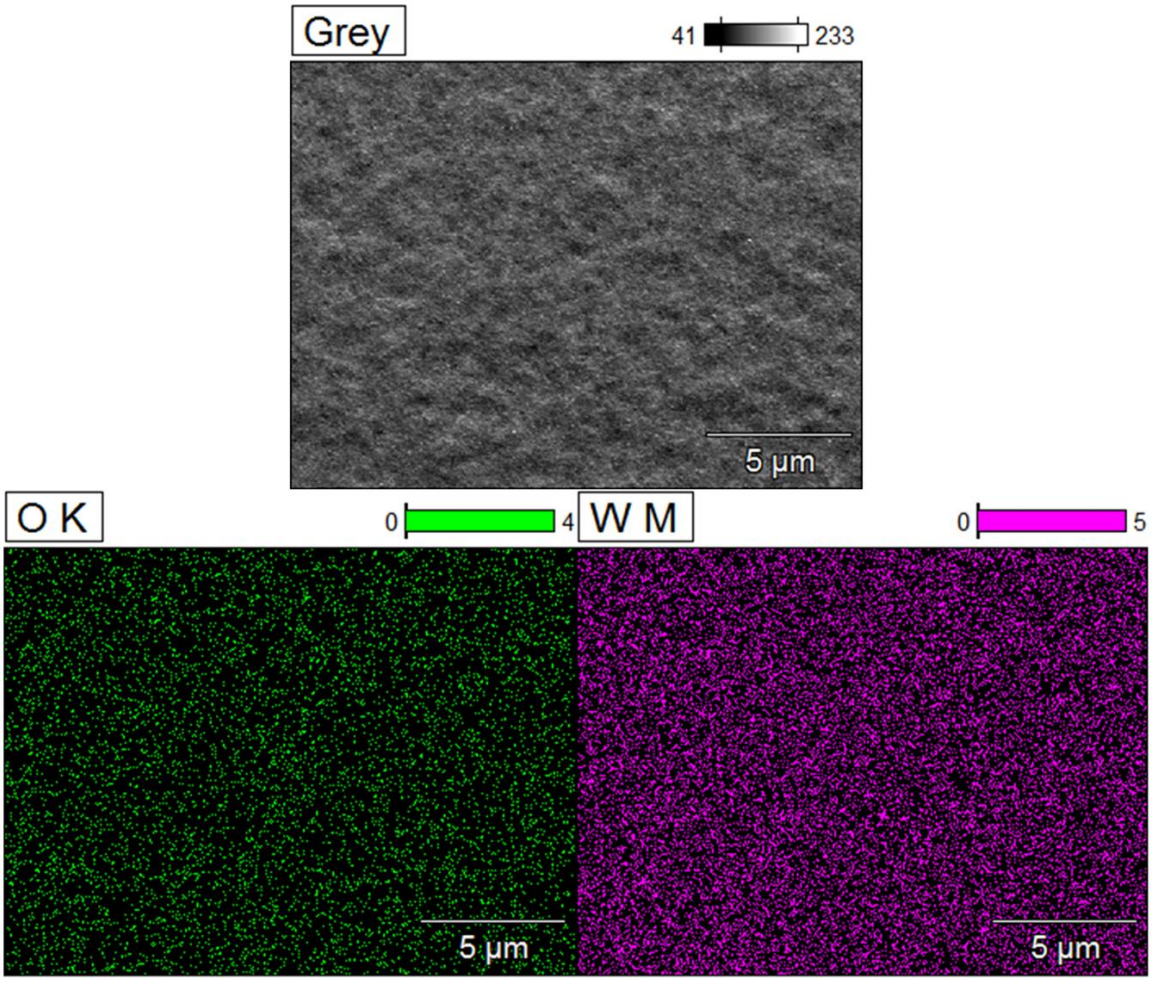

Figure 2-13 Surface EDX of h-DNf/oxide.

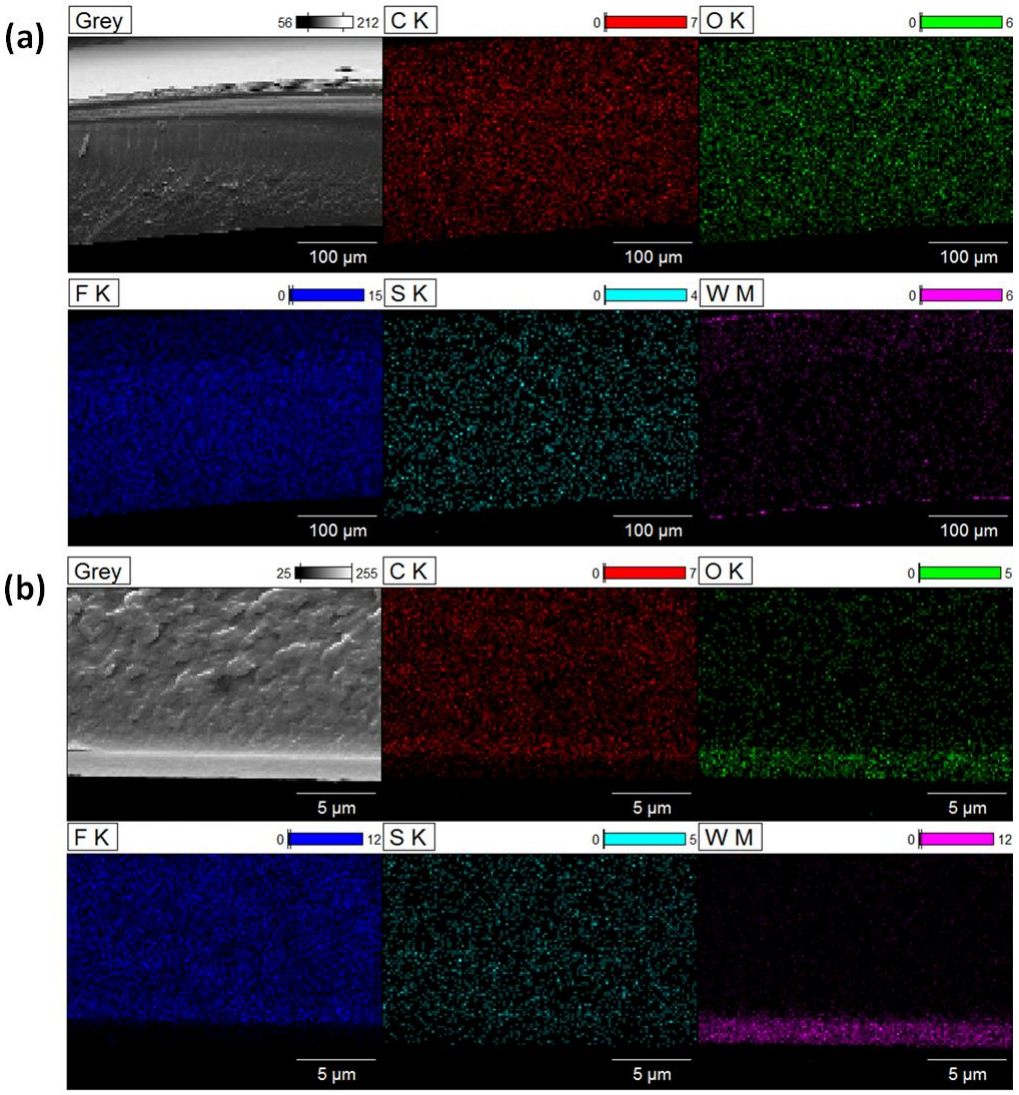

Figure 2-14 Surface EDX of h-DNf/oxide: (a) low magnification; (b) high magnification.

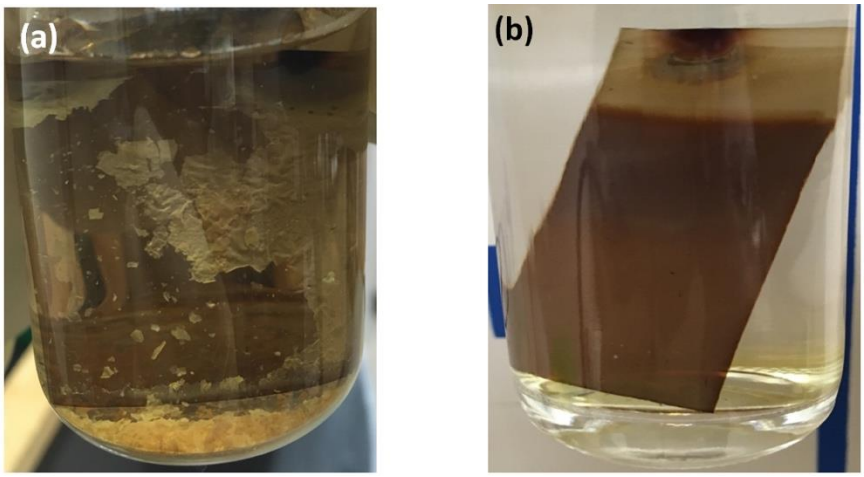

Figure 2-15 Stability of coating layer: (a) l-DNf/oxide soaked in DI water for 24 hours; (b) h-DNf/oxide soaked in DI water for 1 week.

Table 2-2 Mechanical properties of Nafion and h-DNf/oxide.

	Young's modulus [MPa]	Yield stress [MPa]	Yield strain [%)]	Ultimate stress [MPa]	Ultimate strain [%]
Nafion-dry	142.5	7.67	8.5	25.9	223.3
Nafion-wet	35.5	4.95	22.0	20.4	233.4
h-DNf/oxide-wet	148.7	9.29	9.1	17.0	47.3

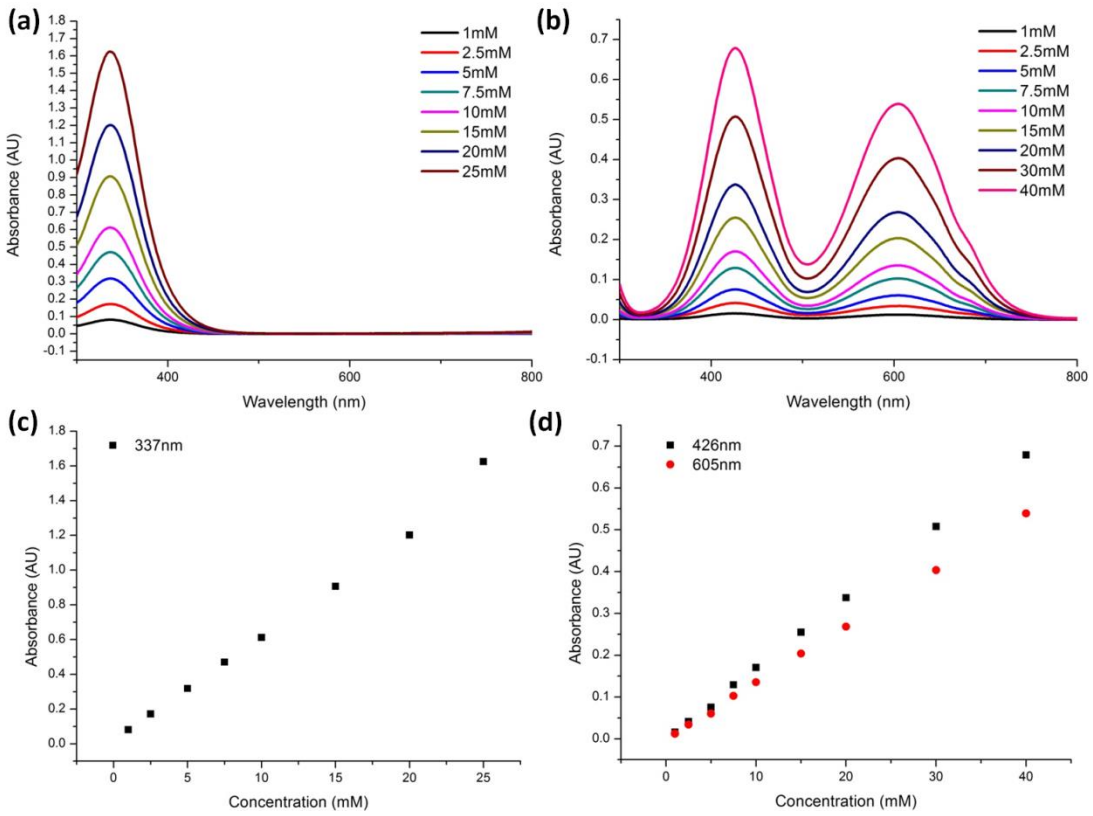

Figure 2-16 UV-vis on standard samples (a) UV-vis spectrums on Fe^{2+} standard samples; (a) UV-vis spectrums on Cr^{3+} standard samples; (c) concentration-absorbance standard curve of Fe^{2+}; (d) concentration-absorbance standard curve of Cr^{3+}.

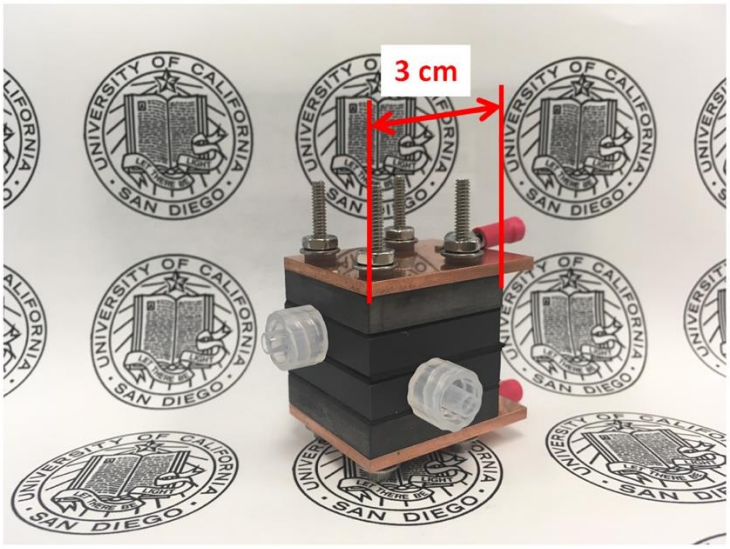

Figure 2-17 Photo of a flow battery hardware designed and fabricated in house.

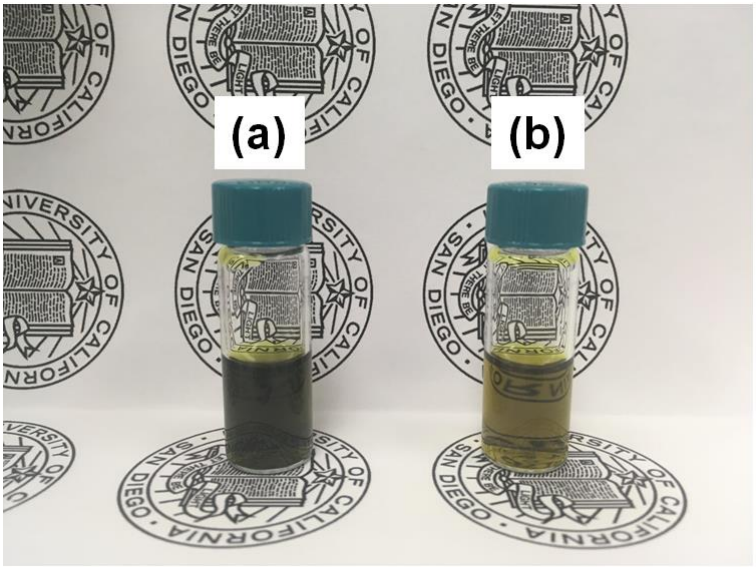

Figure 2-18 Photo of catholytes of flow batteries after cycling for 50 hours at the current density of 20 mA cm^{-2} and the flow rate of 5 ml min^{-1}: (a) Nafion, (b) h-DNf/oxide.

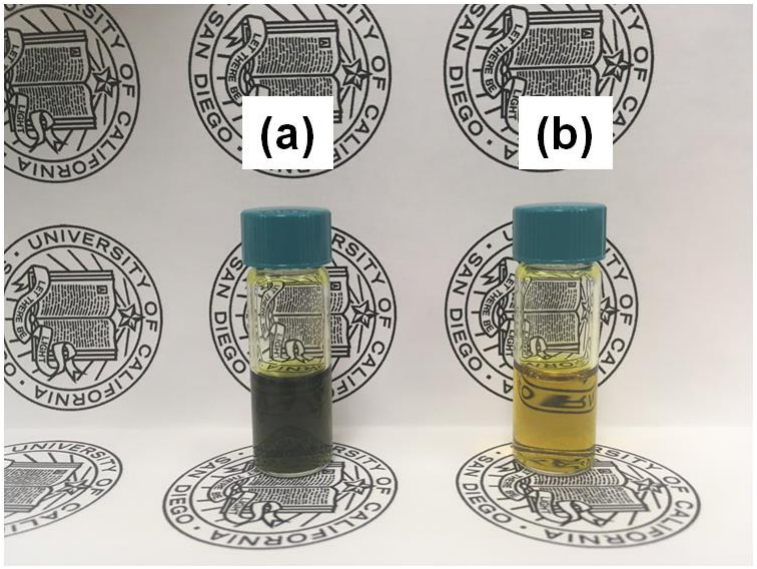

Figure 2-19 Photo of catholytes of flow batteries with no applied current density after 70 hours at the flow rate of 5 ml min^{-1}: (a) Nafion, (b) h-DNf/oxide.

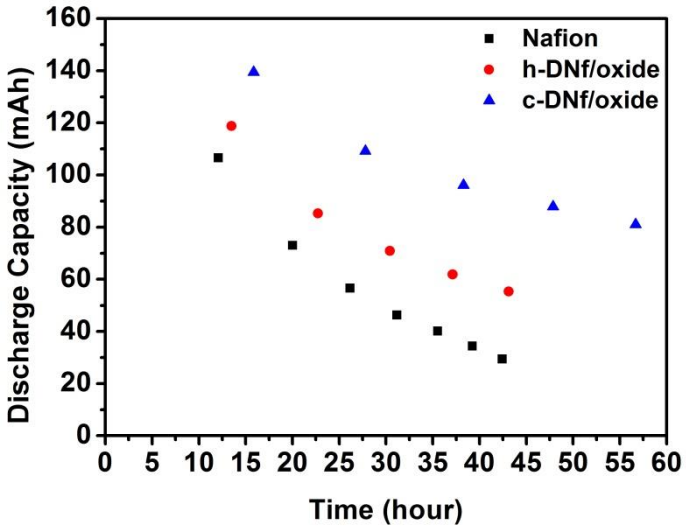

Figure 2-20 Capacity retention over time.

2.8 Acknowledgments

Text, tables, and figures in this chapter, in full, are reprints of materials published in the following paper: Xiujun Yue, Qian He, Hee-dae Lim and Ping Liu*, “Hierarchical structural designs of ion exchange membranes for flow batteries" *J. Mater. Chem. A.*, **2019**, 7, 5794-5802. The dissertation author was the primary researcher for the data presented and was the primary author of this publication. The permissions to reproduce this material were granted by the Royal Society of Chemistry, copyright 2019.

2.9 References

1. Larcher, D.; Tarascon, J. M. Towards greener and more sustainable batteries for electrical energy storage. *Nat. Chem.,* **2014,** *7*, 19.

2. Yang, Z.; Zhang, J.; Kintner-Meyer, M. C. W.; Lu, X.; Choi, D.; Lemmon, J. P.; Liu, J. Electrochemical Energy Storage for Green Grid. *Chem. Rev.,* **2011,** *111*, 3577-3613.

3. Soloveichik, G. L. Flow Batteries: Current Status and Trends. *Chem. Rev.,* **2015,** *115*, 11533-11558.

4. Wang, W.; Luo, Q.; Li, B.; Wei, X.; Li, L.; Yang, Z. Recent Progress in Redox Flow Battery Research and Development. *Adv. Funct. Mater.,* **2012,** *23*, 970-986.

5. Leung, P.; Li, X.; Ponce de Leon, C.; Berlouis, L.; Low, C. T. J.; Walsh, F. C. Progress in redox flow batteries, remaining challenges and their applications in energy storage. *RSC Adv.,* **2012,** *2*, 10125-10156.

6. Ding, C.; Zhang, H.; Li, X.; Liu, T.; Xing, F. Vanadium Flow Battery for Energy Storage: Prospects and Challenges. *J. Phys. Chem. Lett.,* **2013,** *4*, 1281-1294.

7. Parasuraman, A.; Lim, T. M.; Menictas, C.; Skyllas-Kazacos, M. Review of material research and development for vanadium redox flow battery applications. *Electrochim. Acta,* **2013,** *101*, 27-40.

8. Kear, G.; Shah Akeel, A.; Walsh Frank, C. Development of the all - vanadium redox flow battery for energy storage: a review of technological, financial and policy aspects. *Int. J. Energy Res.,* **2011,** *36*, 1105-1120.

9. Weber, A. Z.; Mench, M. M.; Meyers, J. P.; Ross, P. N.; Gostick, J. T.; Liu, Q. Redox flow batteries: a review. *J. Appl. Electrochem.,* **2011,** *41*, 1137.

10. Li, X.; Zhang, H.; Mai, Z.; Zhang, H.; Vankelecom, I. Ion exchange membranes for vanadium redox flow battery (VRB) applications. *Energy Environ. Sci.,* **2011,** *4*, 1147-1160.

11. Skyllas-Kazacos, M.; Chakrabarti, M. H.; Hajimolana, S. A.; Mjalli, F. S.; Saleem, M. Progress in Flow Battery Research and Development. *J. Electrochem. Soc.,* **2011,** *158*, R55-R79.

12. Dunn, B.; Kamath, H.; Tarascon, J.-M. Electrical Energy Storage for the Grid: A Battery of Choices. *Science,* **2011,** *334*, 928-935.

13. Ponce de León, C.; Frías-Ferrer, A.; González-García, J.; Szánto, D. A.; Walsh, F. C. Redox flow cells for energy conversion. *J. Power Sources,* **2006,** *160*, 716-732.

14. Schwenzer, B.; Zhang, J.; Kim, S.; Li, L.; Liu, J.; Yang, Z. Membrane Development for Vanadium Redox Flow Batteries. *ChemSusChem,* **2011,** *4*, 1388-1406.

15. Prifti, H.; Parasuraman, A.; Winardi, S.; Lim, T. M.; Skyllas-Kazacos, M. Membranes for Redox Flow Battery Applications. *Membranes,* **2012,** *2*, 275.

16. Strathmann, H.; Grabowski, A.; Eigenberger, G. Ion-Exchange Membranes in the Chemical Process Industry. *Ind. Eng. Chem. Res.,* **2013,** *52*, 10364-10379.

17. Zhou, X. L.; Zhao, T. S.; An, L.; Zeng, Y. K.; Wei, L. Critical transport issues for improving the performance of aqueous redox flow batteries. *J. Power Sources,* **2017,** *339*, 1-12.

18. Cheng, F.; Liang, J.; Tao, Z.; Chen, J. Functional Materials for Rechargeable Batteries. *Adv. Mater.,* **2011,** *23*, 1695-1715.

19. Liu, J.; Zhang, J. G.; Yang, Z.; Lemmon, J. P.; Imhoff, C.; Graff, G. L.; Li, L.; Hu, J.; Wang, C.; Xiao, J.; Xia, G.; Viswanathan, V. V.; Baskaran, S.; Sprenkle, V.; Li, X.; Shao, Y.; Schwenzer, B. Materials Science and Materials Chemistry for Large Scale Electrochemical Energy Storage: From Transportation to Electrical Grid. *Adv. Funct. Mater.,* **2013,** *23*, 929-946.

20. Li, Y.; He, G.; Wang, S.; Yu, S.; Pan, F.; Wu, H.; Jiang, Z. Recent advances in the fabrication of advanced composite membranes. *J. Mater. Chem. A,* **2013,** *1*, 10058-10077.

21. Lin, C.-H.; Yang, M.-C.; Wei, H.-J. Amino-silica modified Nafion membrane for vanadium redox flow battery. *J. Power Sources,* **2015,** *282*, 562-571.

22. Zhang, J.; Wang, G.; Wang, F.; Zhang, J.; Chen, J.; Wang, R. Sulfonated poly(ether ether ketone)/TiO_2 double-deck membrane for vanadium redox flow battery application. *J. Electroanal. Chem.,* **2016,** *783*, 76-81.

23. Yin, B.; Yu, L.; Jiang, B.; Wang, L.; Xi, J. Nano oxides incorporated sulfonated poly(ether ether ketone) membranes with improved selectivity and stability for vanadium redox flow battery. *J. Solid State Electrochem.,* **2016,** *20*, 1271-1283.

24. Wang, N.; Peng, S.; Wang, H.; Li, Y.; Liu, S.; Liu, Y. SPPEK/WO_3 hybrid membrane fabricated via hydrothermal method for vanadium redox flow battery. *Electrochem. Commun.,* **2012,** *17*, 30-33.

25. Jia, C.; Cheng, Y.; Ling, X.; Wei, G.; Liu, J.; Yan, C. Sulfonated Poly(Ether Ether Ketone)/Functionalized Carbon Nanotube Composite Membrane for Vanadium Redox Flow Battery Applications. *Electrochim. Acta,* **2015,** *153*, 44-48.

26. Aziz, M. A.; Shanmugam, S. Zirconium oxide nanotube–Nafion composite as high

performance membrane for all vanadium redox flow battery. *J. Power Sources,* **2017,** *337*, 36-44.

27. Liu, Y.; Wang, J.; Zhang, H.; Ma, C.; Liu, J.; Cao, S.; Zhang, X. Enhancement of proton conductivity of chitosan membrane enabled by sulfonated graphene oxide under both hydrated and anhydrous conditions. *J. Power Sources,* **2014,** *269*, 898-911.

28. Yu, L.; Lin, F.; Xu, L.; Xi, J. A recast Nafion/graphene oxide composite membrane for advanced vanadium redox flow batteries. *RSC Adv.,* **2016,** *6*, 3756-3763.

29. Su, L.; Zhang, D.; Peng, S.; Wu, X.; Luo, Y.; He, G. Orientated graphene oxide/Nafion ultra-thin layer coated composite membranes for vanadium redox flow battery. *Int. J. Hydrogen Energy,* **2017,** *42*, 21806-21816.

30. Goh, P. S.; Ismail, A. F.; Sanip, S. M.; Ng, B. C.; Aziz, M. Recent advances of inorganic fillers in mixed matrix membrane for gas separation. *Sep. Purif. Technol.,* **2011,** *81*, 243-264.

31. Liu, S.; Sang, X.; Wang, L.; Zhang, J.; Song, J.; Han, B. Incorporation of metal-organic framework in polymer membrane enhances vanadium flow battery performance. *Electrochim. Acta,* **2017,** *257*, 243-249.

32. Wang, J.; Yue, X.; Zhang, Z.; Yang, Z.; Li, Y.; Zhang, H.; Yang, X.; Wu, H.; Jiang, Z. Enhancement of Proton Conduction at Low Humidity by Incorporating Imidazole Microcapsules into Polymer Electrolyte Membranes. *Adv. Funct. Mater.,* **2012,** *22*, 4539-4546.

33. Wang, J.; Zhang, Z.; Yue, X.; Nie, L.; He, G.; Wu, H.; Jiang, Z. Independent control of water retention and acid-base pairing through double-shelled microcapsules to confer membranes with enhanced proton conduction under low humidity. *J. Mater. Chem. A,* **2013,** *1*, 2267-2277.

34. Di Vona, M. L.; Ahmed, Z.; Bellitto, S.; Lenci, A.; Traversa, E.; Licoccia, S. SPEEK-TiO2 nanocomposite hybrid proton conductive membranes via in situ mixed sol–gel process. *J. Membr. Sci.,* **2007,** *296*, 156-161.

35. Yin, Y.; Xu, T.; He, G.; Jiang, Z.; Wu, H. Fabrication of sulfonated poly(ether ether ketone)-based hybrid proton-conducting membranes containing carboxyl or amino acid-functionalized titania by in situ sol–gel process. *J. Power Sources,* **2015,** *276*, 271-278.

36. Xi, J.; Wu, Z.; Qiu, X.; Chen, L. Nafion/SiO2 hybrid membrane for vanadium redox flow battery. *J. Power Sources,* **2007,** *166*, 531-536.

37. Teng, X.; Zhao, Y.; Xi, J.; Wu, Z.; Qiu, X.; Chen, L. Nafion/organic silica modified

TiO_2 composite membrane for vanadium redox flow battery via in situ sol–gel reactions. *J. Membr. Sci.,* **2009,** *341*, 149-154.

38. Tripathi, B. P.; Shahi, V. K. Organic–inorganic nanocomposite polymer electrolyte membranes for fuel cell applications. *Prog. Polym. Sci.,* **2011,** *36*, 945-979.

39. Klein, L. C.; Daiko, Y.; Aparicio, M.; Damay, F. Methods for modifying proton exchange membranes using the sol–gel process. *Polymer,* **2005,** *46*, 4504-4509.

40. Chen, Z.; Holmberg, B.; Li, W.; Wang, X.; Deng, W.; Munoz, R.; Yan, Y. Nafion/Zeolite Nanocomposite Membrane by in Situ Crystallization for a Direct Methanol Fuel Cell. *Chem. Mater.,* **2006,** *18*, 5669-5675.

41. Luo, Q.; Zhang, H.; Chen, J.; Qian, P.; Zhai, Y. Modification of Nafion membrane using interfacial polymerization for vanadium redox flow battery applications. *J. Membr. Sci.,* **2008,** *311*, 98-103.

42. Pan, F.; Jia, H.; Qiao, S.; Jiang, Z.; Wang, J.; Wang, B.; Zhong, Y. Bioinspired fabrication of high performance composite membranes with ultrathin defect-free skin layer. *J. Membr. Sci.,* **2009,** *341*, 279-285.

43. Zhong, S.; Cui, X.; Fu, T.; Na, H. Modification of sulfonated poly(ether ether ketone) proton exchange membrane for reducing methanol crossover. *J. Power Sources,* **2008,** *180*, 23-28.

44. Zhao, Y.; Tang, K.; Liu, H.; Van der Bruggen, B.; Sotto D ́az, A.; Shen, J.; Gao, C. An anion exchange membrane modified by alternate electro-deposition layers with enhanced monovalent selectivity. *J. Membr. Sci.,* **2016,** *520*, 262-271.

45. Hibino, M.; Nakajima, H.; Kudo, T.; Mizuno, N. Proton conductive amorphous thin films of tungsten oxide clusters with acidic ligands. *Solid State Ionics,* **1997,** *100*, 211-216.

46. Li, Y. M.; Hibino, M.; Miyayania, M.; Kudo, T. Proton conductivity of tungsten trioxide hydrates at intermediate temperature. *Solid State Ionics,* **2000,** *134*, 271-279.

47. Tanaka, Y.; Miyayama, M.; Hibino, M.; Kudo, T. Preparation and proton conductivity of WO_3 $2H_2O$/epoxy composite films. *Solid State Ionics,* **2004,** *171*, 33-39.

48. Kumar, P. P.; Yashonath, S. Ionic conduction in the solid state. *Journal of Chemical Sciences,* **2006,** *118*, 135-154.

49. Lee, H.; Dellatore, S. M.; Miller, W. M.; Messersmith, P. B. Mussel-Inspired Surface Chemistry for Multifunctional Coatings. *Science,* **2007,** *318*, 426-430.

50. Lee, H.; Lee, Y.; Statz, A. R.; Rho, J.; Park, T. G.; Messersmith, P. B. Substrate -

Independent Layer‐by‐Layer Assembly by Using Mussel‐Adhesive‐Inspired Polymers. *Adv. Mater.,* **2008,** *20*, 1619-1623.

51. Xiao, M.; Li, Y.; Allen, M. C.; Deheyn, D. D.; Yue, X.; Zhao, J.; Gianneschi, N. C.; Shawkey, M. D.; Dhinojwala, A. Bio-Inspired Structural Colors Produced via Self-Assembly of Synthetic Melanin Nanoparticles. *ACS Nano,* **2015,** *9*, 5454-5460.

52. Wang, J.; Xiao, L.; Zhao, Y.; Wu, H.; Jiang, Z.; Hou, W. A facile surface modification of Nafion membrane by the formation of self-polymerized dopamine nano-layer to enhance the methanol barrier property. *J. Power Sources,* **2009,** *192*, 336-343.

53. Li, J. Y.; Nemat-Nasser, S. Micromechanical analysis of ionic clustering in Nafion perfluorinated membrane. *Mech. Mater.,* **2000,** *32*, 303-314.

54. Zeng, Y. K.; Zhou, X. L.; An, L.; Wei, L.; Zhao, T. S. A high-performance flow-field structured iron-chromium redox flow battery. *J. Power Sources,* **2016,** *324*, 738-744.

55. Zeng, Y. K.; Zhao, T. S.; An, L.; Zhou, X. L.; Wei, L. A comparative study of all-vanadium and iron-chromium redox flow batteries for large-scale energy storage. *J. Power Sources,* **2015,** *300*, 438-443.

56. Zhang, H.; Tan, Y.; Li, J.; Xue, B. Studies on properties of rayon- and polyacrylonitrile-based graphite felt electrodes affecting Fe/Cr redox flow battery performance. *Electrochim. Acta,* **2017,** *248*, 603-613.

57. Wu, C. D.; Scherson, D. A.; Calvo, E. J.; Yeager, E. B.; Reid, M. A. A Bismuth‐Based Electrocatalyst for the Chromous‐Chromic Couple in Acid Electrolytes. *J. Electrochem. Soc.*, **1986,** *133*, 2109-2112.

Chapter 3: A scalable 3D lithium metal anode

3.1 Introduction

Li metal anode is currently being extensively studied to replace graphite in order to further raise the energy density of rechargeable batteries.[1] Li metal anode, however, has been plagued by several well-known issues. Dendritic Li formation during repeated Li plating and stripping results in ever increasing surface area and may short the cell over time and cause safety issues. The loose deposition of Li anode also results in large volume expansion.[2-5] Perhaps the most challenging is the low coulombic efficiency (CE). The continuous loss of active lithium does not satisfy the requirement of long cycling life when limited Li is used in order to achieve high energy density. These challenges have been well reviewed recently. The root causes of these problems are the high reactivity of Li metal and non-uniform Li ion flux.[1]

Several approaches have been presented recently to address these challenges.[6-12] In order to mitigate the lithium metal reaction with the electrolyte, research has identified ether based electrolytes to be more stable than carbonate based ones, resulting in higher coulombic efficiency. Unfortunately, these electrolytes have poor oxidative stability and are usually unsuitable for high voltage, oxide based cathodes.[13-15] Another widely used method is to employ electrolytes (often with additives) that promote the formation of high quality solid electrolyte interface (SEI) formation to protect lithium metal. This method is applicable to the more oxidatively stable, carbonate-based cathodes. For example, Xu simultaneously added $LiAsF_6$ and cyclic carbonate into the electrolyte to

generate a uniform and flexible SEI layer on the Li surface, which contributes to dendrite free Li deposition with enhanced coulombic efficiency.[16] In order to address the large volume changes during Li plating and stripping, other researchers have introduced 3D hosts for Li metal, such as porous Cu, layered reduced graphene oxide, and carbon cloths, among others.[17-19] These 3D hosts not only largely mitigate the volume changes during Li plating and stripping, but also suppress the Li dendrite growth. Although, the large surface area of the 3D host reduces the local current densities, the side reactions become more serious as well. An effective strategy would therefore require combining 3D host design with electrolyte engineering to address all the issues of the Li metal anode.

In this work, a commercial carbonate electrolyte (1 M $LiPF_6$ in 1:1 vol ratio EC/DMC, LP30) is chosen as the baseline. By adding vinylene carbonate and $LiNO_3$, both Li metal morphology and coulombic efficiency are greatly improved. Later, this modified electrolyte is combined with a novel multi-functional 3D composite host for the Li metal anode. As shown in Figure 3-1 (a), this 3D composite host is prepared by simply casting a well-mixed slurry of $LiNO_3$, carbon black, and PVDF on a Cu foil, followed by drying in the oven. As a result of the combination of electrolyte additive and 3D composite host, dense Li chunks with micron-sized particles are observed even at a high current density of 2 mA cm^{-2} after 70 cycles in a carbonate electrolyte. A high coulombic efficiency of 98.4% over 300 cycles has also been achieved at 0.25 mA cm^{-2} for

0.5 mAh cm^{-2}. This work suggests that simultaneous use of electrolyte additives and 3D hosts are necessary to enable stable Li metal anode.

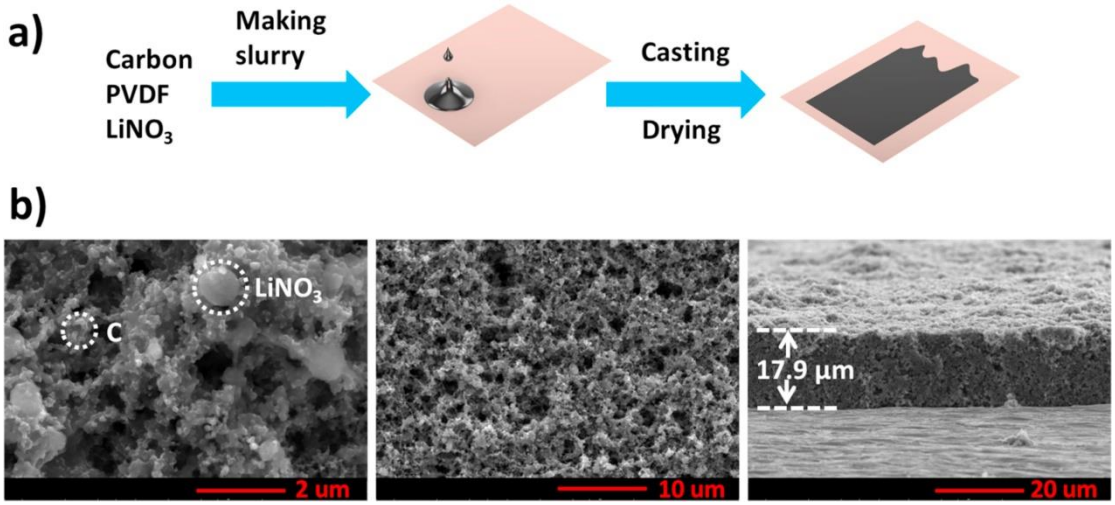

Figure 3-1 (a) The process of making the 3D composite host; (b) SEM images of the 3D $LiNO_3$ composite host.

3.2 Enhanced lithium metal cycling with modified electrolyte.

The coulombic efficiency of Li metal cycling depends on the electrolyte solvent. Due to its high compatibility with oxide based cathodes, it is critical to enhance the Li stability in carbonate based electrolytes. A commercial electrolyte (1 M $LiPF_6$ in 1:1 vol ratio EC/DMC, LP30) was chosen as a baseline electrolyte in this work. Based on previous Si anode research, 5 wt% vinylene carbonate (VC) was chosen as an SEI formation additive in order to improve the uniformity and flexibility of the SEI film on Li surface.[16] The effects of VC additive on Li metal CE were studied by testing Li-Cu coin cells. Li was plated on Cu substrate at 0.5 mA cm^{-2} for 1 mAh cm^{-2}, and then stripped at the same current density until the cell potential reached 1 V. The results of LP30

electrolyte (E1) and LP30 + 5 wt% VC electrolyte (E2) are compared in Figure 3-9. The average CE over 80 cycles is improved from 90.5% to 96.9% with the help of the VC additive.

Our second additive is $LiNO_3$. Previous work has shown that $LiNO_3$ is a universal electrolyte additive in Li-S batteries because it protects the Li metal and reduces the S_n^{2-} shuttle by forming a layer of Li_xNO_y species.[20-21] The concentration of the $LiNO_3$ in ether-based electrolytes for Li-S batteries is usually higher than 0.2 M. Because of the low solubility of $LiNO_3$ in carbonates, $LiNO_3$ has not been widely used in carbonate-based electrolytes yet.[21] The $LiNO_3$ salt was gradually added into the E2 until saturation; the overall concentration of $LiNO_3$ was 0.02 M. As shown in Figure 3-9, this LP30 + 5 wt% VC + 0.02 M $LiNO_3$ (E3) electrolyte further enhanced the CE of Li metal to 97.7%.

In addition to the CE test, the Li deposition morphologies were also investigated in these electrolytes. Li was plated on the Cu substrate at a high current density of 2 mA cm^{-2} for 1 h. Figure 3-2 and Figure 3-11 present the Li morphologies in these electrolytes. The Li plated in E1 is needle-like. Due to the loose deposition, most mossy Li is lost during cell disassembling. It is hard to determine the thickness of the plated Li in E1 through the cross sectional view. The VC promoted Li chunk formation, however, small amounts of dendrites were also observed in E2 at a high current density of 2 mA cm^{-2}. The Li chunk size distribution ranges from 0.5 to 2 μm. The thickness of the

Li film in E2 was 26 µm, which suggests that even though the morphology was improved, the deposition is still incompact. According to theoretical calculations, 2 mAh cm^{-2} of Li corresponds to a thickness of 9.7 µm and the porosity of Li in E2 is thus 62.7%. In the case of E3, the plated Li are all big chunks with sizes between 2 and 5 µm. The Li film was 11.5 µm thick with a low porosity of 15.7%, which indicates a dense Li film was deposited on Cu in E3. All the morphology studies of the deposited Li are consistent with the CE testing data. The bigger Li chunk with denser deposition delivers higher CE. The E3 was used as the optimized electrolyte for the rest of the studies.

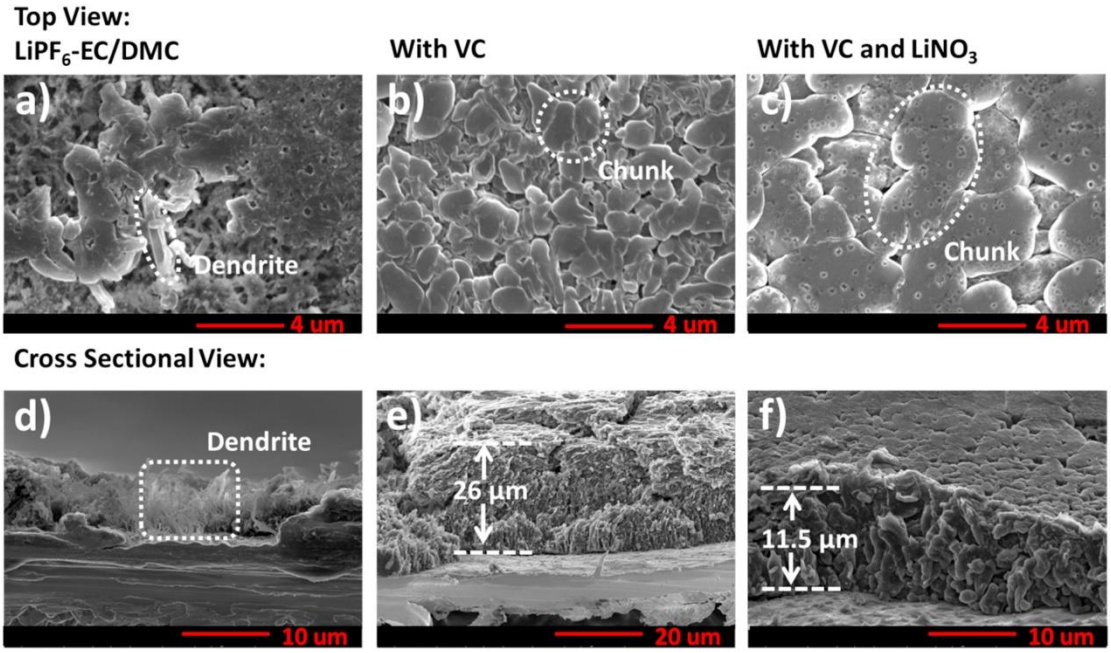

Figure 3-2 SEM images of the deposited Li metal film on Cu foil. (a), (b), (c) are the top view and (d), (e), (f) are the cross-section view of Cu after 1 hour Li deposition at 2 mA cm^{-2} in 1 M $LiPF_6$-EC/DMC electrolyte (E1), 1 M $LiPF_6$-EC/DMC electrolyte with 5 wt% VC (E2), and 1 M $LiPF_6$ + 0.02 M $LiNO_3$-EC/DMC electrolyte with 5 wt% VC (E3), respectively.

3.3 Enhanced lithium metal cycling with multi-functional 3D composite host.

Although electrolyte formulas are effective in improving cycling efficiency, they don't address the volume change issue during Li cycling. The 3D Li host is a promising strategy. However, the current proposed 3D Li hosts are either too complicated to fabricate, or too hard to implement into a real device.[3] Most of the 3D Li hosts only serve as high surface area porous electrode. Here, a multi-functional 3D composite host was designed. The fabrication of this host is similar to the electrode making process in industry, which is schematically showed in Figure 3-1. The SEM images display the porous structure of the host. The porosity of the 3D composite electrode is calculated based on the following equation.

$$\text{Porosity} = \frac{(\boldsymbol{V_{electrode}} - \sum \boldsymbol{V_{component}})}{\boldsymbol{V_{electrode}}} = \frac{\boldsymbol{V_{electrode}} - \boldsymbol{M_{electrode}} \cdot \left(\frac{\boldsymbol{P}_{\text{LN}}}{\boldsymbol{\rho}_{\text{LN}}} + \frac{\boldsymbol{P_C}}{\boldsymbol{\rho_C}} + \frac{\boldsymbol{P_{PVDF}}}{\boldsymbol{\rho_{PVDF}}} \right)}{\boldsymbol{V_{electrode}}}$$

where $V_{component}$ and $V_{electrode}$ are the components ($LiNO_3$, PVDF, and carbon black) and electrode volume, $M_{electrode}$ is the mass of the electrode, and ρ and P are the density and mass fraction of the materials.[22] The densities of the $LiNO_3$, PVDF and carbon black used for calculating the porosity were 2.38, 1.76, and 2.0 g cm^{-3}, respectively. The mass of the electrode is 1.30 mg cm^{-2}, and the thickness of the host is 17.9 μm. The calculated porosity of the 3D host is 66.2%. Based on the porosity of the electrode, this 3D host is theoretically able to store 2.44 mAh Li per cm^2. Once all the pores are filled by Li, the

mass of the deposited Li is calculated to be 0.63 mg cm^{-2}, which corresponds to a high gravimetric capacity of 1264 mAh g^{-1}.

The performance of the 3D composite host was investigated by the CE test in E3. The bare Cu cycled in E3 was chosen as a baseline. Both bare Cu and 3D composite host were discharged versus Li at 0.5 mA cm^{-2} for 4 h, and then the Li was stripped to 1 V at 0.5 mA cm^{-2} for one cycle. Figure 3-11 presents the Li plating and stripping voltage profiles of this conditioning cycle. The purpose of the conditioning cycle is to form an SEI layer on the substrate. The 3D host exhibited a much lower over-potential than the bare Cu, however, the large surface area contributed to the higher irreversibility during this condition cycle. Figure 3-3 systematically compared the CE of both substrates at various current densities after their condition cycles. Figure 3-3 (a) exhibited their CE at 0.25 mA cm^{-2} for 0.5 mAh cm^{-2}. At this mild condition, both substrates showed good stability for a long duration of 300 cycles. The 3D host delivered higher average CE than the bare Cu. The average CEs over 300 cycles were 97.5% and 98.4% for bare Cu and 3D host, respectively. Figure 3-4 shows the Li plating and stripping voltage profiles on both substrates. The voltage difference between the charge and discharge plateaus was only 37.2 mV on 3D host, while a large voltage difference of 69.1 mV was detected on bare Cu. This lower over-potential was attributed to the porous structure in the 3D host, which decreased the local current density. Both substrates were evaluated at harsher conditions that were closer to the current densities in real batteries. When they were cycled at

1 mA cm^{-2} for 1 mAh cm^{-2}, the bare Cu cell started to short before 80 cycles, while the 3D host showed stable Li plating and stripping over 200 cycles. Figure 3-3 (c) and Figure 3-12 show their CEs and voltage profiles. The bare Cu achieved a CE of only 95.7% for 79 cycles. As a comparison, the 3D host delivered a high CE of 97.9%. The bare Cu cycled at 2 mA cm^{-2} for 2 mAh cm^{-2} presented a much lower cycle life; the Li-Cu cells were usually shorted before 20 cycles. On the other hand, the 3D host still delivered a good CE of 97.1%.

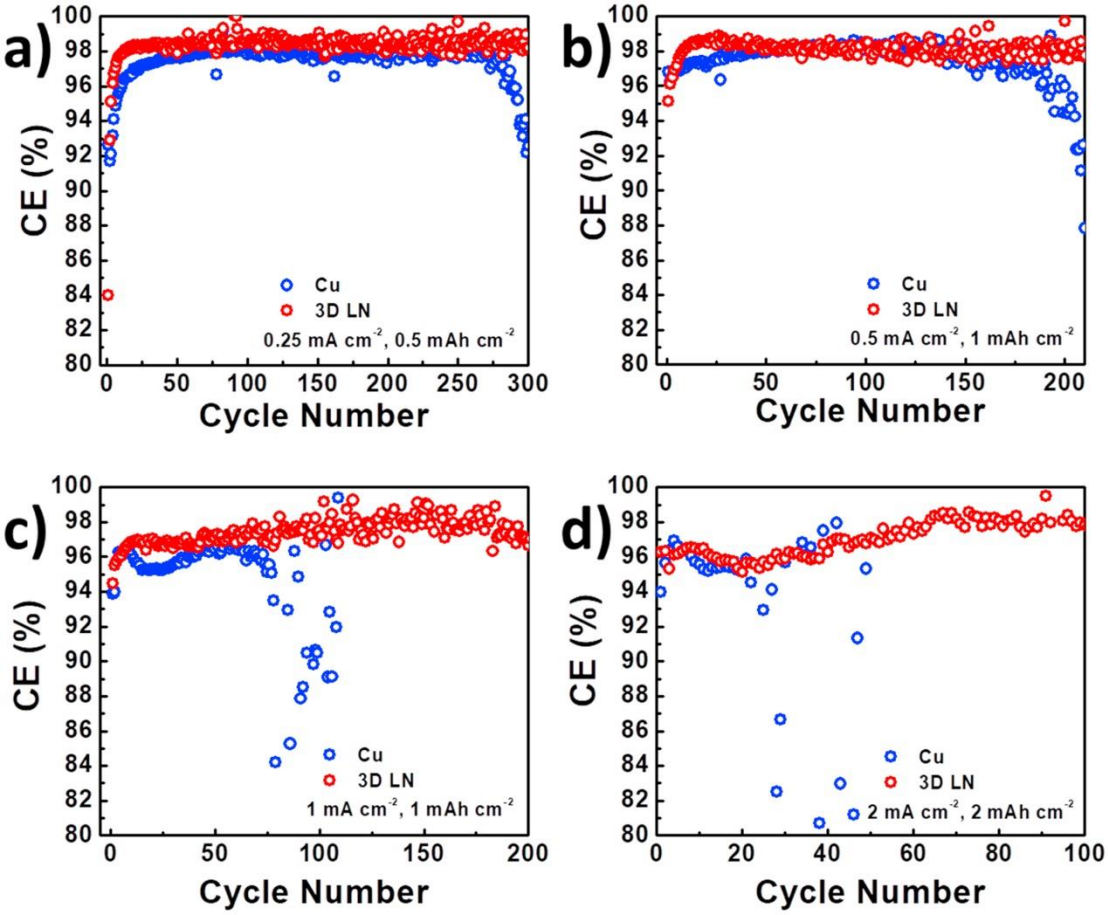

Figure 3-3 The coulombic efficiency comparison of Li||Cu and Li||3D electrode cells cycled in 1 M $LiPF_6$ + 0.02 M $LiNO_3$-EC/DMC electrolyte with 5 wt% VC, (a) at 0.25 mA cm^{-2} for 0.5 mAh cm^{-2}; (b) at 0.5 mA cm^{-2} for 1 mAh cm^{-2}; (c) at 1 mA cm^{-2} for 1 mAh cm^{-2}; (d) at 2 mA cm^{-2} for 2 mAh cm^{-2}.

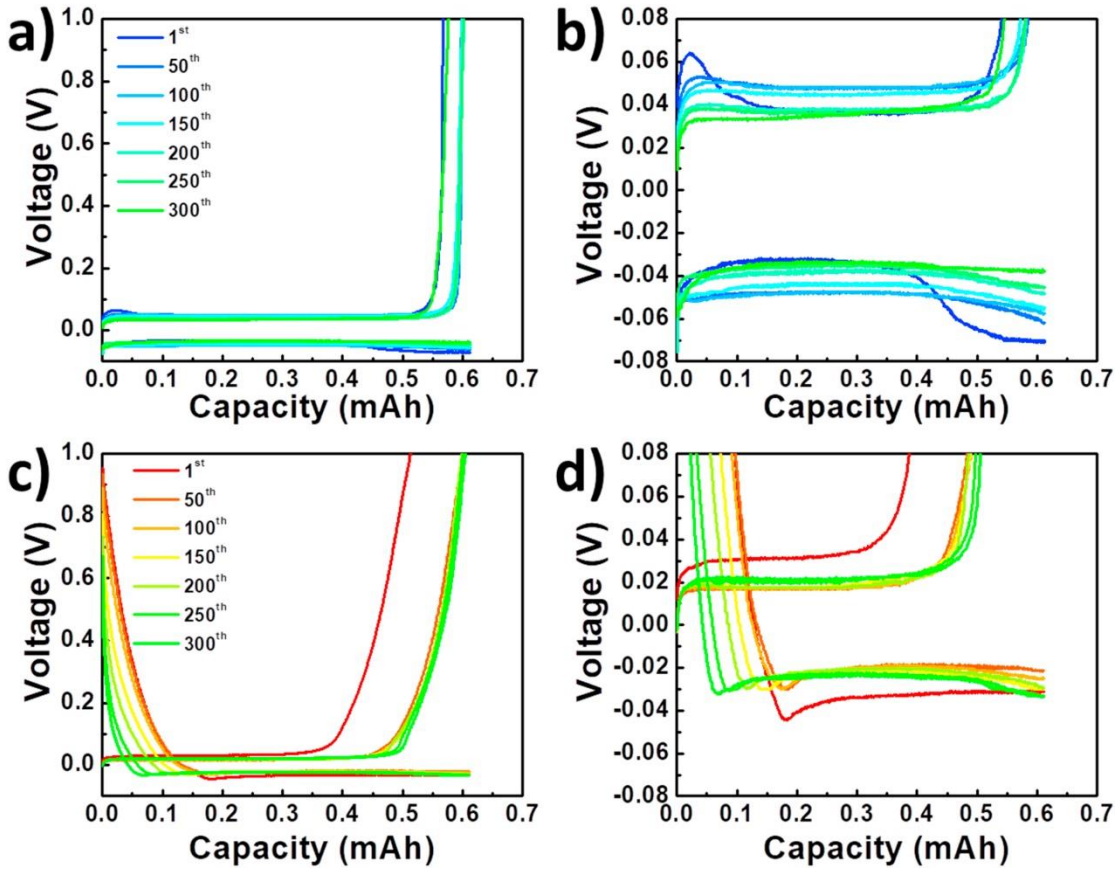

Figure 3-4 (a), and (b) the Li plating/stripping voltage profiles on Cu, at 0.25 mA cm^{-2} for 0.5 mAh cm^{-2}; (c), and (d) the Li plating/stripping voltage profiles on 3D $LiNO_3$ composite electrode, at 0.25 mA cm^{-2} for 0.5 mAh cm^{-2}.

The enhanced CEs were associated with the morphology of the deposited Li. Figure 3-5 and Figure 3-13 illustrated the Li morphology on the 3D substrate. The first deposition of 2 mAh cm^{-2} Li at 2 mA cm^{-2} showed big chunks of Li similar to the bare Cu substrate. Because the porosity of the 17.9 µm thick 3D host was 66.2%, the pores were able to store 11.8 µm of Li metal. Most of the Li was plated into the 3D host, which filled up all the pores inside the host. As a consequence, the thickness of the Li film was 18.2 µm, which was only 1.7% larger than the original 3D host. Both bare Cu substrate

and 3D composite substrates showed dense Li chunks at the first deposition. However, the cells showed different performances after a few Li plating and stripping cycles at 2 mA cm^{-2} for 2 mAh cm^{-2}. Figure 3-5 (b), and e displayed the SEM images of the 20th deposition of the Li on the Cu substrate. All the Li chunks transformed to needles after only 20 cycles, and the thickness of the Li dramatically grew to 68 μm. The short life time of the Li-Cu cell in E3 was caused by the Li dendrite formation as a result of possible $LiNO_3$ depletion. Meanwhile, the morphology of the Li on the 3D composite substrate at its 70th deposition is shown in Figure 3-5 (c), and f. The Li chunk morphology was not only well maintained, but also grew larger. Considering the fact that the CE of the 3D host at 2 mA cm^{-2} was less than 100%, there were accumulations of irreversible Li over 70 cycles. Theoretically, if all the deposited Li were 100% dense, the irreversible Li deposition contributed to 23.1 μm increase of the thickness. In reality, the thickness of the Li film increased to 45 μm, which is only 8.9% higher than assuming completely dense depositions (18.2 + 23.1 μm). The investigation on the evolutions of Li morphologies on different substrates verified that the 3D host maintained the dense Li chunks after long term cycling even at high current density.

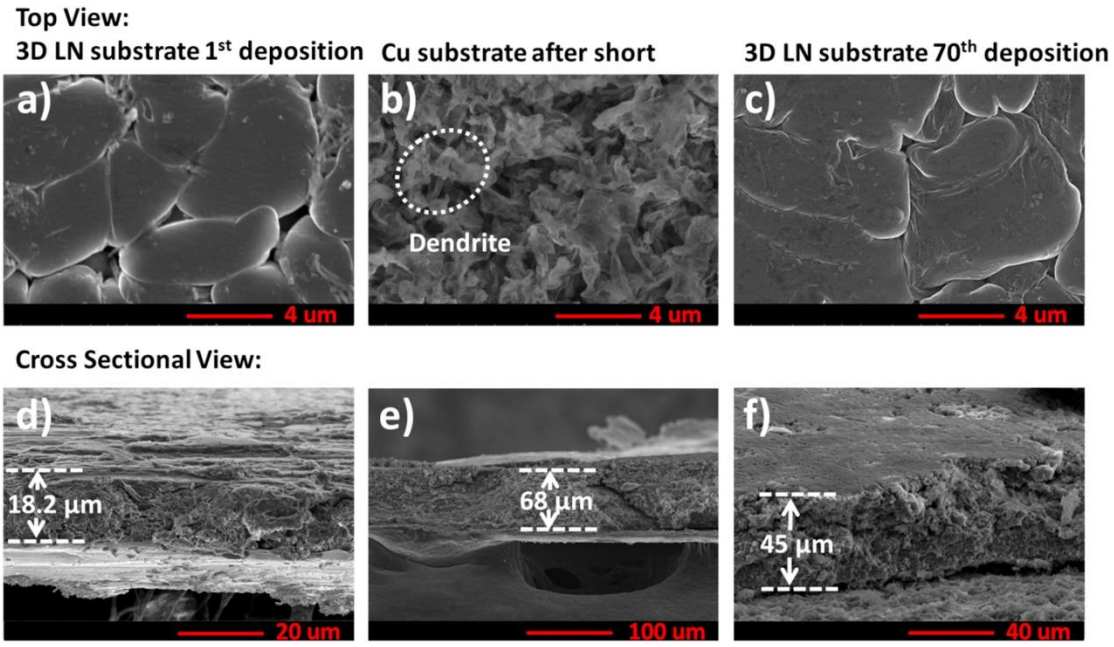

Figure 3-5 SEM images of the deposited Li metal film in 1 M $LiPF_6$ + 0.02 M $LiNO_3$-EC/DMC electrolyte with 5 wt% VC. (a) is the top view and (d) is the cross section view of 3D $LiNO_3$ composite electrode after 1 hour Li deposition at 2 mA cm^{-2}; (b) is the top view and (e) is the cross section view of Cu on its 20th deposition; (c) is the top view and (f) is the cross section view of 3D $LiNO_3$ composite electrode on its 70th deposition; Li depositing at 2 mA cm^{-2} for 2 mAh cm^{-2}, then stripping to 1 V at 2 mA cm^{-2}.

3.4 Anode free full cell performances

Anode free cells with $LiFePO_4$ cathode were fabricated to further evaluate the effectiveness of the 3D host. The area capacity loading of the $LiFePO_4$ was 1.5 mAh cm^{-2}. Figure 3-6 compared the performance of the cells with Cu and 3D host as anode. The cells were cycled between 2.0-4.0 V at 0.5 mA cm^{-2}. The 3D host cell showed much higher CEs and better capacity retention than the Cu cell. The Cu cell exhibited an average CE of 97.3% over the course of 50 cycles, which led to a low capacity retention of 25.6% at the 50th cycle. The 3D host cell maintained 49.1% capacity at its 100th cycle

with a high average CE of 99.3%. Since an anode free cell does not contain excess lithium, the average CE of the cell was calculated as the nth root of X, where the n is the cycle number and the X is the capacity retention at the nth cycle. Note this efficiency is higher than the average CE of a Li metal cell where Li is only partially cycled. In that case, a fixed amount of Li is cycled during each cycle and CE is averaged over multiple cycles. As far as its performance in Li metal anode batteries with high voltage cathodes, for example, classical layered oxides,[23-24] Li-rich layered oxides,[25-26] and high voltage spinel,[27] we do plan to report the test in our future works as we continue to improve the cycling efficiency.

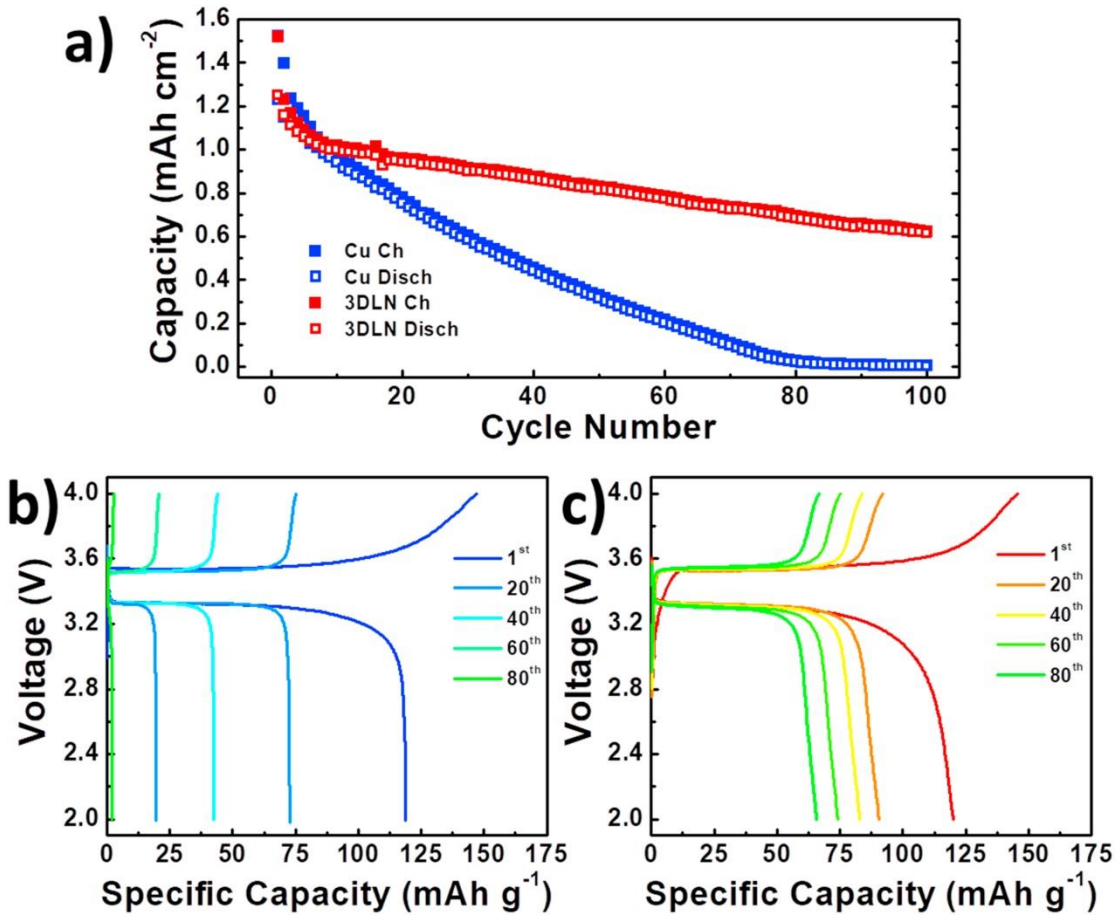

Figure 3-6 The comparison of anode free full cell performance with $LiFePO_4$ (LFP) as cathode in 1 M $LiPF_6$ + 0.02 M $LiNO_3$-EC/DMC electrolyte with 5 wt% VC. (a) is the comparison of capacities and coulombic efficiencies between Cu and 3D $LiNO_3$ composite electrode over the course of 100 cycles; (b), and (c) are the voltage profiles of Cu-LFP and 3D $LiNO_3$ composite electrode-LFP cells, respectively. The voltage range is 2.0-4.0 V at 0.5 mA cm^{-2}.

The importance for both the 3D host structure and abundant $LiNO_3$ reserve is further illustrated with two control experiments. 3D host electrodes without $LiNO_3$ were prepared and compared with the bare Cu and 3D $LiNO_3$ host. The CEs were tested at $0.5\ mA\ cm^{-2}$ for $1\ mAh\ cm^{-2}$. The results in Figure 3-14 revealed that the 3D porous electrode with only carbon and PVDF could not lead to the superior performance without $LiNO_3$. On the other hand, benefiting from the VC and $LiNO_3$ SEI formation additives, the initial Li deposition on bare Cu was dense and full of chunks. However, due to the low solubility of $LiNO_3$ in the carbonates, it was consumed to passivate the freshly deposited Li surfaces during repeated stripping and plating of Li metal. Once the $LiNO_3$ in the electrolyte was consumed, the dendritic Li started to form. As a comparison, the 3D composite host not only works as a conductive host to mitigate the volume expansion, but also supplies the $LiNO_3$ additive to the electrolyte. In order to prove that the reserved $LiNO_3$ was still maintained inside the 3D host after long term cycling, XRD measurements were performed on both cycled bare Cu and 3D $LiNO_3$ composite host. Figure 3-7 (a) clearly demonstrated the diffraction peaks of $LiNO_3$ on the 3D $LiNO_3$ composite host even after 70 cycles. A small diffraction peak related to the Li metal was also observed. In contrast to the 3D host electrode, the bare Cu electrode only presented signals from Li metal. XPS characterizations were also conducted on both cycled bare Cu and 3D $LiNO_3$ composite host. Figure 3-15 compared the C 1s, O 1s, and N 1s spectra of both electrodes. The C 1s and O 1s spectra revealed that the surface of the 3D $LiNO_3$

composite electrode formed more Li_2CO_3 and less Li-alkyl carbonate than the bare Cu. The comparison of the N 1s spectra between both electrodes showed that the $LiNO_3$ reduction compounds Li_3N and LiN_xO_y were formed as SEI components on the surface of the deposited Li film.[28] Moreover, the Li_3N and LiN_xO_y signal on the surface of 3D $LiNO_3$ composite electrode was more prominent, which suggested the 3D $LiNO_3$ composite electrode supplied the $LiNO_3$ additive to the electrolyte. In addition, the $LiNO_3$ peak at 407.4 eV clearly showed the existence of $LiNO_3$ in the 3D composite host after 70 cycles, which is consistent with observations from XRD and SEM. Figure 3-1 (c) illustrated that the $LiNO_3$ particles was well retained inside the host after long term cycling. Consequently, big Li chunk morphology with compact depositions was maintained, which led to the high CE.

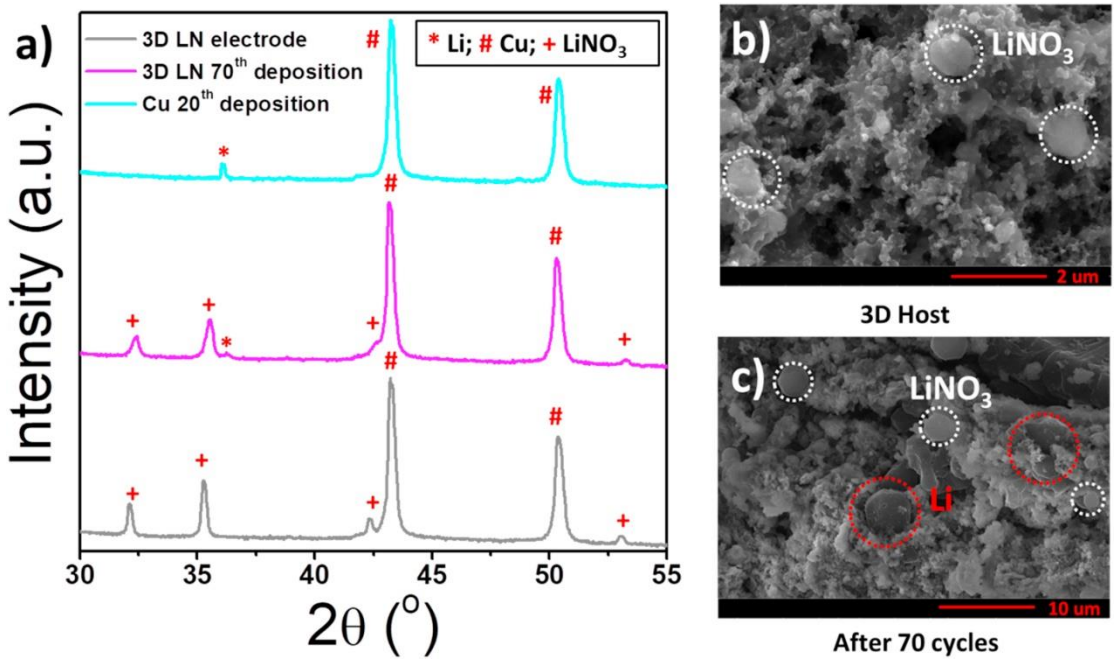

Figure 3-7 (a) XRD patterns. (b) - (c) SEM images. (b) 3D $LiNO_3$ composite host; (c) is the cross sectional view of 3D $LiNO_3$ composite electrode on its 70th deposition, Li depositing at 2 mA cm^{-2} for 2 mAh cm^{-2}, then stripping to 1 V at 2 mA cm^{-2}.

Figure 3-8 (a) illustrates the working mechanism of the 3D composite host. The carbon black in the host provides an electronic conductive network to reduce the local current density and serve as a substrate for Li deposition. The $LiNO_3$ serves as both reserved additive source and a structural skeleton component. The PVDF binder holds all the components together to form the robust porous structure.

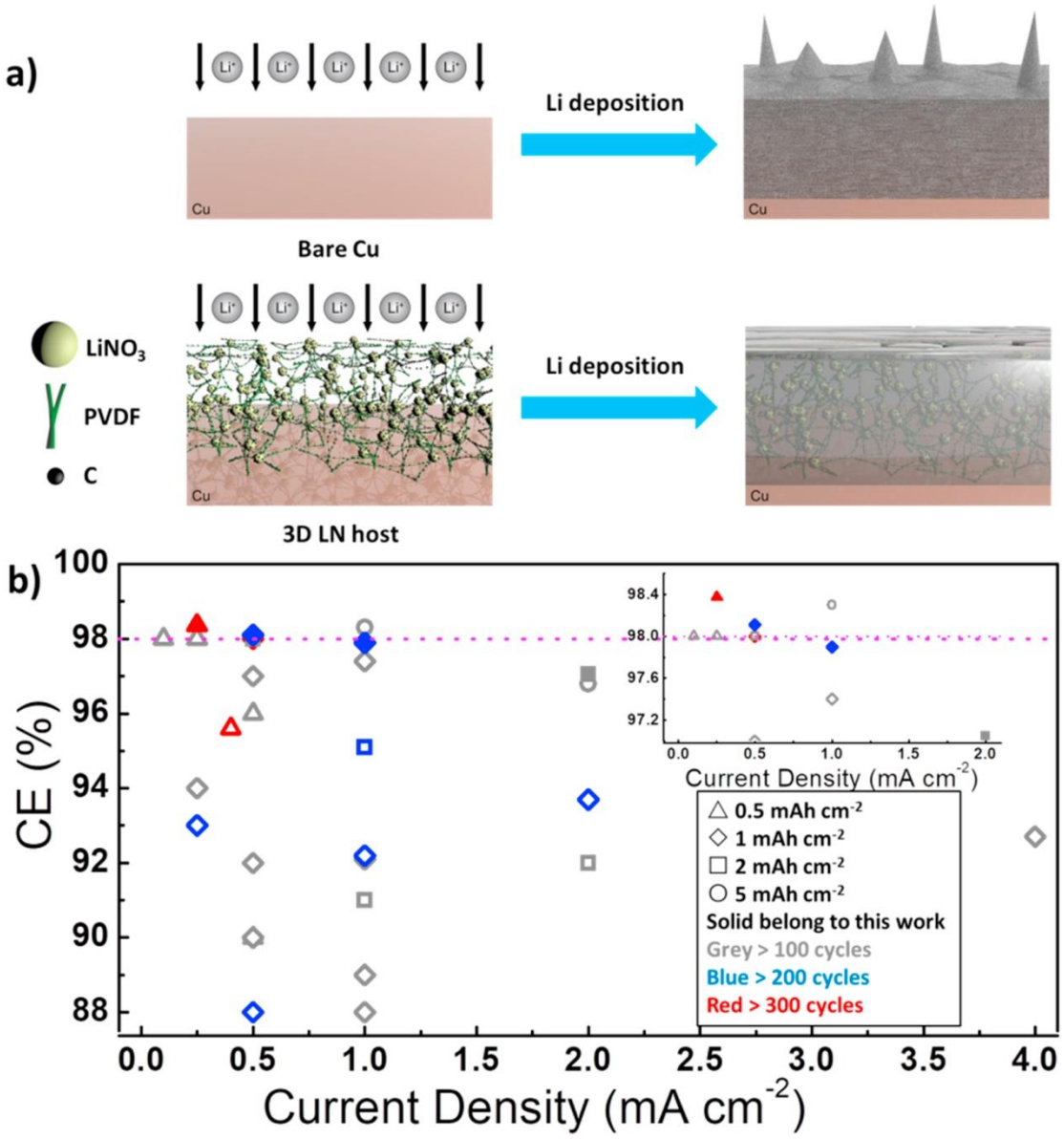

Figure 3-8 (a) The schematic illustration of Li plating/stripping on 3D $LiNO_3$ composite host; (b) a summary of the Li metal anode coulombic efficiencies in carbonate based electrolytes.

To put our results in the context of recently published work, a summary of the Li metal anode coulombic efficiencies in carbonate-based electrolytes was plotted and compared in Figure 3-8 (b) and Table 3-1. The CE tests in most of the published literature

are conducted at current densities of less than 1 mA cm^{-2} and the Li deposition capacities are lower than 1 mAh cm^{-2}. The CEs of Li in the carbonate electrolytes are usually less than 96%. The solid symbols represent the CEs that are achieved in this work. A high CE of 98.4% is reached at a moderate current density of 0.25 mA cm^{-2}. At a high current density of 2 mA cm^{-2}, the CE remains above 97%.

3.5 Conclusion

In summary, a novel multi-functional 3D composite host is designed for Li metal anode. Due to the robust structure and abundant supplement of the $LiNO_3$, dense Li chunks instead of dendrites are formed and retained after repeated Li plating and stripping at a current density of 2 mA cm^{-2}. As a result, the coulombic efficiencies of Li metal on the 3D composite host are reasonably high in the carbonate electrolyte. A high coulombic efficiency of 98.4% has been achieved at 0.25 mA cm^{-2} for a long cycling duration of more than 1200 h. The fabrication process of the 3D host can be easily scaled up by battery manufacturers. This work provides a new route of designing low-cost 3D Li metal for high energy density safe batteries.

3.6 Experimental

3D composite electrode preparation: The 3D composite electrode was prepared by mixing the $LiNO_3$ (Sigma-Aldrich), with 20 wt % Super P carbon (TIMCAL) and 20 wt % poly(vinylidene fluoride) (PVDF) in N-methylpyrrolidone (NMP, ACROS Organics). The slurry was cast onto a Cu foil using a doctor blade and dried in a vacuum oven overnight at 80 °C. The electrode discs were punched and dried again before being storing in an argon-filled glovebox (MTI corporation).

Electrochemical test: Battery grade vinylene carbonate (VC) was acquired from Shenzhen CAPCHEM Technology Co. Ltd. The premixed LP30 electrolyte (1 M $LiPF_6$ in 1:1 vol ratio EC/DMC) was purchased from BASF.

2032-type coin cells were used for all the electrochemical studies in this work. The 250 μm thick lithium was punched to 12.5 mm discs as the counter electrode. The Celgard 25 μm trilayer PP-PE-PP membrane was used as a separator. Galvanostatic cycling was conducted on an LBT-5V5A battery tester (Arbin instruments). The cycled electrode was recovered by disassembling the coin cell. All the samples were washed with DMC three times and dried in the glovebox antechamber under vacuum.

Scanning electron microscopy: The morphology and thickness of the deposited Li metal film and 3D composite electrode were characterized using scanning electron microscopy (FEI Quanta 250 SEM). The sample was adhered to a double-sided carbon tape and placed on a specimen holder. The prepared sample was sealed in a laminate

plastic bag inside the glovebox for transferring to the SEM. The approximate time of sample exposed to air (from a sealed environment to the SEM stage) was less than 3 s.

X-ray diffraction: The crystal structure of coating materials were identified by X-ray diffraction (XRD), acquired using a Bruker D2 phaser diffractometer with a Bragg-Brentano θ-2θ geometry and a Cu Kα source (λ = 1.54 Å). Samples were sealed inside the glovebox by kapton tape, which were scanned from 30° to 60° at a scan rate of 0.02° s^{-1}.

X-ray photoelectron spectroscopy: XPS (Kratos Analytical, Kratos AXIS Supra) was carried out using Al anode source at 15 kV was used and all the peaks were fitted based on the reference C-C bond at 284.6 eV. All XPS measurements were collected with a 300 mm × 700 mm spot size using a charge neutralizer during acquisition. Survey scans were collected with a 1.0 eV step size, and were followed by high resolution scans with a step size of 0.05 eV for C 1s, O 1s, and N 1s regions.

3.7 Appendix

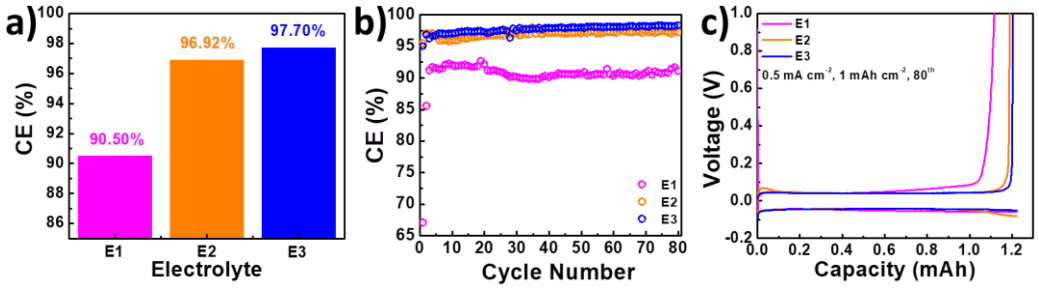

Figure 3-9 The comparison of Li metal coulombic efficiencies in 1 M $LiPF_6$-EC/DMC electrolyte, 1 M $LiPF_6$-EC/DMC electrolyte with 5 wt% VC, and 1 M $LiPF_6$ + 0.02 M $LiNO_3$-EC/DMC electrolyte with 5 wt% VC, (a) average CE over 80 cycles, (b) CEs over the course of 80 cycles. (c) comparison of the 80th plating/stripping voltage profiles in various electrolytes. Li depositing at 0.5 mA cm^{-2} for 1 mAh cm^{-2}, then stripping to 1V at 0.5 mA cm^{-2}.

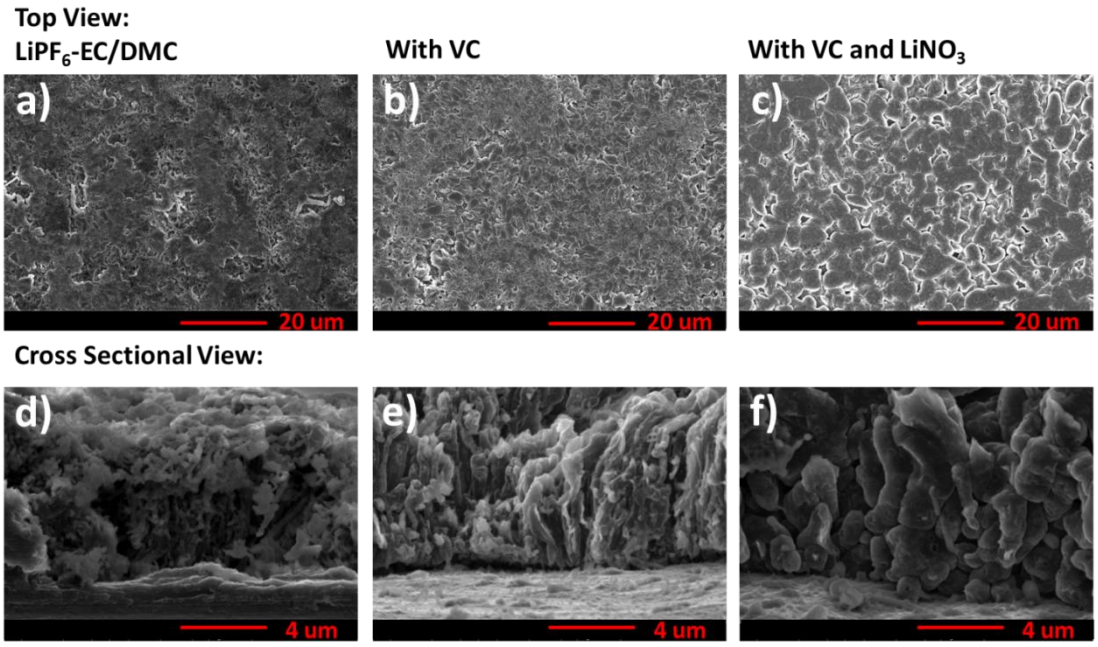

Figure 3-10 SEM images of the deposited Li metal film on Cu foil. (a), (b), (c) are the top view and (d), (e), (f) are the cross section view of Cu after 1 hours Li deposition at 2 mA cm^{-2} in 1 M $LiPF_6$-EC/DMC electrolyte, 1 M $LiPF_6$-EC/DMC electrolyte with 5 wt% VC, and 1 M $LiPF_6$ + 0.02 M $LiNO_3$-EC/DMC electrolyte with 5 wt% VC, respectively.

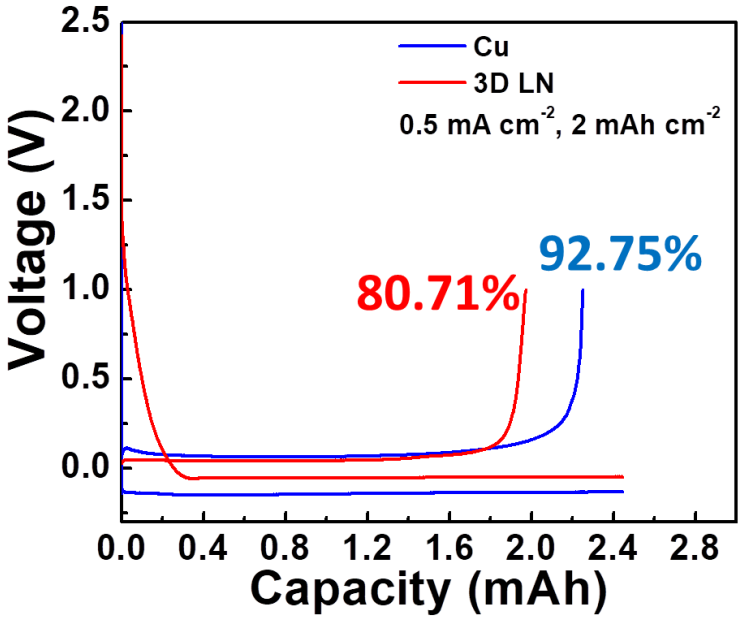

Figure 3-11 The comparison of Li plating/stripping voltage profiles between Cu and 3D $LiNO_3$ composite electrode in their condition cycles. Li depositing at 0.5 mA cm^{-2} for 2 mAh cm^{-2}, then stripping to 1V at 0.5 mA cm^{-2}.

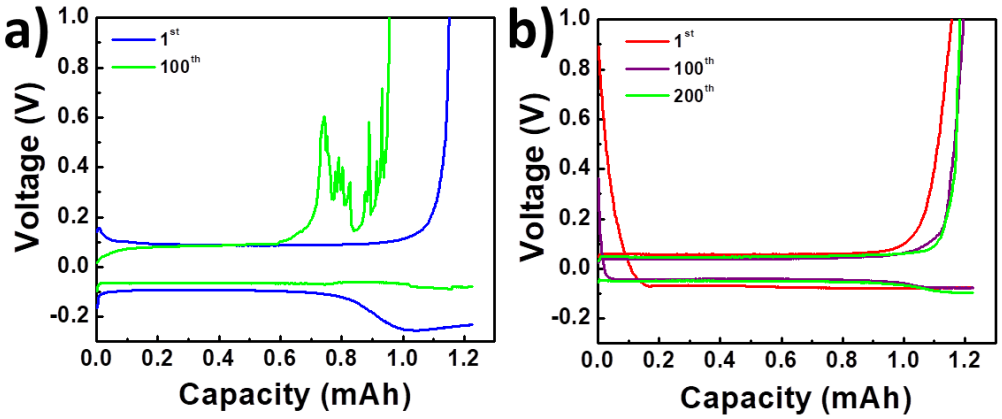

Figure 3-12 (a) the Li plating/stripping voltage profiles on Cu, at 1 mA cm^{-2} for 1 mAh cm^{-2}; (b) the Li plating/stripping voltage profiles on 3D $LiNO_3$ composite electrode, at 1 mA cm^{-2} for 1 mAh cm^{-2}.

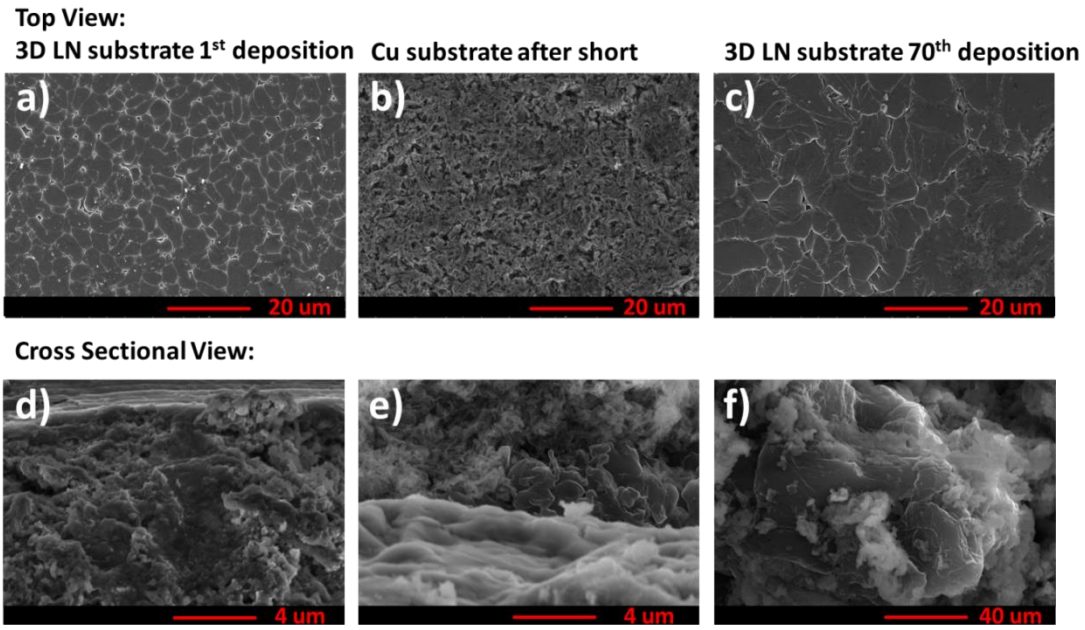

Figure 3-13 SEM images of the deposited Li metal film in 1 M $LiPF_6$ + 0.02 M $LiNO_3$-EC/DMC electrolyte with 5 wt% VC. (a) is the top view and (d) is the cross section view of 3D $LiNO_3$ composite electrode after 1 hour Li deposition at 2 mA cm^{-2}; (b) is the top view and (e) is the cross section view of Cu on its 20th deposition; (c) is the top view and (f) is the cross section view of 3D $LiNO_3$ composite electrode on its 70th deposition; Li depositing at 2 mA cm^{-2} for 2 mAh cm^{-2}, then stripping to 1V at 2 mA cm^{-2}.

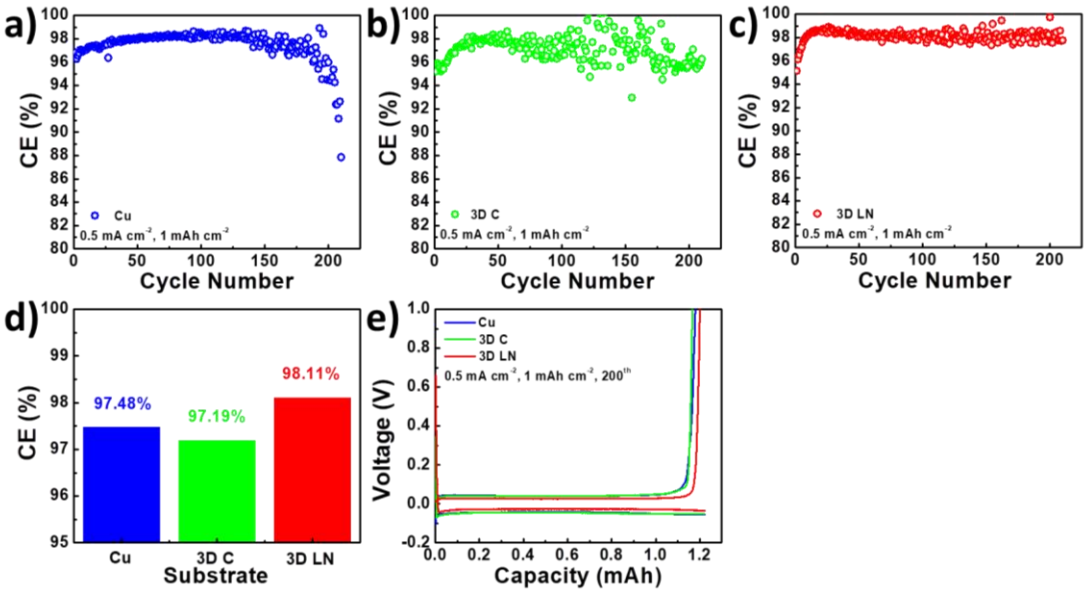

Figure 3-14 The comparison of Li metal coulombic efficiencies in 1 M $LiPF_6$ + 0.02 M $LiNO_3$-EC/DMC electrolyte with 5 wt% VC, (a) Cu substrate, (b) 3D carbon electrode, (c) 3D $LiNO_3$ composite electrode, (d) average CEs, (e) comparison of the 200th plating/stripping voltage profiles on different substrates. Li depositing at 0.5 mA cm^{-2} for 1 mAh cm^{-2}, then stripping to 1V at 0.5 mA cm^{-2}.

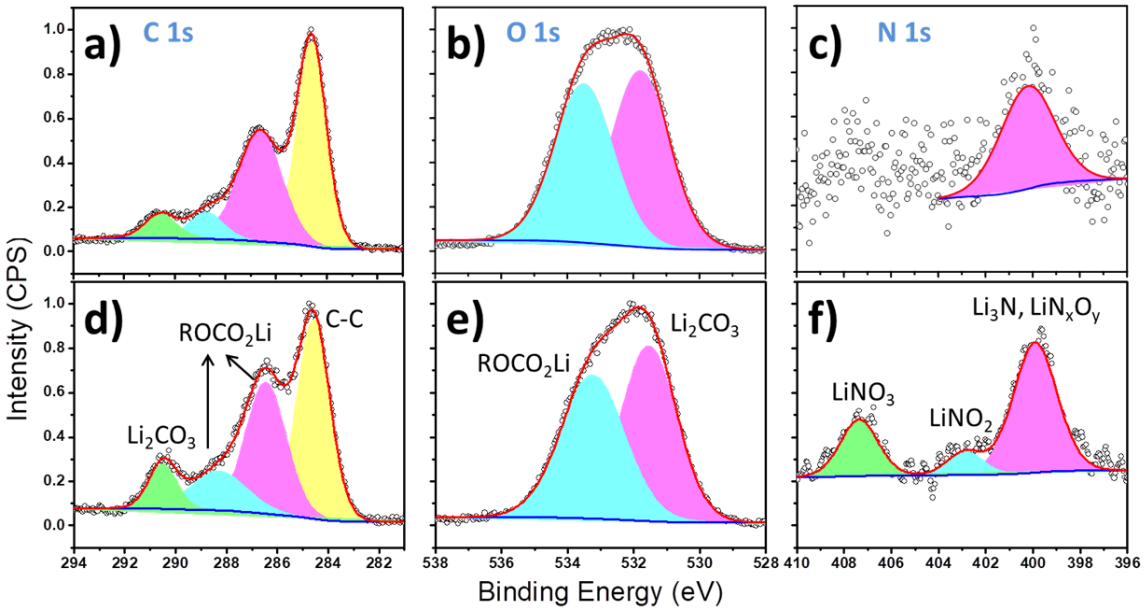

Figure 3-15 XPS spectra of the deposited Li metal film in 1 M $LiPF_6$ + 0.02 M $LiNO_3$-EC/DMC electrolyte with 5 wt% VC. (a), (b), and (c) are the C 1s, O 1s, and N 1s regions of Cu on its 20th deposition; (d), (e), and (f) are the C 1s, O 1s, and N 1s regions of 3D $LiNO_3$ composite electrode on its 70th deposition; Li depositing at 2 mA cm^{-2} for 2 mAh cm^{-2}, then stripping to 1V at 2 mA cm^{-2}.

Table 3-1 A summary of the Li metal coulombic efficiencies in carbonate electrolyte.

Reference	Electrolyte	Current (mA cm^{-2})	Capacity (mAh cm^{-2})	Cycle #	CE
28	1 M $LiPF_6$-EC/DEC (1:1 vol.)	1	1	242	92.20%
		2	1	240	93.70%
		4	1	120	92.70%
		1	2	217	95.10%
		1	5	160	98.30%
		2	5	100	96.80%
29	1 M $LiPF_6$-EC/DEC (1:1 vol.) + 5 vol% FEC	0.1	0.5	100	98%
		0.5	0.5	100	90%*
30	1 M $LiPF_6$-EC/DEC (1:1 vol.) + 10 wt% FEC	1	1	100	97.40%
		0.25	0.5	150	98%
31	1 M $LiPF_6$-EC/DMC/EMC (1:1:1 vol.)	1	1	100	89%
32	1 M $LiPF_6$-EC/DEC (1:1 vol.)	0.25	1	100	94%
		0.5	1	100	92%
		1	1	100	88%
33	1 M $LiPF_6$-EC/DMC/DEC (1:1:1 vol.) with $AlCl_3$ additive	0.5	2	150	98%
34	1 M $LiPF_6$-EC/DEC (1:1 vol.) + 2 wt% VC	0.25	1	200	93%
		0.5	1	100	90%
		1	1	100	89%
35	1 M $LiPF_6$-EC/DEC (1:1 vol.) + 10% FEC + 1 % VC	0.5	1	300	98%
36	1 M $LiPF_6$-EC/DEC (1:1 vol.)	2	2	100	92%
37	1 M $LiPF_6$-EC/EMC/FEC (3:7:1 vol.)	0.5	1	200	98%

Table 3-1 A summary of the Li metal coulombic efficiencies in carbonate electrolyte (Continued).

Reference	Electrolyte	Current (mA cm^{-2})	Capacity (mAh cm^{-2})	Cycle #	CE
38	1 M $LiPF_6$-EC/EMC/DEC + 3% FEC	0.5	1	300	98%
39	1 M $LiPF_6$-EC/DMC (1:1 vol.) + $Mg(TFSI)_2$	0.5	1	240	88%
		1	2	130	91%
40	1 M $LiPF_6$-EC/DEC (1:1 vol.) + 10wt% FEC + 1 wt% VC	0.4	0.5	300	95.60%
		1	1	100	92.10%
41	1 M $LiPF_6$-EC/DEC (1:1 vol.) + 5 vol% FEC	0.5	1	350	98%
42	1 M $LiPF_6$-EC/DMC + 2 vol% FEC	0.5	1	150	97%
This work	1 M $LiPF_6$-EC/DMC + 2 wt% VC + 0.02 M $LiNO_3$	0.25	0.5	300	98.37%
		0.5	1	210	98.11%
		1	1	200	97.90%
		2	2	100	97.05%

3.8 Acknowledgments

Text, tables, and figures in this chapter, in full, are reprints of materials published in the following paper: Haodong Liu, Xiujun Yue, Xing Xing, Qizhang Yan, Jason Huang, Victoria Petrova, Hongyao Zhou and Ping Liu*, "A scalable 3D lithium metal anode" *Energy Storage Materials*, **2019**, 16, 505-511. The dissertation author was one of the primary researchers for the data presented and was one of the primary authors of this

publication. The permissions to reproduce this material were granted by the Elsevier B.V., copyright 2018.

3.9 References

1. Xu, W.; Wang, J.; Ding, F.; Chen, X.; Nasybulin, E.; Zhang, Y.; Zhang, J.-G. Lithium metal anodes for rechargeable batteries. *Energy Environ. Sci.,* **2014,** *7*, 513-537.

2. Lin, D.; Liu, Y.; Cui, Y. Reviving the lithium metal anode for high-energy batteries. *Nat. Nanotechnol.*, **2017,** *12*, 194.

3. Cheng, X.-B.; Zhang, R.; Zhao, C.-Z.; Zhang, Q. Toward Safe Lithium Metal Anode in Rechargeable Batteries: A Review. *Chem. Rev.,* **2017,** *117*, 10403-10473.

4. Tikekar, M. D.; Choudhury, S.; Tu, Z.; Archer, L. A. Design principles for electrolytes and interfaces for stable lithium-metal batteries. *Nat. Energy,* **2016,** *1*, 16114.

5. Aurbach, D.; Zinigrad, E.; Cohen, Y.; Teller, H. A short review of failure mechanisms of lithium metal and lithiated graphite anodes in liquid electrolyte solutions. *Solid State Ionics,* **2002,** *148*, 405-416.

6. Liu, H.; Wang, X.; Zhou, H.; Lim, H.-D.; Xing, X.; Yan, Q.; Meng, Y. S.; Liu, P. Structure and Solution Dynamics of Lithium Methyl Carbonate as a Protective Layer For Lithium Metal. *ACS Appl. Energy Mater.*, **2018,** *1*, 1864-1869.

7. Liu, H.; Zhou, H.; Lee, B.-S.; Xing, X.; Gonzalez, M.; Liu, P. Suppressing Lithium Dendrite Growth with a Single-Component Coating. *ACS Appl. Mater. Interfaces,* **2017,** *9*, 30635-30642.

8. Liu, L.; Yin, Y.-X.; Li, J.-Y.; Wang, S.-H.; Guo, Y.-G.; Wan, L.-J. Uniform Lithium Nucleation/Growth Induced by Lightweight Nitrogen-Doped Graphitic Carbon Foams for High-Performance Lithium Metal Anodes. *Adv. Mater.,* **2018,** *30*, 1706216.

9. Fan, X.; Chen, L.; Ji, X.; Deng, T.; Hou, S.; Chen, J.; Zheng, J.; Wang, F.; Jiang, J.; Xu, K.; Wang, C. Highly Fluorinated Interphases Enable High-Voltage Li-Metal Batteries. *Chem,* **2018,** *4*, 174-185.

10. Lim, H.-D.; Lim, H.-K.; Xing, X.; Lee, B.-S.; Liu, H.; Coaty, C.; Kim, H.; Liu, P. Solid Electrolyte Layers by Solution Deposition. *Adv. Mater. Interfaces,* **2018,** *5*, 1701328.

11. Li, N.-W.; Shi, Y.; Yin, Y.-X.; Zeng, X.-X.; Li, J.-Y.; Li, C.-J.; Wan, L.-J.; Wen, R.; Guo, Y.-G. A Flexible Solid Electrolyte Interphase Layer for Long-Life Lithium Metal Anodes. *Angew. Chem. Int. Ed.,* **2018,** *57*, 1505-1509.

12. Lim, H.-D.; Yue, X.; Xing, X.; Petrova, V.; Gonzalez, M.; Liu, H.; Liu, P. Designing solution chemistries for the low-temperature synthesis of sulfide-based solid electrolytes. *J. Mater. Chem. A,* **2018,** *6*, 7370-7374.

13. Xu, K. Electrolytes and Interphases in Li-Ion Batteries and Beyond. *Chem. Rev.,* **2014,** *114*, 11503-11618.

14. Radin, M. D.; Hy, S.; Sina, M.; Fang, C.; Liu, H.; Vinckeviciute, J.; Zhang, M.; Whittingham, M. S.; Meng, Y. S.; Van der Ven, A. Narrowing the Gap between Theoretical and Practical Capacities in Li-Ion Layered Oxide Cathode Materials. *Adv. Energy Mater.,* **2017,** *7*, 1602888.

15. Hy, S.; Liu, H.; Zhang, M.; Qian, D.; Hwang, B.-J.; Meng, Y. S. Performance and design considerations for lithium excess layered oxide positive electrode materials for lithium ion batteries. *Energy Environ. Sci.,* **2016,** *9*, 1931-1954.

16. Ren, X.; Zhang, Y.; Engelhard, M. H.; Li, Q.; Zhang, J.-G.; Xu, W. Guided Lithium Metal Deposition and Improved Lithium Coulombic Efficiency through Synergistic Effects of LiAsF6 and Cyclic Carbonate Additives. *ACS Energy Lett.,* **2018,** *3*, 14-19.

17. Ke, X.; Cheng, Y.; Liu, J.; Liu, L.; Wang, N.; Liu, J.; Zhi, C.; Shi, Z.; Guo, Z. Hierarchically Bicontinuous Porous Copper as Advanced 3D Skeleton for Stable Lithium Storage. *ACS Appl. Mater. Interfaces,* **2018,** *10*, 13552-13561.

18. Lin, D.; Liu, Y.; Liang, Z.; Lee, H.-W.; Sun, J.; Wang, H.; Yan, K.; Xie, J.; Cui, Y. Layered reduced graphene oxide with nanoscale interlayer gaps as a stable host for lithium metal anodes. *Nat. Nanotechnol.,* **2016,** *11*, 626.

19. Yang, C.-P.; Yin, Y.-X.; Zhang, S.-F.; Li, N.-W.; Guo, Y.-G. Accommodating lithium into 3D current collectors with a submicron skeleton towards long-life lithium metal anodes. *Nat. Commun.,* **2015,** *6*, 8058.

20. Li, W.; Yao, H.; Yan, K.; Zheng, G.; Liang, Z.; Chiang, Y.-M.; Cui, Y. The synergetic effect of lithium polysulfide and lithium nitrate to prevent lithium dendrite growth. *Nat. Commun.,* **2015,** *6*, 7436.

21. Adams, B. D.; Carino, E. V.; Connell, J. G.; Han, K. S.; Cao, R.; Chen, J.; Zheng, J.; Li, Q.; Mueller, K. T.; Henderson, W. A.; Zhang, J.-G. Long term stability of Li-S batteries using high concentration lithium nitrate electrolytes. *Nano Energy,* **2017,** *40*, 607-617.

22. Lee, B.-S.; Wu, Z.; Petrova, V.; Xing, X.; Lim, H.-D.; Liu, H.; Liu, P. Analysis of Rate-Limiting Factors in Thick Electrodes for Electric Vehicle Applications. *J. Electrochem. Soc.*, **2018,** *165*, A525-A533.

23. Liu, H.; Liu, H.; Lapidus, S. H.; Meng, Y. S.; Chupas, P. J.; Chapman, K. W. Sensitivity and Limitations of Structures from X-ray and Neutron-Based Diffraction Analyses of Transition Metal Oxide Lithium-Battery Electrodes. *J. Electrochem. Soc.*, **2017,** *164*, A1802-A1811.

24. Liu, H.; Liu, H.; Seymour, I. D.; Chernova, N.; Wiaderek, K. M.; Trease, N. M.; Hy, S.; Chen, Y.; An, K.; Zhang, M.; Borkiewicz, O. J.; Lapidus, S. H.; Qiu, B.; Xia, Y.; Liu, Z.; Chupas, P. J.; Chapman, K. W.; Whittingham, M. S.; Grey, C. P.; Meng, Y. S. Identifying the chemical and structural irreversibility in $LiNi_{0.8}Co_{0.15}Al_{0.05}O_2$ – a model compound for classical layered intercalation. *J. Mater. Chem. A,* **2018,** *6*, 4189-4198.

25. Liu, H.; Qian, D.; Verde, M. G.; Zhang, M.; Baggetto, L.; An, K.; Chen, Y.; Carroll, K. J.; Lau, D.; Chi, M.; Veith, G. M.; Meng, Y. S. Understanding the Role of NH_4F and Al_2O_3 Surface Co-modification on Lithium-Excess Layered Oxide $Li_{1.2}Ni_{0.2}Mn_{0.6}O_2$. *ACS Appl. Mater. Interfaces,* **2015,** *7*, 19189-19200.

26. Liu, H.; Chen, Y.; Hy, S.; An, K.; Venkatachalam, S.; Qian, D.; Zhang, M.; Meng, Y. S. Operando Lithium Dynamics in the Li-Rich Layered Oxide Cathode Material via Neutron Diffraction. *Adv. Energy Mater.*, **2016,** *6*, 1502143.

27. Huang, J.; Liu, H.; Zhou, N.; An, K.; Meng, Y. S.; Luo, J. Enhancing the Ion Transport in $LiMn_{1.5}Ni_{0.5}O_4$ by Altering the Particle Wulff Shape via Anisotropic Surface Segregation. *ACS Appl. Mater. Interfaces,* **2017,** *9*, 36745-36754.

28. Shi, Q.; Zhong, Y.; Wu, M.; Wang, H.; Wang, H. High-capacity rechargeable batteries based on deeply cyclable lithium metal anodes. *PNAS,* **2018,** *115*, 5676-5680.

29. Zhang, X.-Q.; Cheng, X.-B.; Chen, X.; Yan, C.; Zhang, Q. Fluoroethylene Carbonate Additives to Render Uniform Li Deposits in Lithium Metal Batteries. *Adv. Funct. Mater.*, **2017,** *27*, 1605989.

30. Liu, Y.; Lin, D.; Yuen, P. Y.; Liu, K.; Xie, J.; Dauskardt, R. H.; Cui, Y. An Artificial Solid Electrolyte Interphase with High Li-Ion Conductivity, Mechanical Strength, and Flexibility for Stable Lithium Metal Anodes. *Adv. Mater.,* **2017,** *29*, 1605531.

31. Chi, S.-S.; Liu, Y.; Song, W.-L.; Fan, L.-Z.; Zhang, Q. Prestoring Lithium into Stable 3D Nickel Foam Host as Dendrite-Free Lithium Metal Anode. *Adv. Funct. Mater.,* **2017,** *27*, 1700348.

32. Luo, W.; Zhou, L.; Fu, K.; Yang, Z.; Wan, J.; Manno, M.; Yao, Y.; Zhu, H.; Yang, B.;

Hu, L. A Thermally Conductive Separator for Stable Li Metal Anodes. *Nano Lett.,* **2015,** *15*, 6149-6154.

33. Ye, H.; Yin, Y.-X.; Zhang, S.-F.; Shi, Y.; Liu, L.; Zeng, X.-X.; Wen, R.; Guo, Y.-G.; Wan, L.-J. Synergism of Al-containing solid electrolyte interphase layer and Al-based colloidal particles for stable lithium anode. *Nano Energy,* **2017,** *36*, 411-417.

34. Zhu, B.; Jin, Y.; Hu, X.; Zheng, Q.; Zhang, S.; Wang, Q.; Zhu, J. Poly(dimethylsiloxane) Thin Film as a Stable Interfacial Layer for High-Performance Lithium-Metal Battery Anodes. *Adv. Mater.,* **2017,** *29*, 1603755.

35. Yan, K.; Lu, Z.; Lee, H.-W.; Xiong, F.; Hsu, P.-C.; Li, Y.; Zhao, J.; Chu, S.; Cui, Y. Selective deposition and stable encapsulation of lithium through heterogeneous seeded growth. *Nat. Energy,* **2016,** *1*, 16010.

36. Lu, L.-L.; Zhang, Y.; Pan, Z.; Yao, H.-B.; Zhou, F.; Yu, S.-H. Lithiophilic Cu–Ni core–shell nanowire network as a stable host for improving lithium anode performance. *Energy Storage Mater.,* **2017,** *9*, 31-38.

37. Gao, Y.; Zhao, Y.; Li, Y. C.; Huang, Q.; Mallouk, T. E.; Wang, D. Interfacial Chemistry Regulation via a Skin-Grafting Strategy Enables High-Performance Lithium-Metal Batteries. *J. Am. Chem. Soc.,* **2017,** *139*, 15288-15291.

38. Peng, Z.; Zhao, N.; Zhang, Z.; Wan, H.; Lin, H.; Liu, M.; Shen, C.; He, H.; Guo, X.; Zhang, J.-G.; Wang, D. Stabilizing Li/electrolyte interface with a transplantable protective layer based on nanoscale LiF domains. *Nano Energy,* **2017,** *39*, 662-672.

39. Chu, F.; Hu, J.; Tian, J.; Zhou, X.; Li, Z.; Li, C. In Situ Plating of Porous Mg Network Layer to Reinforce Anode Dendrite Suppression in Li-Metal Batteries. *ACS Appl. Mater. Interfaces,* **2018,** *10*, 12678-12689.

40. Lee, H.; Ren, X.; Niu, C.; Yu, L.; Engelhard, M. H.; Cho, I.; Ryou, M.-H.; Jin, H. S.; Kim, H.-T.; Liu, J.; Xu, W.; Zhang, J.-G. Suppressing Lithium Dendrite Growth by Metallic Coating on a Separator. *Adv. Funct. Mater.,* **2017,** *27*, 1704391.

41. Zhang, Z.; Peng, Z.; Zheng, J.; Wang, S.; Liu, Z.; Bi, Y.; Chen, Y.; Wu, G.; Li, H.; Cui, P.; Wen, Z.; Wang, D. The long life-span of a Li-metal anode enabled by a protective layer based on the pyrolyzed N-doped binder network. *J. Mater. Chem. A,* **2017,** *5*, 9339-9349.

42. Zhang, Z.; Xu, X.; Wang, S.; Peng, Z.; Liu, M.; Zhou, J.; Shen, C.; Wang, D. Li2O-Reinforced Cu Nanoclusters as Porous Structure for Dendrite-Free and Long-Lifespan Lithium Metal Anode. *ACS Appl. Mater. Interfaces,* **2016,** *8*, 26801-26808.

Chapter 4: Polymer grafted on carbon nanotubes as a flexible cathode for aqueous zinc ion batteries

4.1 Introduction

Driven by the ever increasing demand of environmentally benign, low-cost electrical energy storage solutions, Zn based aqueous batteries are being extensively investigated due to potential advantages in cost, safety, abundancy, and environmental friendliness.[1-4] With a very negative electrical potential of -0.76 V vs. SHE, zinc based batteries also offer highly competitive energy densities.[5-6]

Finding a reversible cathode with high capacity has been a major challenge. Intercalation reaction based materials, including oxides of manganese and vanadium, are the current focus.[7-12] Due to the large changes in crystal volume, structure, and morphology during zinc insertion and removal, cycling stability of these materials is usually a concern.[3, 13-14] In addition, manganese oxides also suffer severe capacity fading due to Mn^{2+} dissolution associated with the Jahn-Teller effect.[1, 15-16] Adding manganese or other salts into the electrolyte is required to alleviate such effects.[17-18] Framework type (e.g., Prussian blue analogs) materials have also been investigated, which offer enhanced cycling stability at the expense of volumetric energy density.[19-20]

Very recently, several attempts have been made to develop organic cathode materials utilizing an energy storage mechanism other than intercalation/deintercalation. For instance, quinone exhibits ion storage capability by coordinating with the metal ions with its oxygen atoms when the carbonyl groups are reduced at low potentials.[21-25] Both high capacity and cycling stability has been achieved by calix[4]quinone (C4Q) when

used in a zinc ion battery.[26] Moreover, polymers are expected to have minimal dissolution in the electrolyte and long cycle life due to the stable, covalently connected structure.[27]

Herein, we demonstrate the application of polydopamine (PDA)/carbon nanotube (CNT) composite as a cathode material for aqueous zinc ion batteries (Figure 4-1). Inspired by the adhesive protein Mefp5 in mussels, PDA can be coated on a wide range of material surfaces through the spontaneous self-polymerization of dopamine in basic aqueous solution.[28-29] In each building unit, two redox-active quinone groups are available for zinc ion storage via the reversible catechol/ortho-quinone reaction (Figure 4-1 (c)).[30-32] Compared to other organic cathodes for zinc-ion batteries, PDA has several advantages: (1) PDA has low solubility in water which mitigates capacity loss during cycling. Additionally, the hydrophilic nature of PDA ensures excellent wetting at the electrode/electrolyte interface, whereas many other polymer cathodes are hydrophobic;[33] (2) due to the bio-adhesion effect, PDA enhance the structural stability of composite electrode as it adheres to the conductive CNT strongly which results in high rate capability. In comparison, polymer cathodes are usually physically mixed with large amount of carbon, making it difficult to achieve a highly efficient conductive network; (3) with a similar structure and function to natural eumelanins, PDA exhibits high biocompatibility and low cytotoxicity.[34] Indeed, a Zn/PDA battery with an aqueous electrolyte at a neutral pH would be substantially non-hazardous and highly desirable for

biomedical devices; and (4) the PDA/CNT electrode is highly flexible which makes it possible to fabricate conformal batteries, also essential for biomedical applications.

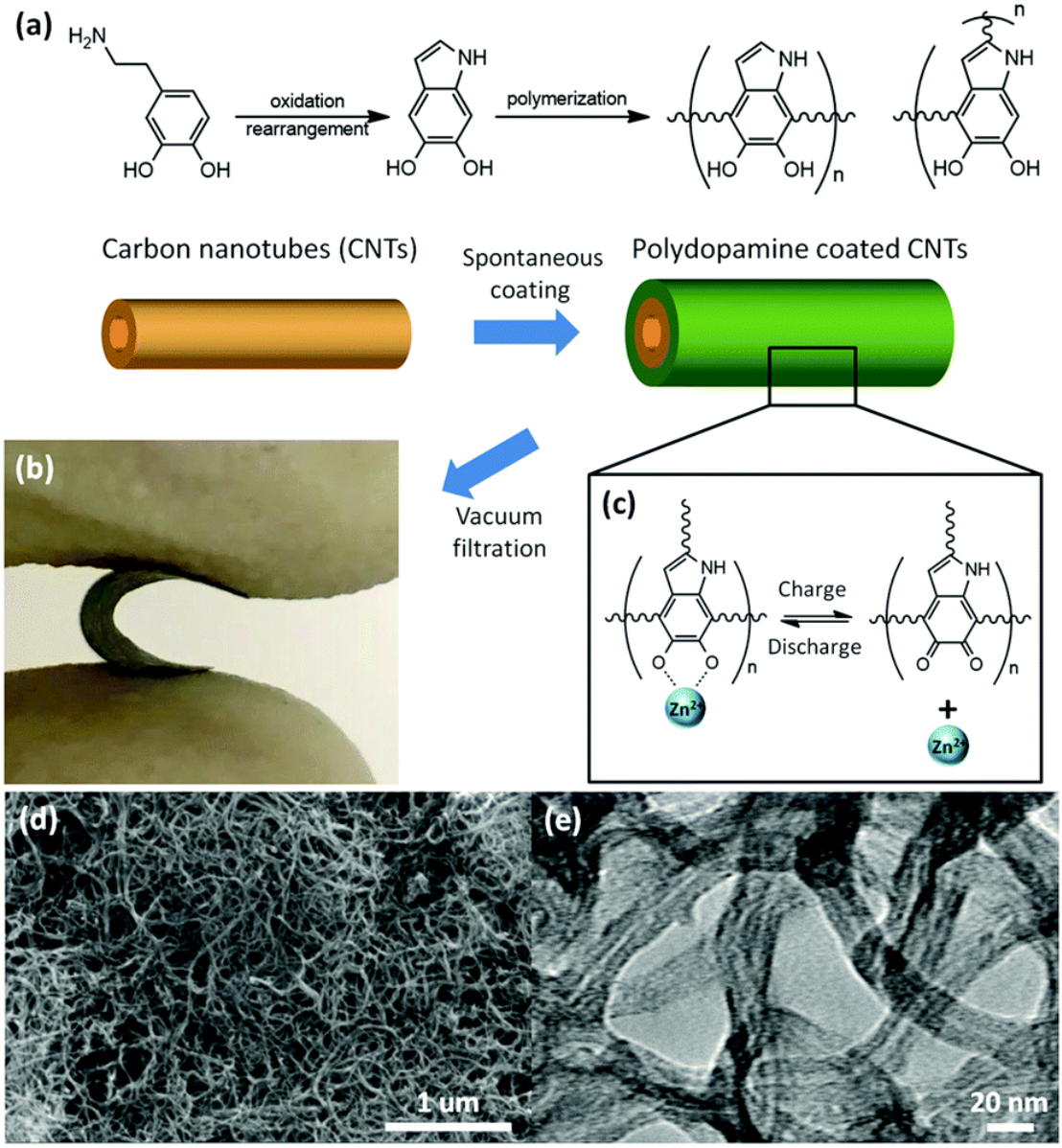

Figure 4-1 (a) Fabrication of PDA electrode by the spontaneous self-polymerization of dopamine on CNT supporting in basic aqueous solution. (b) Photo of a flexible free-standing CNT supported PDA thin film electrode. (c) Schematic of zinc ion adsorption by catechol and desorption by ortho-quinone when PDA at discharged or charged states, respectively. (d) Scanning electron microscopy (SEM). (e) Transmission electron microscopy (TEM) images of PDA electrode.

4.2 Fabrication of PDA electrode

We developed a flexible, free-standing, binder-free cathode for rechargeable aqueous zinc ion battery based on CNT supported PDA (Figure 4-1 (a and b)). PDA was coated on dispersed CNT by spontaneous polymerization of dopamine in a basic aqueous solution. Followed by vacuum-filtering the mixture dispersion, the free-standing thin film electrode was assembled while removing unreacted monomers. Outstanding flexibility of the thin film electrode is achieved due to the bio-adhesion nature of PDA. SEM images show the PDA coated CNTs in the electrode were well-dispersed but also well-connected (Figure 4-1 (d)). TEM images show that the PDA was uniformly coated onto CNT with a thickness of 8 nm (Figure 4-1 (e)). No aggregated PDA nanoparticles were found in either TEM or SEM images.

4.3 Electrochemical performances of PDA electrode

Cyclic voltammetry (CV) was first performed to assess the electrochemical behaviour of PDA as cathode material for zinc ion batteries (Figure 4-2 (a)). The PDA electrode was assembled into a coin cell with zinc foil as the anode, a filter paper as separator, and 3.3 M $ZnSO_4$ aqueous solution as the electrolyte. CV curves were obtained by scanning between 0.3 and 1.4 V vs. Zn^{2+}/Zn at a rate of 1 mV s^{-1}. The scanning begins with reduction (zinc ion adsorption) since the pristine PDA electrode contains no zinc ion. In both initial anodic and cathodic scans, strong but not well-defined features were

observed (Figure 4-6). After about 20 cycles, the peak current decreases and the curve gradually develops into a pair of wide and well-defined reduction/oxidation peaks at 0.91/1.15 V. Those two peaks correspond to the reversible reaction between catechol and ortho-quinone along with zinc ion adsorption/desorption. The CV curve shape change and capacity drop during initial cycles are likely related to the non-covalently bonded dopamine monomer and intermediate species assembled in the PDA structure, which will be discussed further later. The linear relationship between the peak current and scan rate indicated the redox reaction of PDA is controlled by a surface process (Figure 4-2 (b)), similar to the mechanism operating in pseudo-capacitors.

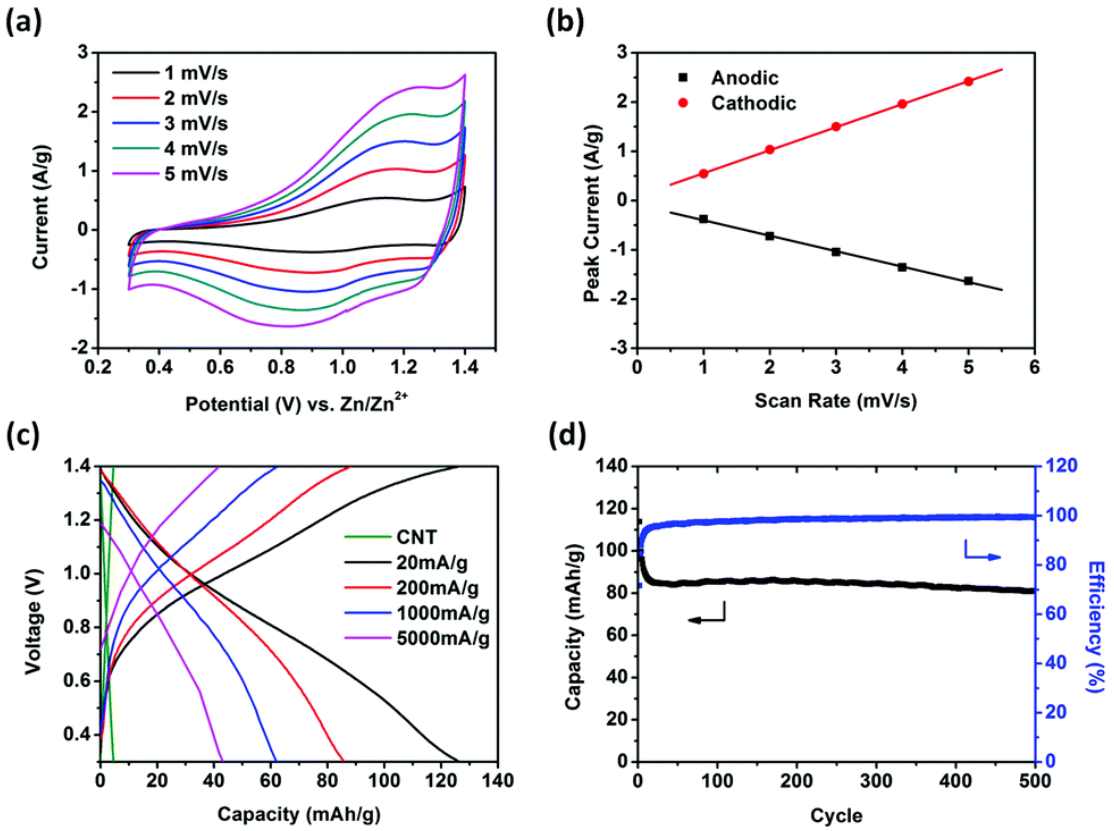

Figure 4-2 Electrochemical performances of PDA electrodes. (a) Cyclic voltammetry (CV) profiles at different scan rate. (b) CV peak current as a function of scan rate (c). Galvanostatic charge/discharge curves of PDA electrodes at different current densities and blank CNT thin film electrode at 200 mA g^{-1}. 20 mA g^{-1} curves was from 30th cycle. All other data were from 100th cycle. (d) Long term cyclic performance at 200 mA g^{-1} for 500 cycles. All tests were in coin cells at the potential range of 0.3-1.4 V, with zinc metal foil as anode and 3.3 M $ZnSO_4$ aqueous solution as electrolyte.

The cycling stability of PDA was evaluated by galvanostatic charge and discharge at a potential range of 0.3-1.4 V vs. Zn^{2+}/Zn. As shown in the Figure 4-2 (c), the PDA electrode delivered a capacity of 126.2 mA h g^{-1} at a low rate of 20 mA g^{-1}. The electrode is capable of exceptionally high rates, delivering 43.2 mA h g^{-1} at 5000 mA g^{-1}. Note that the majority of the loss is related to an IR drop which can be further improved by cell design. The high rate performance is consistent with the capacitive mechanism observed in CV studies. The capacity of CNT itself was also examined by fabricating free standing CNT thin film electrode with the same vacuum-filtration method. When discharged at 200 mA g^{-1}, the CNT thin film electrode can only deliver a capacity of 4.5 mA h g^{-1}, thus contributing very little to the CNT supported PDA electrode. The volumetric capacity of PDA electrode is moderate as shown in Figure 4-8. However, this does not preclude the application in biomedical devices and grid storage since unique advantages in flexibility, environmental friendliness, and cycle life are our main concern. The cycling performance of PDA was evaluated at a constant current density of 200 mA g^{-1} (Figure 4-2 (d)). After about 20 cycles, the battery reached a steady state and delivered a stable capacity of PDA for over 500 cycles. The 500th cycle maintained 96% capacity of the 20th cycle, which is attributed to the stable covalent cross-linked PDA structure and the highly reversible redox reaction of catechol/ortho-quinone groups. The high coulombic efficiency of about 99.4% also supports the outstanding reversibility of the redox reaction.

4.4 Energy storage mechanism of PDA electrode

The energy storage mechanism of PDA as a cathode material for zinc ion batteries was investigated by a comparison of *ex situ* Fourier-transform infrared (FT-IR) before and after electrochemical oxidation (Figure 4-3 (a)). The complex spectra in the 3300 to 3600 cm^{-1} region on the sample reduced at 0.3 V correspond to N-H, O-Zn-O and possible intermolecular bonds, which virtually disappeared when the electrode was charged (oxidized) to 1.4 V. In addition, a C=O bond signal at 1730 cm^{-1} appeared after charging, which supports the formation of a quinone structure. The double-peak at 2870, 2960 cm^{-1} and signals below 1600 cm^{-1} belong to the features of the indole structure, which exist all the time. The changes of FT-IR spectra clearly prove the reversible redox reaction between catechol and ortho-quinone of PDA.

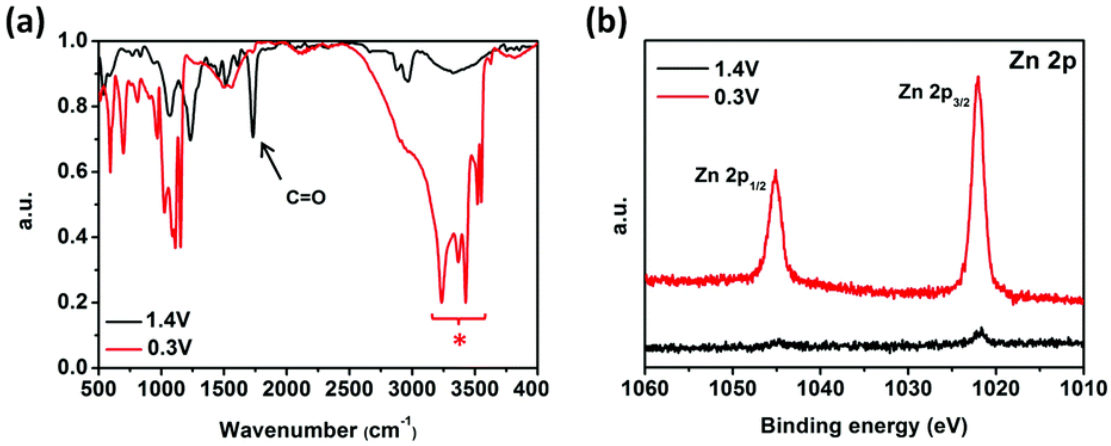

Figure 4-3 *Ex situ* spectroscopic analysis of PDA electrodes at charged (1.4 V) and discharged (0.3 V) states. (a) FT-IR. (b) High resolution XPS Zn 2p. All electrodes were cycled between 0.3-1.4 V in 3.3 M $ZnSO_4$ aqueous electrolyte for 20 cycles at 200 mA g^{-1}, then charged or discharged to noted potentials. Peaks noted with the asterisk symbol represent N-H, O-Zn-O structure, and possible intermolecular bonds.

Ex situ X-ray photoelectron spectroscopy (XPS) tests were performed to further analyze the energy storage mechanism of PDA. The wide-range XPS spectra for charged and discharged PDA electrodes exhibit almost identical signals for H, C, N and O (Figure 4-9). However, after repeated rinsing with water, only the spectra of discharged PDA electrode clearly shows a series of zinc features, including 2p, 3s, 3p, 3d and several auger LMM peaks, indicative of significant amounts of zinc ions binding to the catechols. The difference is more evident in the high resolution Zn 2p spectra (Figure 4-3 (b)). The charged PDA electrode exhibits negligible signal from Zn $2p_{1/2}$. The signal from Zn $2p_{3/2}$ is less than 5% of the peak area of discharged PDA, which might be due to residual $ZnSO_4$ electrolyte. It is well known that catechols have a strong binding affinity to multivalent cations and such interaction is significantly suppressed when oxidized to ortho-quinones.[35] Our observation is consistent with such a mechanism involving the reversible reaction between PDA and zinc ions.

We note that there is a capacity loss process during the first twenty cycles before stabilizing for hundreds of cycles. High resolution XPS was utilized to understand this phenomenon via examining the structure of PDA electrode. As-prepared pristine PDA electrode was first studied (Figure 4-10). The C 1s spectra can be deconvoluted into four peaks: CH_x, C-NH_2 and sp^2-hybridized carbon at 284.20 eV, C-O and C-N at 285.25 eV, C=O at 287.75 eV, and $\pi \rightarrow \pi^*$ for aromatic carbon species at 290.95 eV. The result matches with reported PDA materials.[36] The O 1s signals at 531.45 and 532.85 eV

correspond to C=O and C-O in the quinone/catechol structure, respectively, indicating the PDA electrode is a mixture of quinone and catechol in its as-synthesized form. The N 1s spectrum can be deconvoluted into one dominating peak at 399.70 eV corresponding to secondary amine (R_2NH), while the peaks at 401.45 eV and 398.45 eV can be assigned to primary amine (RNH_2) and tertiary or aromatic amine groups (=N-R), respectively. The presence of three different peaks indicated that the pristine PDA electrode contains not only PDA but also dopamine monomers and some intermediate species, consistent with the formation mechanism of PDA proposed by several recent studies (Figure 4-5).[37-40] The primary amine peak, 21% of the total N 1s signal, is indicative of unreacted dopamine monomers even after an extended polymerization reaction time. The tertiary amine intermediate specie contributes to about 7% of the total. The secondary amine peak, contributing 72% to the N 1s signal, is associated with both PDA and intermediate species. This is because the tertiary amine intermediate specie is a tautomer of secondary amine intermediate species. The presence of one type of intermediate specie indicates the co-existence of the other. We hypothesize that the non-negligible amount of non-covalently assembled dopamine and intermediate species in the pristine PDA electrodes are responsible for the initial capacity loss due to their dissolution in the electrolyte in ionized forms.

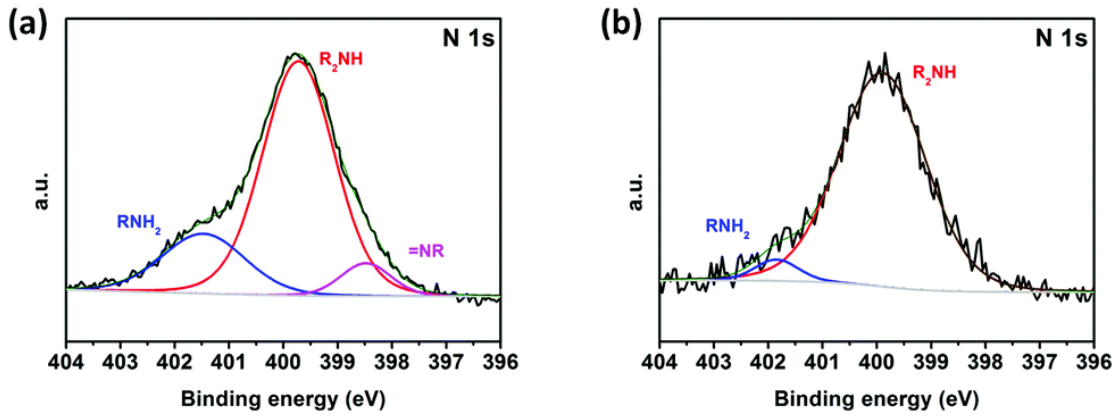

Figure 4-4 *Ex situ* high resolution XPS N 1s spectrums of PDA electrodes. (a) Before cycling. (b) After cycling.

To further confirm our hypothesis, *ex situ* XPS was performed. In the N 1s XPS spectrum of PDA electrode which has been cycled and reached steady-state capacity (Figure 4-4), the ratio of the primary amine peak, belonging to unreacted dopamine, decreases from 21% to 5% when compared with the pristine electrode. This indicates a loss of the primary amine during initial cycling. In the addition, no tertiary amine intermediate specie is observed in the cycled sample means the secondary amine peak is from only PDA. The total amount of non-covalent bonded species decreased from more than 28% to 5% during the process of PDA electrode reaching steady state.

The presence of dopamine monomer in the PDA electrode prior to cycling was also confirmed via UV-vis spectroscopy (Figure 4-11). Since CNT has strong signals in the UV range, PDA nanoparticles were prepared for these tests. Even after repeated washing, a strong peak at 280 nm, attributable to the dopamine monomer, can still be observed in PDA particles. The peak at 320 nm can be assigned to intermediate species.

Hence, during the initial cycles, non-covalently bonded species provided the extra capacity, which was gradually lost due to their solubility in the electrolyte. This hypothesis was further examined by a pre-cycling process. The pristine PDA electrode was pre-cycled for 50 cycles at 200 mA g^{-1} first. The electrode was then washed, dried, and re-assembled into a new battery. As shown in Figure 4-12, when cycled at 200 mA g^{-1}, the pre-cycled PDA electrode exhibited less significant initial capacity decay as compared with the pristine one. The stable capacity was increased from 86.0 mA h g^{-1} to 92.9 mA h g^{-1}, while many fewer cycles were needed for the capacity to stabilize. It is thus important to remove the encapsulated monomers as much as possible to obtain highly stable polymer cathodes.

4.5 Conclusion

In conclusion, we have demonstrated polydopamine (PDA) as a new organic cathode material for aqueous zinc ion battery. A flexible, free-standing, binder-free PDA cathode was fabricated with CNT as support. The PDA delivers a low-rate specific capacity of 126.2 mA h g^{-1}. After an initial stabilization period, outstanding long term stability was observed: after 500 cycles, the PDA electrode still retained 96% of the stabilized capacity. CV studies indicate the electrode reaction is a surface process, similar to that in electrochemical capacitors. FT-IR and XPS studies have established the reaction mechanism to be the redox reaction between catechol and ortho-quinone accompanied by

zinc ion adsorption and desorption. The non-toxic, flexible PDA has great potential to broaden the application of aqueous zinc ion battery, including in biomedical devices.

4.6 Experimental

Materials: 3-Hydroxytyramine hydrochloride (dopamine, 99%) was purchased from ACROS Organics. Tris(hydroxymethyl)aminomethane (Tris, 99.8%), hydrochloric acid (HCl, 36.5-38%) and zinc sulfate heptahydrate ($ZnSO_4 \cdot 6H_2O$, 99-103%) were purchased from Fisher Scientific. Carbon nanotube, multi-walled (MWCNT, >98% carbon basis) was purchased from Sigma-Aldrich. Zinc foil (0.25mm, 99.98% metals basis) was purchased from Alfar Aesar.

Sample preparation: 1 mg/ml dopamine was added into the tris-HCl aqueous solution (pH 8.5) dispersed with 0.5 mg/ml CNT. After stirring for 16 hours, the solution was vacuum filtered by a hydrophilic separator (Dreamweaver Silver 20). The free standing film can be peeled off from the separator when dried under vacuum at 70 ℃ overnight. The loading amount of polydopamine was 38.1% which was calculated by comparing with the pristine CNT film prepared with similar method. The loading density in the film was 0.9-1.3 mg/cm^2. Polydopamine particles were prepared with similar methods without adding CNT.

Sample characterization: The morphology of polydopamine electrode was characterized using transmission electron microscopy (TEM, FEI Tecnai G2 Sphera at

200 KV) and scanning electron microscopy (SEM, FEI Quanta 250) with atomic composition and elemental mapping analysis by an integrated energy-dispersive X-ray (EDX) spectrometer. The chemical structure of the membrane was characterized by Fourier transform infrared spectroscopy (FTIR, Perkin Elmer Spectrum Two) and X-ray photoelectron spectroscopy (XPS, Kratos Analytical, Kratos AXIS Supra). The UV-vis spectroscopy was conducted on Hitachi UH-4150. Reduced or oxidized state samples for FTIR and XPS were cycled at 200 mA g^{-1} for 20 cycles then discharged or charged to 0.3 V or 1.4 V respectively.

Electrochemical test: 2032-type coin cells were used for all the electrochemical tests. Zinc foil was used as the anode and filter paper (Whatman grade 2) was used as the separator. Argon purged 3.3 M $ZnSO_4$ aqueous solution (pH 4.5) was used as the electrolyte without pH adjustment. Cyclic voltammetry was performed on a potentiostat (Biologic VSP-300). Galvanostatic cycling was tested on a battery tester (Landt CT2001A). The pre-cycled sample was cycled for 50 cycles at 200 mA g^{-1} first. Then, after carefully washing and drying, the electrode was re-assembled into a new battery to test.

4.7 Appendix

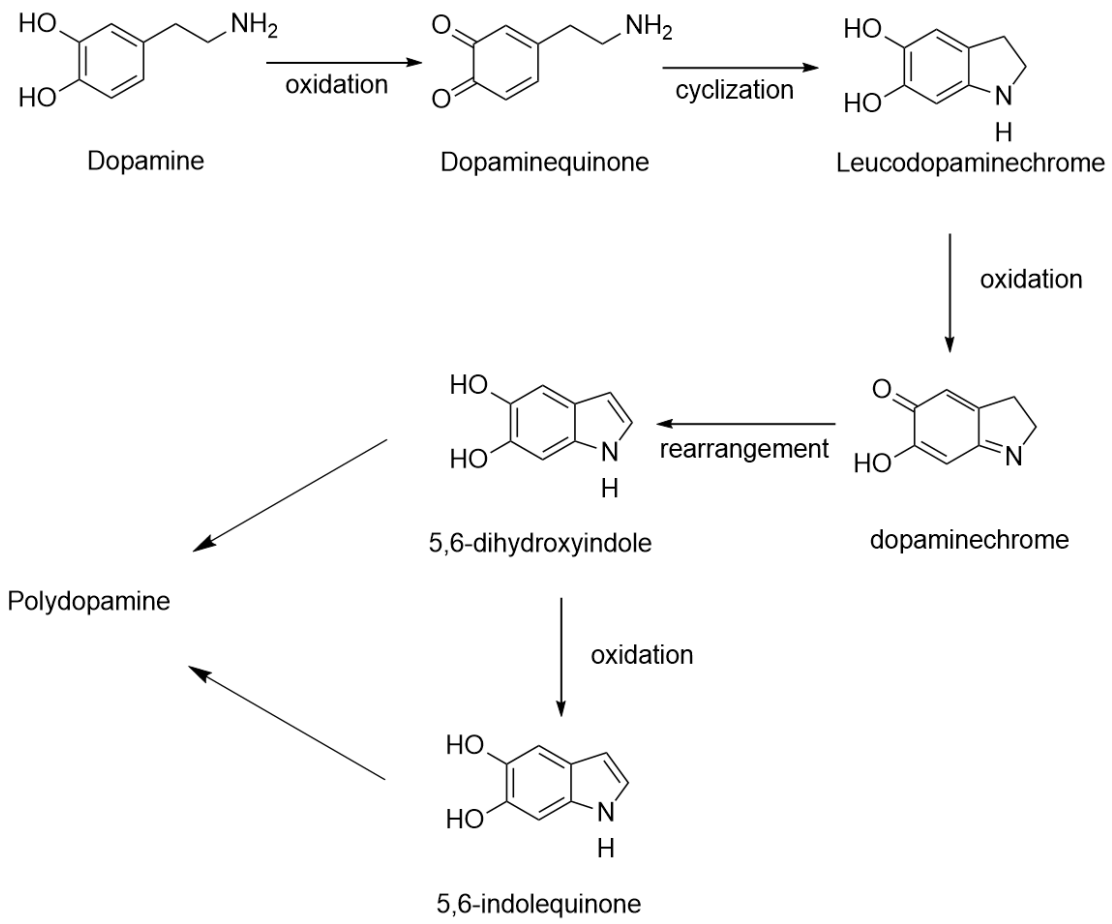

Figure 4-5 Possible reaction mechanism of PDA.

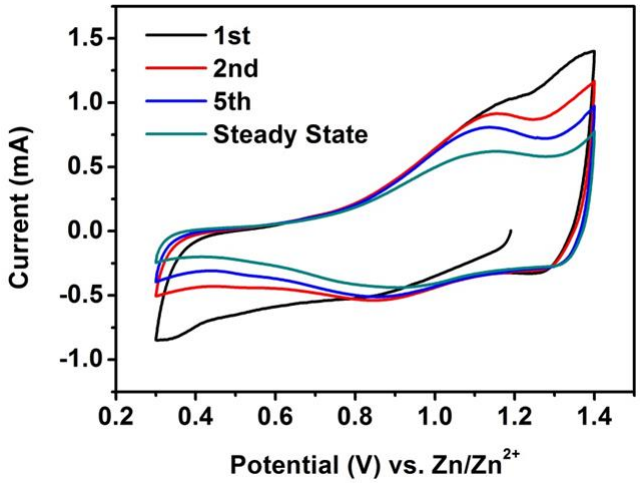

Figure 4-6 Cyclic voltammetry profiles of initial cycles and steady state scan at 1 mV s^{-1}.

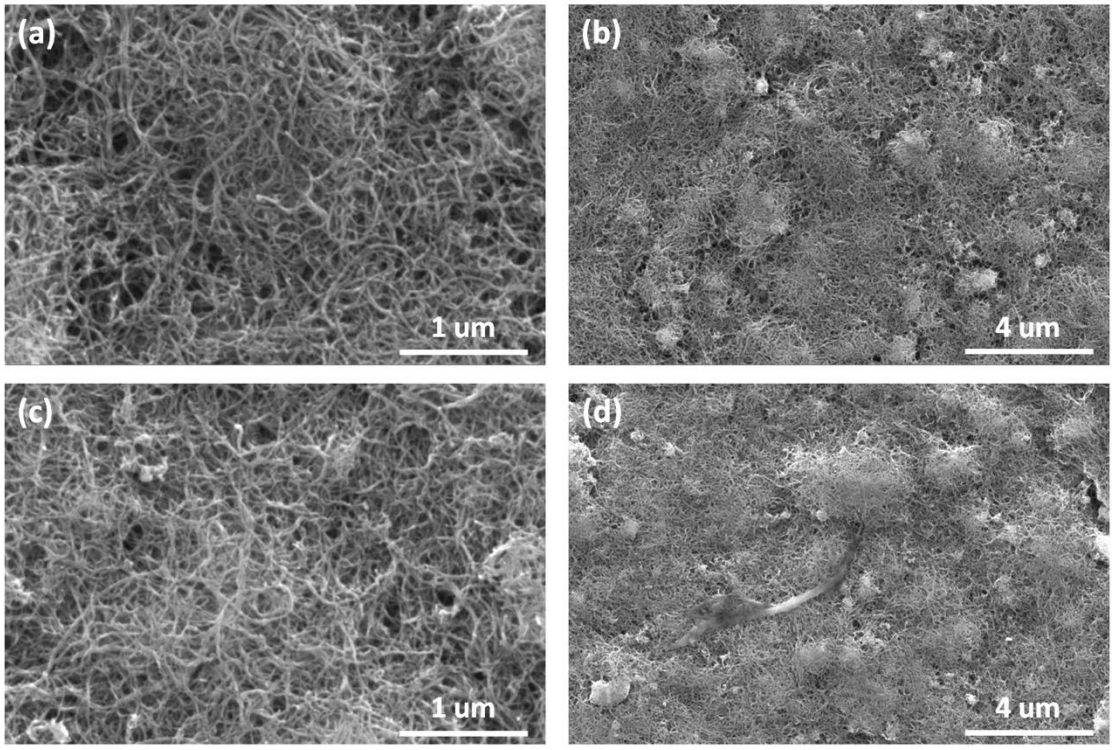

Figure 4-7 SEM images of PDA electrode. (a)(b) Before cycling. (c)(d) After 400 cycles at 200 mA g^{-1}

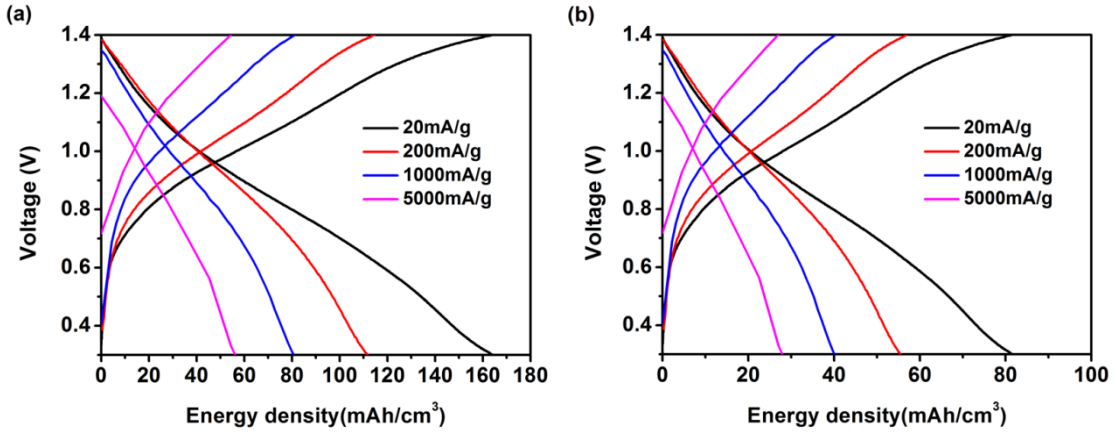

Figure 4-8 Volumetric specific capacity at different current densities: (a) polydopamine (b) polydopamine electrode. Converted from Figure 4-2(c).

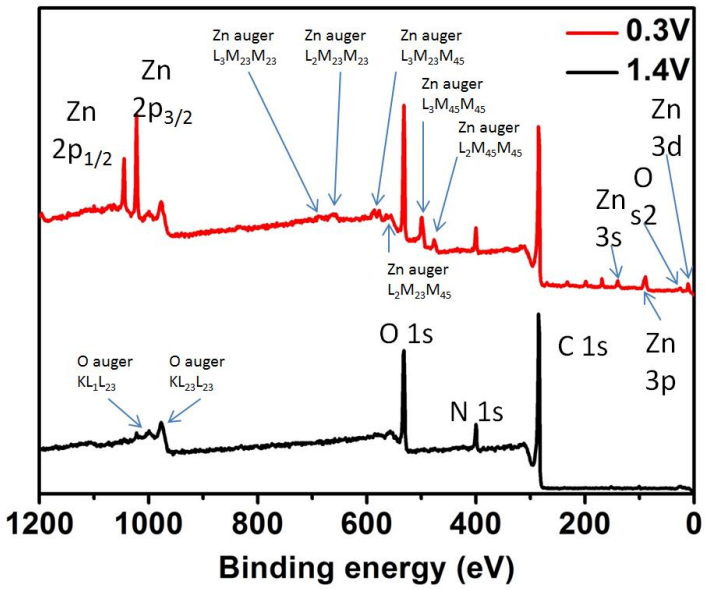

Figure 4-9 *Ex situ* low resolution XPS analysis of PDA electrodes at charged (1.4 V) and discharged (0.3 V) states.

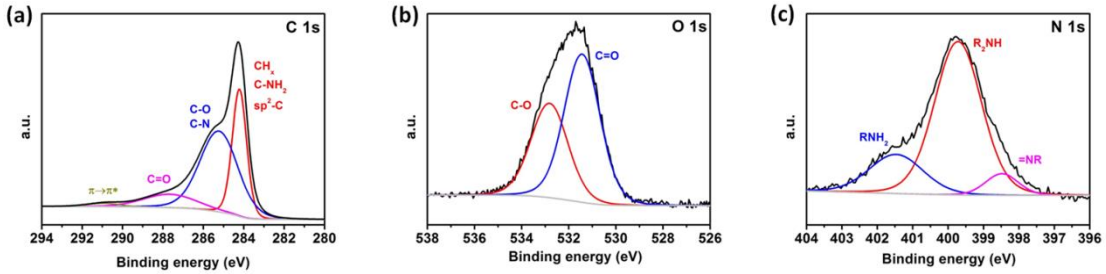

Figure 4-10 High resolution X-ray photoelectron spectroscopy (XPS) spectra of pristine PDA electrode. (a) C 1s, (b) O 1s, (c) N 1s.

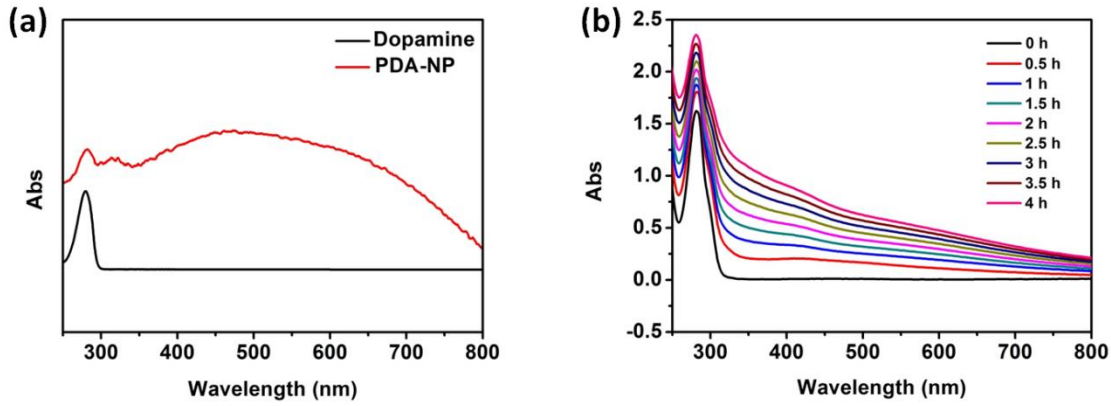

Figure 4-11 UV-vis analysis (a) Dopamine monomer and washed PDA nanoparticles in water. (b) *in situ* characterization of the polymerization of dopamine.

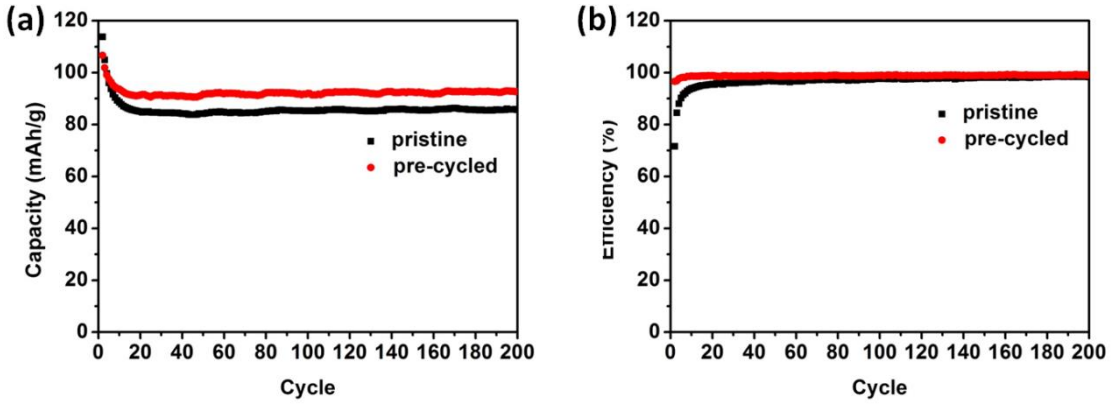

Figure 4-12 Cyclic performance of pristine and pre-cycled PDA electrode.

4.8 Acknowledgments

Text, tables, and figures in this chapter, in full, are reprints of materials published in the following paper: Xiujun Yue, Haodong Liu and Ping Liu*, “Polymer grafted on carbon nanotubes as a flexible cathode for aqueous zinc ion batteries" *Chem. Commun.* **2019**, 55, 1647-1650. The dissertation author was the primary researcher for

the data presented and was the primary author of this publication. The permissions to reproduce this material were granted by the Royal Society of Chemistry, copyright 2019.

4.9 References

1. Song, M.; Tan, H.; Chao, D.; Fan, H. J. Recent Advances in Zn-Ion Batteries. *Adv. Funct. Mater.,* **2018,** *28*, 1802564.

2. Zhang, X., *Corrosion and Electrochemistry of Zinc*. Springer US: New York, 1996.

3. Xu, C.; Li, B.; Du, H.; Kang, F. Energetic Zinc Ion Chemistry: The Rechargeable Zinc Ion Battery. *Angew. Chem. Int. Ed.,* **2012,** *51*, 933-935.

4. Muldoon, J.; Bucur, C. B.; Gregory, T. Quest for Nonaqueous Multivalent Secondary Batteries: Magnesium and Beyond. *Chem. Rev.,* **2014,** *114*, 11683-11720.

5. Zhang, L.; Chen, L.; Zhou, X.; Liu, Z. Towards High-Voltage Aqueous Metal-Ion Batteries Beyond 1.5 V: The Zinc/Zinc Hexacyanoferrate System. *Adv. Energy Mater.,* **2015,** *5*, 1400930.

6. Konarov, A.; Voronina, N.; Jo, J. H.; Bakenov, Z.; Sun, Y.-K.; Myung, S.-T. Present and Future Perspective on Electrode Materials for Rechargeable Zinc-Ion Batteries. *ACS Energy Lett.,* **2018,** *3*, 2620-2640.

7. Kundu, D.; Adams, B. D.; Duffort, V.; Vajargah, S. H.; Nazar, L. F. A high-capacity and long-life aqueous rechargeable zinc battery using a metal oxide intercalation cathode. *Nat. Energy,* **2016,** *1*, 16119.

8. Wang, F.; Borodin, O.; Gao, T.; Fan, X.; Sun, W.; Han, F.; Faraone, A.; Dura, J. A.; Xu, K.; Wang, C. Highly reversible zinc metal anode for aqueous batteries. *Nature Materials*, **2018,** *17*, 543-549.

9. Wu, X.; Xiang, Y.; Peng, Q.; Wu, X.; Li, Y.; Tang, F.; Song, R.; Liu, Z.; He, Z.; Wu, X. Green-low-cost rechargeable aqueous zinc-ion batteries using hollow porous spinel $ZnMn_2O_4$ as the cathode material. *J. Mater. Chem. A,* **2017,** *5*, 17990-17997.

10. Zhang, N.; Cheng, F.; Liu, Y.; Zhao, Q.; Lei, K.; Chen, C.; Liu, X.; Chen, J. Cation-Deficient Spinel $ZnMn_2O_4$ Cathode in $Zn(CF_3SO_3)_2$ Electrolyte for Rechargeable Aqueous Zn-Ion Battery. *J. Am. Chem. Soc.,* **2016,** *138*, 12894-12901.

11. He, P.; Quan, Y.; Xu, X.; Yan, M.; Yang, W.; An, Q.; He, L.; Mai, L.

High-Performance Aqueous Zinc–Ion Battery Based on Layered $H_2V_3O_8$ Nanowire Cathode. *Small,* **2017,** *13,* 1702551.

12. Sambandam, B.; Soundharrajan, V.; Kim, S.; Alfaruqi, M. H.; Jo, J.; Kim, S.; Mathew, V.; Sun, Y.-k.; Kim, J. Aqueous rechargeable Zn-ion batteries: an imperishable and high-energy $Zn_2V_2O_7$ nanowire cathode through intercalation regulation. *J. Mater. Chem. A,* **2018,** *6,* 3850-3856.

13. Alfaruqi, M. H.; Mathew, V.; Gim, J.; Kim, S.; Song, J.; Baboo, J. P.; Choi, S. H.; Kim, J. Electrochemically Induced Structural Transformation in a γ-MnO_2 Cathode of a High Capacity Zinc-Ion Battery System. *Chem. Mater.,* **2015,** *27,* 3609-3620.

14. Chae, E.; Gim, J.; Song, J.; Kim, S.; Mathew, V.; Han, J.; Boo, S.; Kim, J. Mesoporous manganese dioxide cathode prepared by an ambient temperature synthesis for Na-ion batteries. *RSC Adv.,* **2013,** *3,* 26328-26333.

15. Ming, J.; Guo, J.; Xia, C.; Wang, W.; Alshareef, H. N. Zinc-ion batteries: Materials, mechanisms, and applications. *Mater. Sci. Eng. R,* **2019,** *135,* 58-84.

16. Lee, B.; Seo, H. R.; Lee, H. R.; Yoon, C. S.; Kim, J. H.; Chung, K. Y.; Cho, B. W.; Oh, S. H. Critical Role of pH Evolution of Electrolyte in the Reaction Mechanism for Rechargeable Zinc Batteries. *ChemSusChem,* **2016,** *9,* 2948-2956.

17. Zhang, N.; Cheng, F.; Liu, J.; Wang, L.; Long, X.; Liu, X.; Li, F.; Chen, J. Rechargeable aqueous zinc-manganese dioxide batteries with high energy and power densities. *Nat. Commun.,* **2017,** *8,* 405.

18. Pan, H.; Shao, Y.; Yan, P.; Cheng, Y.; Han, K. S.; Nie, Z.; Wang, C.; Yang, J.; Li, X.; Bhattacharya, P.; Mueller, K. T.; Liu, J. Reversible aqueous zinc/manganese oxide energy storage from conversion reactions. *Nat. Energy,* **2016,** *1,* 16039.

19. Jia, Z.; Wang, B.; Wang, Y. Copper hexacyanoferrate with a well-defined open framework as a positive electrode for aqueous zinc ion batteries. *Mater. Chem. Phys.,* **2015,** *149-150,* 601-606.

20. Liu, Z.; Bertram, P.; Endres, F. Bio-degradable zinc-ion battery based on a prussian blue analogue cathode and a bio-ionic liquid-based electrolyte. *J. Solid State Electrochem.,* **2017,** *21,* 2021-2027.

21. Liu, T.; Kim, K. C.; Lee, B.; Chen, Z.; Noda, S.; Jang, S. S.; Lee, S. W. Self-polymerized dopamine as an organic cathode for Li- and Na-ion batteries. *Energy Environ. Sci.,* **2017,** *10,* 205-215.

22. Liang, Y.; Jing, Y.; Gheytani, S.; Lee, K.-Y.; Liu, P.; Facchetti, A.; Yao, Y. Universal quinone electrodes for long cycle life aqueous rechargeable batteries. *Nature Materials,*

2017, *16*, 841.

23. Milczarek, G.; Inganäs, O. Renewable Cathode Materials from Biopolymer/Conjugated Polymer Interpenetrating Networks. *Science,* **2012,** *335*, 1468-1471.

24. Liang, Y.; Tao, Z.; Chen, J. Organic Electrode Materials for Rechargeable Lithium Batteries. *Adv. Energy Mater.,* **2012,** *2*, 742-769.

25. Pan, B.; Zhou, D.; Huang, J.; Zhang, L.; Burrell, A. K.; Vaughey, J. T.; Zhang, Z.; Liao, C. 2,5-Dimethoxy-1,4-Benzoquinone (DMBQ) as Organic Cathode for Rechargeable Magnesium-Ion Batteries. *J. Electrochem. Soc.,* **2016,** *163*, A580-A583.

26. Zhao, Q.; Huang, W.; Luo, Z.; Liu, L.; Lu, Y.; Li, Y.; Li, L.; Hu, J.; Ma, H.; Chen, J. High-capacity aqueous zinc batteries using sustainable quinone electrodes. *Science Advances*, **2018,** *4*, eaao1761.

27. Dawut, G.; Lu, Y.; Miao, L.; Chen, J. High-performance rechargeable aqueous Zn-ion batteries with a poly(benzoquinonyl sulfide) cathode. *Inorganic Chemistry Frontiers*, **2018,** *5*, 1391-1396.

28. Lee, H.; Dellatore, S. M.; Miller, W. M.; Messersmith, P. B. Mussel-Inspired Surface Chemistry for Multifunctional Coatings. *Science,* **2007,** *318*, 426-430.

29. Xiao, M.; Li, Y.; Allen, M. C.; Deheyn, D. D.; Yue, X.; Zhao, J.; Gianneschi, N. C.; Shawkey, M. D.; Dhinojwala, A. Bio-Inspired Structural Colors Produced via Self-Assembly of Synthetic Melanin Nanoparticles. *ACS Nano,* **2015,** *9*, 5454-5460.

30. d'Ischia, M.; Napolitano, A.; Pezzella, A.; Meredith, P.; Sarna, T. Chemical and Structural Diversity in Eumelanins: Unexplored Bio-Optoelectronic Materials. *Angew. Chem. Int. Ed.,* **2009,** *48*, 3914-3921.

31. Szpoganicz, B.; Gidanian, S.; Kong, P.; Farmer, P. Metal binding by melanins: studies of colloidal dihydroxyindole-melanin, and its complexation by Cu(II) and Zn(II) ions. *J. Inorg. Biochem.*, **2002,** *89*, 45-53.

32. Kim, Y. J.; Wu, W.; Chun, S.-E.; Whitacre, J. F.; Bettinger, C. J. Catechol-Mediated Reversible Binding of Multivalent Cations in Eumelanin Half-Cells. *Adv. Mater.,* **2014,** *26*, 6572-6579.

33. Yoon, T. H.; Park, Y. J. New strategy toward enhanced air electrode for Li–air batteries: apply a polydopamine coating and dissolved catalyst. *RSC Adv.,* **2014,** *4*, 17434-17442.

34. Huang, Y.; Li, Y.; Hu, Z.; Yue, X.; Proetto, M. T.; Jones, Y.; Gianneschi, N. C.

Mimicking Melanosomes: Polydopamine Nanoparticles as Artificial Microparasols. *ACS Central Science,* **2017,** *3*, 564-569.

35. Lee, H.; Scherer, N. F.; Messersmith, P. B. Single-molecule mechanics of mussel adhesion. *PNAS,* **2006,** *103*, 12999-13003.

36. Zangmeister, R. A.; Morris, T. A.; Tarlov, M. J. Characterization of Polydopamine Thin Films Deposited at Short Times by Autoxidation of Dopamine. *Langmuir,* **2013,** *29*, 8619-8628.

37. Li, Y.; Liu, M.; Xiang, C.; Xie, Q.; Yao, S. Electrochemical quartz crystal microbalance study on growth and property of the polymer deposit at gold electrodes during oxidation of dopamine in aqueous solutions. *Thin Solid Films,* **2006,** *497*, 270-278.

38. Bernsmann, F.; Ball, V.; Addiego, F.; Ponche, A.; Michel, M.; Gracio, J. J. d. A.; Toniazzo, V.; Ruch, D. Dopamine−Melanin Film Deposition Depends on the Used Oxidant and Buffer Solution. *Langmuir,* **2011,** *27*, 2819-2825.

39. Arzillo, M.; Mangiapia, G.; Pezzella, A.; Heenan, R. K.; Radulescu, A.; Paduano, L.; d'Ischia, M. Eumelanin Buildup on the Nanoscale: Aggregate Growth/Assembly and Visible Absorption Development in Biomimetic 5,6-Dihydroxyindole Polymerization. *Biomacromolecules,* **2012,** *13*, 2379-2390.

40. Jiang, J.; Zhu, L.; Zhu, L.; Zhu, B.; Xu, Y. Surface Characteristics of a Self-Polymerized Dopamine Coating Deposited on Hydrophobic Polymer Films. *Langmuir,* **2011,** *27*, 14180-14187.